A Microscopic Continuum Model of a Proton Exchange Membrane Fuel Cell Electrode Catalyst Layer

Kenneth Weber Armstrong

Thesis Submitted to the Faculty of
Virginia Polytechnic Institute and State University
in partial fulfillment of the requirements for the degree of

Master of Science

in

Mechanical Engineering

Committee Members:

Dr. Michael R. von Spakovsky, Chair
Dr. Michael W. Ellis
Dr. Douglas J. Nelson

Friday, September 10, 2004
Blacksburg, Virginia

Keywords: Fuel Cell, PEMFC, CFD, Modeling, Agglomerate, Catalyst

A Microscopic Continuum Model of a Proton Exchange Membrane Fuel Cell Electrode Catalyst Layer

Kenneth W. Armstrong

Abstract

A series of steady-state microscopic continuum models of the cathode catalyst layer (active layer) of a proton exchange membrane fuel cell are developed and presented. This model incorporates O_2 species and ion transport while taking a discrete look at the platinum particles within the active layer. The original 2-dimensional axisymmetric Thin Film and Agglomerate Models of Bultel, Ozil, and Durand [8] were initially implemented, validated, and used to generate various results related to the performance of the active layer with changes in the thermodynamic conditions and geometry. The Agglomerate Model was then further developed, implemented, and validated to include among other things pores, flooding, and both humidified air and humidified O_2. All models were implemented and solved using FEMAP™ and a computational fluid dynamics (CFD) solver, developed by Blue Ridge Numerics Inc. (BRNI) called CFDesign™.

The use of these models for the discrete modeling of platinum particles is shown to be beneficial for understanding the behavior of a fuel cell. The addition of gas pores is shown to promote high current densities due to increased species transport throughout the agglomerate. Flooding is considered, and its effect on the cathode active layer is evaluated. The model takes various transport and electrochemical kinetic parameters values from the literature in order to do a parametric study showing the degree to which temperature, pressure, and geometry are crucial to overall performance. This parametric study quantifies among a number of other things the degree to which lower porosities for thick active layers and higher porosities for thin active layers are advantageous to fuel cell performance. Cathode active layer performance is shown not to be solely a function of catalyst surface area but discrete catalyst placement within the agglomerate.

Acknowledgements

I would like to thank my thesis committee, Dr. Ellis and Dr. Nelson, for taking their time to review my Masters Thesis. Dr. von Spakovsky, my chair advisor, for presenting me with a great opportunity to work on exactly what I wanted and for all of the advice and guidance over my entire graduate career. Last but not least, I would also like to thank Dr. Siegel whose counsel throughout the past two years has helped guide this work into what it is today.

Dedication

This thesis is dedicated to my family and friends near and far and to Ashley in particular for her words of encouragement and inspiration over the past five years.

Table of Contents

List of Figures

List of Tables

Nomenclature

Parameter and variables

A_{Pt}	surface area of Pt, μm^2
a	interparticle distance, μm
b	Tafel slope, V/decade
C	concentration, mol/ μm^3
d	mean particle diameter, μm
D	diffusion coefficient μm^2/sec
D_{eff}	effective diffusion coefficient
F	Farraday's constant, 96485 col/mol e^-
H	Henry's constant
i	current density, A/ μm^2
i_o	current density, A/ μm^2
k_P	permeability, mol/ms
L	maximum length for any X or Y direction, μm
n	flux of O_2 consumed, mole/ μm^2
r_o	outer radius of platinum particle, μm
r_i	inner radius of platinum particle, μm
T	temperature, °K
S	source term
V_{Pt}	volume of Pt, μm^3

Greek

$r_{A/V}$	area/unit volume, 1/ μm
η	local overpotential, V
κ	conductivity, S/ μm

Subscripts

O_2	oxygen
H^+	hydrogen ion

Superscripts

Air	air
G	gas pore
max	maximum value terms
P	polymer
W	water
*	effective terms

Chapter 1: Introduction

Recently, hydrogen as an energy carrier and fuel has garnered much interest around the world. Impressions of the use of hydrogen have evolved from negative connotations associated with the Hindenburg to the current possibilities of using it to fuel America in to the future. Hydrogen technology in the past few years has made its way into gasoline and auto manufactures' commercials as well as the state of the union address. To many it is not a question of if hydrogen is a viable alternative to fossil fuels, but instead when will implementations of a hydrogen infrastructure become common place around the world.

One of the reasons hydrogen has become such an important topic can be attributed to major advances in fuel cell technology over the past several decades. Fuel cells originally were used by NASA for missions in space. This has evolved into fuel cells being considered for all types of applications in order to meet the world's ever-growing appetite for energy. Currently, prototype and some commercial fuel cells are being used to power homes, automobiles, and even smaller electronics such as computers and cell phones. The recent adoption of this technology in certain niche markets is due to fuel cells becoming more economically viable. This technology has been around for more then a hundred years but has gained much promise as of late due to its potential competitiveness with more conventional energy conversion technologies. This chapter will provide a brief description of fuel cell technology in general and proton exchange membrane fuel cells (PEMFC) in particular.

1.1 Fuel Cells

1.1.1 Overview of Fuel Cells

A fuel cell operates by utilizing a relatively simple conversion process involving

species of hydrogen and oxygen, combining them to make water and energy. During the conversion which is electrochemical in nature a fuel cell produces energy in the form of electricity, a very valuable form of energy. From electrical energy one can power just about anything. Conversely, electrical energy can be used to split hydrogen and oxygen from water. This process is called electrolysis. Because a fuel cell can directly transform chemical energy into electrical energy, it is very different than conventional energy conversion devices (engines) based on combustion. Such engines are limited by the Carnot heat engine efficiency. This means that a combustion engine's efficiency is limited by the temperature difference of the two reservoirs between which it operates. Fuel cells on the other hand, which are based on the use of electrochemical instead of chemical reactions, are not restrained by Carnot's maximum efficiency. Thus, in theory, their efficiencies can significantly surpass those of combustion engines.

Fuel cells are also pollution free when using hydrogen directly as a fuel, since the products are simply water and energy. This is very attractive to the world's overall ecosystem. The burning of fossil fuels releases tons of greenhouse gases into the world's atmosphere everyday. Many, though not all experts, believe that this is leading to an elevation in the earth's average surface temperature with potential destructive effects to the entire ecosystem. Thus, fuel cells are being looked at as viable alternatives to conventional energy conversion technologies from an environmental stand point.

Figure 1.1: Fuel cell stack made from many individual cells [1].

Fuel cells also happen to be very scalable which means that cost and performance scales well with size (e.g. large and small stacks are equally efficient). Also, more power simply requires adding more cells which is beneficial from a mass production standpoint since the same cells can be manufactured and different amounts combined for different applications. Figure 1.1 shows a stack, which is many individual fuel cells combined in

series to produce power. A stack can vary from a few cells for electronic applications, to many cells used to power homes or automobiles.

Figure 1.2: Ford P2000 [2].

Fuel cells are also conducive to automotive power requirements. A typical combustion engine is most efficient at high load where a car spends very little of its time. A fuel cell vehicle like the one shown in Figure 1.2 is much more efficient across a large range of loads which is beneficial to an automobile because most of its time is spent at light loads.

1.1.2 Different Types of Fuel Cells

There are various types of fuel cells generally classified by the type of electrolyte they use (with the exception of the DMFC which is named after the fuel used). Though the overall reaction in which hydrogen and oxygen combine forming energy and water remains the same, the way the reaction is carried out varies. Table 1.1 list the various major types of fuel cells and their major operating parameters.

Important information to note in Table 1.1 is the applications and efficiencies for each type of technology. One technology that particularly stands out is the Proton Exchange Membrane Fuel Cell (PEMFC). PEMFCs are capable of producing high efficiencies at low temperatures. This is very beneficial to automobiles, which require a fast start-up time. Being able to operate at lower temperatures means the fuel cell can power up in seconds rather then minutes or hours. PEMFCs also have high energy densities, which are critical for automotive applications.

Table 1.1: Various Types of Fuel Cells [3].

Fuel Cell Type	Electrolyte	Anode Gas	Cathode Gas	Temperature	Application	Efficiency
Proton Exchange Membrane (PEM)	solid polymer membrane	hydrogen	pure or atmospheric oxygen	75°C (180°F)	smaller electronics automotive residential	35–60%
Alkaline (AFC)	potassium hydroxide	hydrogen	pure oxygen	below 80°C	Space Shuttle, specialized application	50–70%
Direct Methanol (DMFC)	solid polymer membrane	methanol solution in water	atmospheric oxygen	75°C (180°F)	portable electronics	35–40%
Phosphoric Acid (PAFC)	phosphoric acid	hydrogen	atmospheric oxygen	210°C (400°F)	industrial, commercial	35–50%
Molten Carbonate (MCFC)	alkali-carbonates	hydrogen, methane	atmospheric oxygen	650°C (1200°F)	industrial, commercial	40–55%
Solid Oxide (SOFC)	ceramic oxide	hydrogen, methane	atmospheric oxygen	800–1000°C (1500–1800°F)	industrial, commercial, residential	45–60%

Alkaline Fuel Cells (AFCs) due to their reliance on very pure fuels will probably rarely see applications beyond the space shuttle any time in the near future. Direct Methanol Fuel Cell (DMFC) technology is rather new to the spectrum and is based on PEMFC technology except for the use of a dilute mixture of methanol in water instead of hydrogen. This is beneficial due to the present abundance of methanol in the energy sector. In contrast, a hydrogen infrastructure will take time to develop.

Phosphoric Acid Fuel Cells (PAFCs) are probably the most mature of all the fuel cell technologies and are currently serving the power requirements of commercial building, buses, and hospitals. Molten Carbonate Fuel Cells (MCFCs), on the other hand, are new on the scene but are expected to start making an impact very soon. However, since they operate at a high temperature and have a low power density, their use will be limited to large terrestrial applications.

Finally, Solid Oxide Fuel Cells (SOFCs) will be coming online throughout America within the next 3 to 5 years. SOFCs operate at high temperatures and have decent energy densities and relatively high efficiencies. When combined in a

cogeneration scheme requiring process steam or as a topping cycle to a gas turbine, steam turbine, or combined cycle, their efficiencies can be extremely high.

1.2 Proton Exchange Membrane Fuel Cells (PEMFCs)

A proton exchange membrane fuel cell (PEMFC) is simply electrolysis in reverse. By combining oxygen and hydrogen, it is able to produce energy. The overall chemical reaction for a PEMFC is

$$H_2 + \frac{1}{2}O_2 \Leftrightarrow H_2O. \tag{1.1}$$

This overall conversion results from two separate electrochemical reactions taking place in parallel. These are shown in Figures 1.3 and are generally confined to two separate

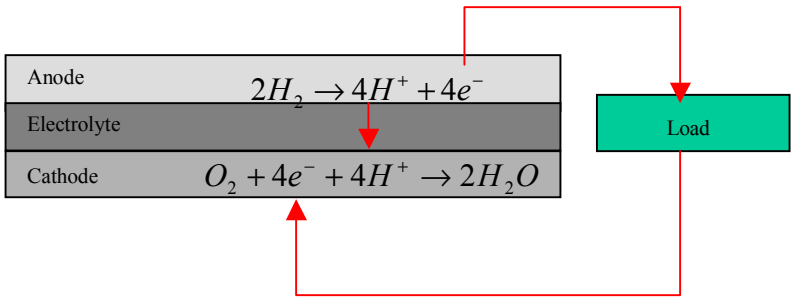

Figure 1.3: Governing electrochemical reactions for a proton exchange membrane fuel cell.

acid electrolyte active layers. At the anode active layer (anode catalyst layer), hydrogen ionizes, creating electrons and protons. The protons are conducted through the permeable membrane to the cathode active layer, and the electrons are conducted to an exterior circuit or neighboring cell. At the cathode active layer (cathode catalyst layer), oxygen reacts with protons from the anode as well as electrons from an external circuit or neighboring cell in order to create water and release thermal energy. This total process creates a potential between the anode and the cathode. Thus, when connecting a load to

the external circuit, power is produced from the reaction. A depiction of the processes occurring in a PEMFC is given in Figure 1.4.

PEMFCs are applicable to a broad range of applications. In particular, PEMFCs show great promise of being adopted into vehicles. For this reason, a great deal of research has been conducted to prefect this power source. PEMFCs are able to operate at low temperatures, which is very important for automotive applications since operating at low temperatures means short start-up times and increased operational safety.

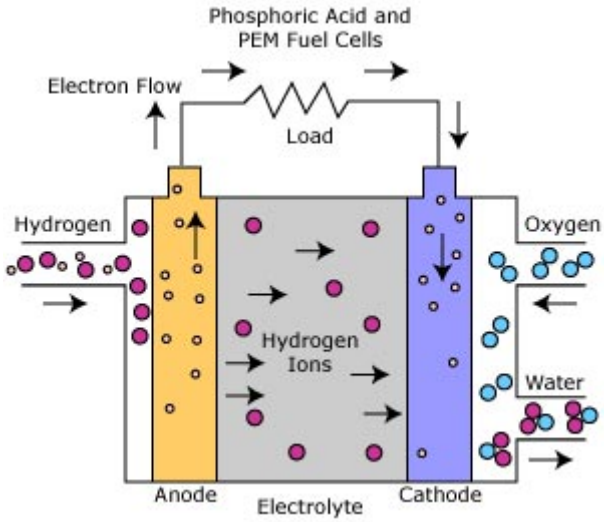

Figure 1.4: Diagram of a Fuel cell in operation [4].

Because of the low temperatures, PEMFCs have a relatively slow reaction rate. This problem is addressed with the addition of catalysts to the reaction. A catalyst is a substance that aides in reaction rate without being consumed in the reaction. Platinum is the most common catalyst used to increase the reaction rate for a PEMFC. However, since platinum is a precious metal it is fairly expensive and careful steps must be taken to reduce the amount used within a fuel cell.

The importance of the catalyst particles for the performance of a fuel cell have prompted the development of a number of models and experiments have in order to find out the correct size and distribution of these particles along with the electronic and protonic conducting materials as well as pores which comprise the anode or cathode catalyst layers. A good deal of this research has focused on the reaction rate being a function of loading, and loading alone. In addition, there have been some experiments

conducted to find the optimal platinum size and spacing. However, there has been little research into the overall distribution of the platinum particles in the active layer. This distribution which is important for controlling fuel cell performance spawned the current research, presented in this thesis.

Reducing catalyst loading is beneficial to the over all price of a fuel cell, but with current loadings becoming so low, the main goal is to improve performance. By mapping the platinum particles themselves, one can pinpoint the best geometric arrangement to improve performance possibly and reduce loading even further.

1.3 Fuel Cell Modeling

Fuel cells have been mathematically modeled extensively throughout the past decade. By using governing equations that model the different layers present within the fuel cell, the cost and time associated with prototype development can be reduced. With a finite element, difference, or volume approach, these governing equations, closure relations and boundary conditions can be applied to the given geometry and solved for a discrete set of elements, nodes, or volumes. The more elements, nodes, or volumes used the greater the accuracy of the solution as well as the greater the solution time. Therefore, a compromise must be made between finding a valid solution and the solution time required to find it.

Mathematical models also allow one to predict the behavior of certain parameters which would be nearly impossible to do experimentally. For example, one of the major parameters investigated in this research was the concentration of oxygen at different points in the active layer, something that would be difficult to do in a working fuel cell without disturbing its natural process.

Throughout most of the literature surveyed with regards to PEMFC modeling, a homogeneous model is assumed in order to model the behavior of the electrode catalyst layer. This type of model assumes that the catalyst is homogeneously mixed within the layer so that the layer can be treated as a whole. Under this assumption, catalyst loading along with volumetric macroscopic parameters such as porosity, tortnosity, and saturation

(e.g. [5], [6], and [7]) are the sole parameters directly related to the geometry which can be varied within the model. These parameters cannot account in detail for variances in platinum size, interparticle distance, or a particular particle's placement within a given geometry. However, all of these additional considerations can be taken into account when using a microscopic continuum model[1]. Such a model accounts for the actual make-up of the active layer without resorting to averaged macroscopic parameters such as the ones mentioned above. A microscopic continuum model, thus, models discrete platinum particles and their arrangement in order to improve fuel cell performance and reduce loading. Of work already done, the work by Butel, Ozil, and Durand [8] is of particular interest. Butel et al. found the platinum distribution to be very important for the fast paced reaction at the anode. However, they found this not to be the case at the rate determining much slower reaction at the cathode. Here they found the oxygen reduction reaction to simply be a function of catalyst area, and thus changing from a nondiscrete to a discrete model showed little change in performance of the cathode catalyst layer. The results of my research will show this not to be the case. Butel et al.'s results and other pertinent research regarding fuel cell modeling will be presented in Chapter 2.

1.4 Research Objectives

The research conducted as part of my M.S. degree requirements has taken another look at the reactions in the cathode catalyst layer and whether or not a nondiscrete approximation is sufficient. Various platinum placements and sizes will be used and compared in order to find their effect on fuel cell performance.

The principle objective of this research is to produce a mathematical and computational microscopic continuum model of a PEMFC active layer. This model will be used to do the following:

[1] The phrase "microscopic continuum model" is used here to emphasize the "continuum" nature of the governing equations used to model the structures of a microscopic level. Such a "continuum" approach is distinctive from the statistical (Boltzmann) or even molecular dynamic approaches often used to model structures and transport through such structures at a microscopic level.

1 Test the common nondiscrete catalyst layer assumption and its correspondence to the discrete case.
2 Expand on the nonporous agglomerate models present in the literature by adding pores of various sizes to the geometry.
3 Predict the effect that flooding has on cathode catalyst layer performance.
4 Perform a parametric study in which various geometric parameters are varied in order to determine which arrangements of the active layer provide the best performance.

Chapter 2: Literature Survey

A large number of articles on fuel cell research have been published over the past decade. The fuel cell research which these papers represent can generally be broken down into three levels; system, stack (including single cell), and single cell components(s). At the system level, models are used to investigate each system component from a macroscopic viewpoint. Points of interest include detailed component and system syntheses and designs as well as operation and control. At the stack or single cell level, macroscopic models take into account the various complex phenomena occurring in the fuel cell stack or single cell. At the individual component level of a single cell, both macroscopic and microscopic models are used to determine the performance as well as synthesis/design of a component (e.g., an electrode catalyst layer) or set of components (e.g., a membrane electrode assembly). For example, when modeling an electrode catalyst layer, the individual tracking of species and ions becomes important when trying to enhance fuel cell kinetics and how the geometry of these layers affect overall performance.

The research presented in this thesis models the catalyst layer as a set of individual discrete particles in hopes of finding an optimum loading strategy. In order to begin, a survey of the literature focusing on the catalyst layer of the fuel cell was conducted. A limited number of microscopic models are presented in the subsequent sections due to the lack of research in this area.

2.1 Microscopic Continuum Models

To date, the most recent models found in the literature that focus on discrete catalyst particle modeling in electrode catalyst layers are those written by Bultel, Ozil, and Durand [8]. The authors were some of the first to study catalyst particle sites and placement in some detail back in 1995. Based on my survey of the literature, no other

microscopic continuum models have been produced in the past 5 years that incorporate the transport equations with discrete catalyst sites as modeled in the work of Butel, Ozil, and Durand.

The first study conducted by Butel, Ozil, and Durand [9] describes the effect one platinum particle has on its neighbor. This article presents an overview of the model geometry and governing theory behind the research. Table 2.1 gives a summary of this first attempt at modeling discrete catalyst sites.

Table 2.1: Bultel, Ozil, Durand, and Simonsson [9].

Model	Study of Mass Transfer Within the Active Layer of P.E.M.F.C. Electrodes at the Particle Level (1995)
Authors	Y. Bultel, P. Ozil, R. Durand, and D. Simonsson
Regions	Active Layer
Dimensionality	2D, (X,Y)
Assumptions	Isothermal Equally distributed Pt particles Catalyst particles are spheres having equal diameters Ohmic drop is neglected Homogenous electrochemical kinetic properties Steady-state
Boundary Conditions	A concentration of $C = C_o$ is imposed at the gas-membrane interface A no ion flux boundary condition is applied to any symmetry plane and gas-membrane interface The Butler-Volmer equation is reduced to the Tafel equation and applied to the electrolyte-particle interface.
Governing Equations	$\nabla^2(C) + S_{O_2} = 0$ $i = i_o\left[\exp(\frac{2.3\eta}{b})\frac{C}{C_o}\right]$
Phenomena investigated	The authors introduce 4 different models to find out how big of an impact geometric effects have on mass transfer. - two isolated particles (diffusion and electrochemical kinetics) - a particle deposited on a surface (diffusion) - 2 dimensional hemispheric particles (diffusion) - 3 dimensional spherical particles (diffusion and electrochemical kinetics)
Main conclusions	The authors draw a few main conclusions: i) the geometry of the catalysts particles do not have a very big effect on the oxygen reduction reaction; because the hydrogen oxidation reaction is controlled by diffusion, ii) the geometry of the catalysts particles play a big part in determining the reaction rate.

Limits	This early model was developed to find one platinum particle's effect on concentration. The active layer needs to be considered.

The principal goal of the research summarized in Table 2.1 was to pinpoint one platinum's effect on another. This was demonstrated using four models of increasing complexity. The research finds that modeling discrete catalyst particles at the cathode is not very important due to the slow electrochemical kinetics. However, discrete modeling at the anode is necessary due to the more rapid kinetic behavior in this active layer.

In 1997, Butel, Ozil, and Durand published a paper modeling charge transfer and the effect that ohmic drop has on fuel cell performance [10]. Prior to this article, ohmic loss across the active layer had commonly been ignored. The work presented by the authors proved this to be a bad assumption when considering an active layer with a high porosity. An increase in porosity directly results in a decrease in the electrolyte used to transport the ions across the active layer. Thus, it is important to include this effect when modeling layers with high pore to carbon ratios. This research also showed unexpected local ohmic losses. This has an effect on current density and fuel cell performance. These losses should not be ignored especially when considering thick active layers and large platinum particles. Table 2.2 summarizes the work the authors did when considering ohmic losses.

Table 2.2: Bultel, Ozil, and Durand [10].

Model	Modeling the Mode of Operation of PEMFC Electrodes at the Particle Level: Influence of Ohmic Drop within the Active Layer on Electrode Performance (1997)
Authors	Y. Bultel, P. Ozil, and R. Durand
Regions	Active Layer
Dimensionality	2D, (X,Y), as well as 2D with axisymmetry
Assumptions	Isothermal temperature = 25 °C Equally distributed Pt particles Homogenous electrochemical kinetic properties Steady-state
Boundary Conditions	An overpotential, of $\eta = \eta_o$ is imposed at the active layer-membrane interface. A no ion flux boundary condition is applied to any symmetry plane and gas-membrane interface.

	The Butler-Volmer equation is reduced to the Tafel equation and applied to the electrolyte-particle interface.
Governing Equations	$\nabla(\kappa\nabla(\Phi)) - S_{H^+} = 0$ $i = i_o\left[\exp\left(\frac{-(1-\alpha)nF\lvert\eta\rvert}{RT}\right)\right]$
Phenomena investigated	Previous models assume homogenously mixed catalyst within the active layer. This model considers the catalyst particles to be discrete spheres, thus, taking the platinum's shape and distribution into account. A microscopic continuum model was also developed that studies the ohmic drop encountered with charge transfer in order to find the limitations of the active layer.
Main conclusions	i) When the interparticle distance is less then 10 times the catalyst diameter, one particle's effect on the next is hidden under the electrochemical kinetics. ii) There is a local ohmic effect that must be added to the classical model in order to produce accurate results. iii) This model also finds smaller electrolyte layers and catalysts diameters advantageous to the conductance of ions. iv) There is a negligible ohmic drop when modeling sparsely porous media; yet this effect can not be ignored when modeling largely porous media.
Limits	This model's focus is on ionic drop across the active layer, and, thus, its scope is very narrow. The authors only vary interparticle distance to produce their effectiveness results.

In 1998, Bultel et al. [11] and Bultel, Ozil, and Durand [12] published articles on species transfer as summarized in Tables 2.3 and 2.4. The authors wanted to see whether the concentration and diffusion of species would encounter the same local losses as seen in their previous ion transport study. The model used the same geometry but incorporated mass transfer effects. The first paper summarized in Table 2.3, couples the mass and ion transport equations together. The result of this research was a parametric study looking at particle size and discrete spatial distribution effects.

Table 2.3: Antoine, Bultel, Durand, and Ozil [11].

Model	Electrocatalysis, Diffusion and Ohmic Drop in PEMFC: Particle Size and Spatial Discrete Distribution Effects. (1998)
Authors	O. Antoine, Y. Bultel, R. Durand, and P. Ozil
Regions	Active Layer
Dimensionality	2D, (X,Y), as well as 2D axisymmetry

Assumptions	Isothermal temp = 25 °C Equally distributed Pt particles Homogenous electrochemical kinetic properties Steady-state
Boundary Conditions	A concentration of C= C_o is imposed at the gas pore-electrolyte interface. An overpotential, of $\eta = \eta_o$ is imposed at the active layer-membrane interface. A no ion flux boundary condition is applied to any symmetry plane and gas-membrane interface. The Butler-Volmer equation is reduced to the Tafel equation and applied to the electrolyte-particle interface.
Governing Equations	$\nabla(D\nabla(C)) + S_{O_2} = 0$ $\nabla(\kappa\nabla(\eta)) - S_{H^+} = 0$ $i = i_o\left[\exp(\frac{2.3\eta}{b})\frac{C}{C_o}\right]$
Phenomena investigated	A parametric study on the size and discrete spatial distribution effects on oxygen reduction and hydrogen oxidation.
Main conclusions	The authors conclude that: i) the discrete distribution of catalyst particles is not very important when considering oxygen reduction; ii) the size effect is only a catalytic one, meaning that the catalyst effective area is what really matters rather then where and how are they arranged at the cathode; iii) the smaller the particles are the better for the hydrogen oxidation since this helps limit the local diffusion effects.
Limits	The authors only varied the Pt size and did not keep the loading the same. Thus, constant loading with Pt size differing still needs to be evaluated as does interparticle distance.

The model of Table 2.3 does not show evident changes in the oxygen reduction reaction with particle size. However, the hydrogen oxidation reaction is quite dependent upon catalyst size and placement. In fact, smaller catalyst particles produce better results for a given reaction.

The second of the 1998 papers is summarized in Table 2.4 and details the concentration drop as seen around the catalyst particles. Ion transfer was ignored in this work so that spherical diffusion could be exclusively investigated.

Table 2.4: Bultel, Ozil, and Durand [12].

Model	Modeling of Mass Transfer within the PEM Fuel Cell Active Layer: Limitations at the Particle Level (1998)
Authors	Y. Bultel, P. Ozil, and R. Durand

Regions	Active Layer
Dimensionality	2D, (X,Y), as well as 2D with axisymmetry
Assumptions	Isothermal temperature = 25 °C Equally distributed Pt particles Ohmic resistances are neglected Homogenous electrochemical kinetic properties Steady-state
Boundary Conditions	A concentration of C= C_o is imposed at the gas pore-electrolyte interface. . A no ion flux boundary condition is applied to any symmetry plane and gas-membrane interface. The Butler-Volmer equation is reduced to the Tafel equation and applied to the electrolyte-particle interface.
Governing Equations	$\nabla(D\nabla(C))+S_{O_2}=0$ $r=\kappa(\frac{C}{C_o})$
Phenomena investigated	This model uses the geometry from previous work to study the local mass transfer and the effect that discrete catalyst particles have on the concentration throughout the active layer.
Main conclusions	This model demonstrates a local spherical diffusion effect that has been ignored in classical models. This local diffusion acts in addition to classical planar diffusion. This diffusive effect is much more apparent with the oxidation of hydrogen then with the reduction of oxygen.
Limits	This model's focus is only on concentration drop across the active layer and, thus, has a very narrow scope. The authors only vary interparticle distance and overpotential in their parametric study. Thus, there is a wide range of other variables to consider.

In the work summarized in Table 2.4, a concentration gradient is formed due to the planar diffusion of the oxygen species, across the active layer. Additional detail demonstrates the spherical diffusion effect around each particular catalyst particle. The author's conclude that this effect alters the overall concentration and should be considered when calculating current density.

After Antoine, Butel, Ozil, and Durand [11] illustrated that discrete modeling of catalyst particles is important for both ion and species transport (Table 2.3), Bultel, Ozil, and Durand conducted a final more detailed study of the coupled effects [8]. The local ohmic and spherical diffusion resistances are again combined in order to capture the effects of the ion and species transport. Table 2.5 summarizes the authors' most recent and complete work on discrete catalysts placement. Their main conclusion is that

limitations at the particle level are insignificant for the oxygen reduction at the cathode; and, thus, the classical non-discrete model is sufficient.

Table 2.5: Bultel, Ozil, and Durand [8].

Model	Concentration and Potential Distributions in the Active Layer of Proton Exchange Membrane Fuel Cell Electrodes (2000)
Authors	Y. Bultel, P. Ozil, and R. Durand
Regions	Active Layer
Dimensionality	2D, (X,Y), as well 2D with axisymmetry
Assumptions	Isothermal Temp = 25 °C Equally distributed Pt particles Homogenous electrochemical kinetic properties Steady-state
Boundary Conditions	A concentration of C= C_o is imposed at the gas pore-electrolyte interface. An overpotential, of $\eta = \eta_o$ is imposed at the active layer-membrane interface. A no ion flux boundary condition is applied to any symmetry plane and gas-membrane interface. The Butler-Volmer equation is reduced to the Tafel equation and applied to the electrolyte-particle interface.
Governing Equations	$\nabla(D\nabla(C)) + S_{O_2} = 0$ $\nabla(\kappa\nabla(\eta)) - S_{H^+} = 0$ $i = i_o\left[\exp(\frac{2.3\eta}{b})\frac{C}{C_o}\right]$
Phenomena investigated	This model expands on the work summarized in Table 2.3 to study the local mass transfer and ionic drop across the active layer of a fuel cell. The discrete model is compared to the classical continuous model to note the effect that individual catalyst particles have on the model's predictions.
Main conclusions	This work demonstrates the importance of considering the discrete distribution of catalyst particles when modeling mass and charge transfer. The effect of spherical diffusion and ohmic drop near the catalyst particle are important to consider and their effects on current density. This study also shows the ohmic drop to be important. Commonly it is neglected when modeling the active layer. Finally, the authors conclude that in the case of oxygen reduction, the classical non-discrete model is acceptable.
Limits	This model is much more complete then the previous work, focusing on both concentration and ohmic drops across the active layer. The authors however do not vary many parameters. Thus, a complete parametric study is missing.

2.2 Nondiscrete Cathode Catalyst Layer Models

Gloaguen et al. [13] considers an agglomerate model similar to the work done by Butel, Ozil and Durand [8], but do not model individual catalyst particles. Table 2.6 summarizes this work and shows that the same geometry (without discrete particles) and equations were used in this model as in the work of Butel, Ozil, and Durand.

Table 2.6: Gloaguen, Convert, Gamburzev, Velev and Srinivasan [13].

Model	An Evaluation of the Macro-homogeneous and Agglomerate Model for Oxygen Reduction in PEMFC's (1998).
Authors	F. Gloaguen, P. Convert, S. Gamburzev, O. A. Velev and S. Srinivasan
Regions	Active Layer (cathode)
Dimensionality	2D, (X,Y)
Assumptions	Isothermal Equally mixed Pt particles Homogenous electrochemical kinetic properties Steady-state
Boundary Conditions	A concentration of $C=C_o$ is imposed a the active layer-gas interface. The relation $E=E_o - \eta(L)$ is applied at the catalyst layer-electrolyte interface. A no flux boundary condition is applied to any symmetry plane and gas-membrane interface The Butler-Volmer equation based upon overpotential and concentration is applied at the membrane-particle interface.
Governing Equations	$\nabla(D\nabla(C)) + S_{O_2} = 0$ $\nabla(\kappa\nabla(\eta)) - S_{H^+} = 0$ $i = Hi_o\left[\exp(\frac{2.3\eta}{b})\frac{C}{C_o}\right]$ where H is a temperature based correction factor
Phenomena investigated	An experimental and numerical evaluation into the electrochemical kinetics of oxygen reduction in the cathode active layer.
Main conclusions	One major finding for this paper is that one can not simulate a gas pore with a macro-homogeneous model, the diffusion overpotential is overestimated. However, using an agglomerate model when modeling pores is a valid solution.
Limits	The authors did not discretely model the platinum particles. There was also little parametric study conducted.

Although the model presented by Gloaguen et al [13] is not discrete, it is still

important to consider. The authors reconfirmed the use of an agglomerate model when modeling pores.

In 2002 Genevey et al. [14] published a model based on the transient modeling of the cathode catalyst layer. This model includes the effects of heat, mass, and charge transport as well as electrochemistry within the cathode catalyst layer. Table 2.7 gives a brief summary of this research.

Table 2.7: Genevey, von Spakovsky, Ellis, Nelson, Olsommer, Topin, and Siegel [14].

Model	Transient Model of Heat, Mass, and Charge Transfer as well as Electrochemistry in the Cathode Catalyst Layer of a PEMFC (2002)
Authors	D. B. Genevey, M. R. von Spakovsky, M. W. Ellis, D. J. Nelson, B. Olsommer, F. Topin, and N. Siegel
Regions	Active Layer (catalyst layer)
Dimensionality	1D
Assumptions	Equally mixed Pt particles Electro-neutrality in the membrane Homogenous electrochemical kinetic properties Fully developed flow Gravity is neglected Constant voltage potential in the porous media
Boundary Conditions	A concentration of oxygen is imposed on the active layer-gas interface. A value for the potential Φ_c in the carbon phase is specified. The potential Φ_m is set to zero at the membrane interface, and the proton current is set to zero at the backing layer interface.
Governing Equations	$\frac{\partial i}{\partial x} = \frac{\partial i_c}{\partial x} = \frac{1}{1-\varepsilon_m}\frac{\partial i_c^{app}}{\partial x}$ $\frac{\partial i}{\partial x} = a i_o \left[\exp\left(\frac{\alpha_a F(\Phi_c - \Phi_m}{RT} \right) - \exp\left(\frac{-\alpha_c F(\Phi_c - \Phi_m}{RT} \right) \right]$ -where i_o is concentration dependent $\varepsilon s^{\alpha} \frac{\partial c_i^{\alpha}}{\partial t} + \varepsilon c_i^{\alpha} \frac{\partial s^{\alpha}}{\partial t} = -\frac{\partial N_i^{\alpha}}{\partial x} - \frac{1}{M_i} \dot{m}_i^{\alpha \to \beta} - \dot{n}_i^{\alpha}$ $\frac{\partial \Phi_m}{\partial x} = -\frac{i_m^{app}}{\kappa_m^{app}} + \frac{F}{\kappa_m^{app}} C_{H^+} u^m$ The following is a list of equations used in this research but, not applicable to our model: Governing Equations- momentum equation, energy equation, ohm's law Constitutive Relations- void fraction calculation, state equation, capillary pressure equation, water vapor pressure calculation, mixture equations, water activity relations (please

	see reference for a detailed description [5])
Phenomena investigated	The current limiting the oxygen reduction reaction was explored through this transient model in order to reduce the amount of platinum used in the active layer.
Main conclusions	i) Higher porosity and catalyst loading are desirable to fuel cell performance. ii) High temperature was seen to have a negative effect on catalyst layer performance. iii) A limiting current is evident when the oxygen concentration at the membrane-active layer interface goes to 0.
Limits	The authors did not discretely model the platinum particles.

Using the equations described in Table 2.7, the authors were able to conclude that higher porosity and catalyst loading are beneficial to a fuel cell's performance. Furthermore, an increase in temperature had an adverse affect on the performance of the catalyst layer.

2.3 Multi-Layer Models

Siegel et al. [6] present a model which describes the performance of a PEMFC based on an agglomerate electrode catalyst layer geometry. The authors used CFDesign™ and FEMAP™ in order to develop a two-dimensional agglomerate catalyst model. Table 2.8 presents their model and main conclusions.

Table 2.8: Siegel, Ellis, Nelson, and von Spakovsky [6].

Model	Single Domain PEMFC Model Based on Agglomerate Catalyst Geometry (2002)
Authors	N. P. Siegal, M. W. Ellis, D. J. Nelson, and M. R. von Spakovsky
Regions	Proton Exchange Membrane Fuel Cell
Dimensionality	2D
Assumptions	Steady-state Equally mixed Pt particles Homogenous electrochemical kinetic properties Fully developed flow Gravity is neglected

	Constant voltage potential in the porous media
Boundary Conditions	Concentration of oxygen is specified at the cathode inlet and there is a no flux condition at the exit. There is a no flux membrane potential condition present at the inlet and exit of the cathode. There is a non flux condition applied to all remaining external surfaces.
Governing Equations	$\nabla(D\nabla(C)) - \bar{u}\nabla C + S_{O_2} = 0$ $\nabla(\kappa\nabla(\eta)) - S_{H^+} = 0$ $BV = nF/((\partial/a)/C^* D_{m,k}) + 1/kE$ $k = A_{vl} i_{o,e} / nF(C^*/C_{k,ref})^{\gamma}[e^{(\phi_c-\phi_m)\alpha_a F/RT} - e^{-(\phi_c-\phi_m)\alpha_c F/RT}]$ $C^* = h_{d,e} T C_k$ $E = \tanh(mL)/mL$ $mL = L\sqrt{k/(C^* D_{m,g})}$ $D_k = [((1 - C_k MW_k)/\rho)/\sum_{k\neq j}(C_j/C_{tol} D_{jk})]\tau^{1.5}$ $D_m = 1.3E-4e^{2416(1/303)-(1/T)}$ $\kappa_m = (0.005139\lambda - 0.000326)e^{(1268/(1/303)-(1/T))}(\tau_g \tau_m)$ $\lambda = C_m/((MW_m/\rho_m) - 0.0126C_m)$ The following is a list of equations used in this research but, not applicable to our model: Governing Equations- momentum equation, energy equation, global continuity equation, (please see reference for a detailed description [6])
Phenomena investigated	To model a proton exchange membrane fuel cell with specific interest in species transport, electrochemical kinetics, energy transport, current distribution, and water uptake and release in the electrode catalyst layer.
Main conclusions	The catalyst void fraction has a notable effect on fuel cell performance with 0.04 being optimum at η=0.5V. Thinner catalyst layers are desirable to overcome diffusive resistances.
Limits	A microscopic approach would aid this research and further evaluate the optimum void fraction.

From the model, the authors conclude that a more porous media up to a certain limit aids in fuel cell performance do to enhanced species diffusion throughout the electrode catalyst layer. Siegel et al. also found how much a thinner electrode catalyst layer reduces the ohmic drop across it.

In 2003, Siegel et al. [7] expanded their research to include a computational model of a PEMFC that included liquid water transport. Table 2.9 gives a summary of the basic assumptions, equations, and conclusions presented in their work.

Table 2.9: Siegel, Ellis, Nelson, and von Spakovsky [7].

Model	A Two-dimensional Computational Model of a PEMFC with Liquid Water Transport (2003)
Authors	N. P. Siegal, M. W. Ellis, D. J. Nelson, and M. R. von Spakovsky
Regions	Proton Exchange Membrane Fuel Cell
Dimensionality	2D
Assumptions	Steady-state Equally mixed Pt particles Homogenous electrochemical kinetic properties Fully developed flow Gravity is neglected
Boundary Conditions	Concentration of oxygen is specified at the cathode inlet and there is a no flux condition at the exit. There is a no flux membrane potential condition present at the inlet and exit of the cathode. There is a non flux condition applied to all remaining external surfaces.
Governing Equations	$\rho^g \bar{u} \cdot \nabla wo_2 + wo_2 \nabla \cdot (\rho^g \bar{u}) = \nabla \cdot (D^g_{o_2} \rho^g \nabla wo_2) + S_{O_2}$ $\nabla \cdot (\varepsilon_p \kappa_{H^+} \nabla \Phi_{H^+}) + S_{H^+} = 0$ The following is a list of equations used in this research but, not applicable to our model: Governing Equations- global continuity equation, momentum equation, and energy equation (please see reference for a detailed description [7])
Phenomena investigated	To model a proton exchange membrane fuel cell with specific interest in the transport of liquid water, gaseous species, protons, energy, and water dissolved in the ion conducting polymer.
Main conclusions	This papers main conclusion is that liquid water transport must be considered when modeling a fuel cell. If omitted the performance of the fuel cell is overestimated. The model also shows that 20-40% of the water at the cathode travels across the membrane.
Limits	A microscopic approach would aid this research and further evaluate water transport and predict flooding.

The authors investigate the transport of liquid water, gaseous species, protons, energy and water through the catalyst layer. One of their major findings is that water transport must be considered when trying to accurately model the electrode catalyst layer. Otherwise the performance of the fuel cell is overestimated.

2.4 Parameter Evaluations

When modeling the electrode catalyst layer of a fuel cell, transport and electrochemical kinetic parameters are very important to performance. These parameters directly affect the transport phenomena and alter the cell's overall current density. There are three sources for these parameters used for comparison purposes in this research, namely, Parthasarathy, Srinivasan, and Appleby [14], Beattie, Basura, and Holdcroft [15], and Zang, Ma, and Mukerjee [16]. The mass transport properties exhibit similar trends but somewhat different magnitudes between Beattie, Basura, and Holdcroft [15], and Zang, Ma, and Mukerjee [16] and significantly different magnitudes of both papers with Parthasarathy, Srinivasan, and Appleby [14]. As to the kinetic parameters, there is a variance in trends between the three papers and at times significant differences in magnitudes (i.e. the Tafel slope and the exchange current density). The large variance in data can be attributed to inadequate measuring equipment or procedures. Difficulties arise when trying to produce consistent results due to contact resistances between the measuring devices and the active layer. The parameters chosen for this study were taken from the research conducted by Zang, Ma, and Mukerjee [16] due to theirs being the most recent and complete (for example, data for both temperature and pressure variations is given).

In 1992 Parthasarathy, Srinivasan, and Appleby [14] investigated various mass transport and kinetic parameters in a Platinum/Nafion interface. These early studies used a thin platinum wire encased in Nafion. This wire was used to simulate the electrode catalyst layer, and the study was conducted at varying temperatures.

Table 2.10: Parthasarathy, Srinivasan, and Appleby [14].

Model	Temperature Dependence of the Electrode Kinetics of Oxygen Reduction at the Platinum/Nafion Interface-A Microscopic Investigation (1992).
Authors	A. Parthasarathy, S. Srinivasan, and A. J. Appleby
Phenomena investigated	Mass-transport parameters for oxygen in Nafion were obtained at various temperatures. A variation of electrochemical kinetic parameters with temperature at the Pt/Nafion interface was also investigated.

Main conclusions	There are two sets of electrochemical kinetic parameters: one for low current density and one for high current density. This is due to the presence of oxide on the platinum surface at low current densities. This thin layer eventually burns off at high current densities. Furthermore, diffusion of oxygen in Nafion increases with temperature whereas solubility decreases. The product of the two increases with temperature; thus, mass transport also increases with temperature. Most kinetic parameters are found to increase with temperature.

Parthasarathy, Srinivasan, and Appleby [14] found the permeability, k_P, defined by

$$k_P = DC \tag{2.1}$$

to increase with temperature. The Tafel slope also has a temperature dependency. All experiments were conducted using a pressure for oxygen of 5 atm and a relative humidity of 100%.

Beattie, Basura, and Holdcroft [15] presented a similar study to that of Parthasarathy, Srinivasan, and Appleby [14]. The mass transport and kinetic parameters were explored at varying temperatures and pressures. Calculations were conducted using a 50 μm platinum disk electrode and two solid polymer electrolyte membranes. Table 2.11 displays the finding of this research.

Table 2.11: Beattie, Basura, and Holdcroft [15].

Model	Temperature and Pressure Dependence of O_2 Reduction at PT/Nafion 117 and PT/BAM 407 Interfaces (1999)
Authors	P. D. Beattie, V. I. Basura, and S. Holdcroft
Phenomena investigated	Mass transport and electrochemical kinetic parameters were established for oxygen in Nafion in this research. These parameters were evaluated at varying temperatures and pressures. The authors also found oxide covered and non-oxide based parameters for varying current densities.
Main conclusions	The activation energies and diffusion of oxygen were found to be much smaller in BAM® 407 then in traditional Nafion® 177. The exchange current density was found to be lower for BAM® 407 then Nafion® 177 at low current densities and the opposite at high current densities. Both BAM® 407 and Nafion® 177 were found to obey Henry's law to a first approximation.

Beattie, Basura, and Holdcroft [15] conclude that there are two different kinetic regions: one for low current densities and one for high current densities. The change in

kinetics at low current densities can be attributed to the oxide covered Platinum. The authors saw the same general trends and magnitudes in the mass transport parameters as did Parthasarathy, Srinivasan, and Appleby [14]. However, although the kinetic parameter trends for the exchange current density with temperature found by Beattie, Basura, and Holdcroft follow the same trends as those in Parthasarathy, Srinivasan, and Appleby [14], their magnitudes cannot be directly compared. Since one set (Beattie, Basura, and Holdcroft [15]) is measured at 3atm while the other (Parthasarathy, Srinivasan, and Appleby [14]) is measured at 5atm. Nonetheless, the trends with respect to pressure do appear (based on Zang, Ma, and Mukerjee [16]) to be correct. Unfortunately, when it comes to the transfer coefficient it is difficult to know which set of data values are correct (Beattie, Basura, and Holdcroft [15]) or (Zang, Ma, and Mukerjee [16]) neither the magnitudes nor trends are the same between the two papers.

In 2004, Zhang, Ma, and Mukerjee [16] conducted a study to examine the electrochemical kinetic and mass transfer parameters for oxygen reduction. This study used varying temperatures and pressures for each parameter as did the research performed by Beattie, Basura, and Holdcroft [16]. A microelectrode was placed on Nafion 117 and sulfonated poly(arylene ether sulfone) membranes. A brief summary of this research is presented in Table 2.12.

Table 2.12: Zhang, Ma, and Mukerjee [16].

Model	Oxygen Reduction and Transport Characteristics at a Platinum and Alternative Proton Conducting Membrane Interface (2004)
Authors	L. Zhang, C. Ma, and S. Mukerjee
Phenomena investigated	Investigation into mass transfer and electrochemical kinetic parameters for oxygen reduction in Nafion and sulfonated poly(arylene ether sulfone) membranes. These parameters where studied with varying temperature and pressure at 100% relative humidity.
Main conclusions	Using slow-sweep voltammetry and chronoamperometry varying electrode kinetic and mass transport parameters were investigated. Low and high current density regions where found for the kinetic parameters. The overall permeability (DC) was found to increase with temperature and pressure.

The data collected by Zhang, Ma, and Mukerjee [16] shows similar trends for the exchange current density to the two previous studies, although differences in magnitude

with those of Beattie, Basura, and Holdcroft [15] are significant[2]. Transfer coefficient trends are not consistent with those of either of the other two papers while magnitudes are significantly different from those found in Beattie, Basura, and Holdcroft [15][3]. Zhang, Ma, and Mukerjee also find similar low and high current regions for the kinetic parameters as did Beattie, Basura, and Holdcroft [15] and an increase in permeability for temperature and pressure as did Parthasarathy, Srinivasan, and Appleby [14]. This paper covers a large range of temperatures (303 to 353K) as well as oxygen pressures (0.41 to 4 atm) and is the most recent.

2.5 Contribution to the Body of Research

In order to initiate my research the work done by Bultel, Ozil, and Durand [8] was replicated and validated. The authors' conclusion that the reduction reaction is not significantly affected when using a discrete as opposed to a nondiscrete catalyst distribution was then explored because it was felt that the reduction reaction should directly depend on particle placement within the electrode catalyst layer. The same axisymmetric agglomerate model was used as in Butel, Ozil, and Durand [8] to study in detail discrete platinum placement and its effect on the performance of the cathode catalyst layer. This particular model is described in Chapter 3.

A new porous microscopic continuum model incorporating discrete platinum sites in the electrode catalyst layer was also implemented. It is described in detail in Chapter 3. For this model mass transfer and electrochemical kinetic parameters from Zhang, Ma, and Mukerjee [16] were used.

[2] Note that a direct comparison of magnitude with Parthasarathy, Srinivasan, and Appleby [14] is not possible because of the difference in pressures.

[3] Note again that a comparison of magnitude with Parthasarathy, Srinivasan, and Appleby [14] is not possible due to differences in pressure

Chapter 3: The Mathematical Model

An investigation was conducted into the microscopic effects that various transport, electrochemical kinetic, and geometric parameters have on the electrode catalyst layer of a proton exchange membrane fuel cell. For example, the inter-particle effect that one catalyst particle has on its' neighbor was examined with regard to how it relates to overall performance of the fuel cell. Although proton exchange membrane fuel cells, (PEMFCs), can be fairly accurately modeled at a macroscopic level using the appropriate transport relations and computational fluid dynamics solvers, they are not able to predict in detail the structure required in the electrode catalyst layers at a microscopic level. Thus, microscopic models are needed to show the effect of, for example, catalyst particle size and placement on performance so that new designs of electrode catalyst layer geometries can be made.

Chapter 3 describes the assumptions, equations, boundary conditions, and initial conditions used when formulating the microscopic continuum models developed here. Assumptions such as isothermal and isobaric conditions are made to ease the solution process when no great change in temperature or pressure occurs. Governing equations are for species and charge transport. Boundary conditions specify species concentrations or loads.

The first set of microscopic models presented will be those of Bultel, Ozil, and Durand [8]. There are two: a Thin Film Model and an Agglomerate one. The Thin Film Model assumes that all the catalyst particles at some depth are located inside a thin film of electrolyte which sits below a gas pore (see Figure 3.1a). The thickness of the electrolyte film covering the catalyst particles is constant and very small in comparison to the pore size. The Agglomerate Model assumes the catalyst particles to be uniformly dispersed within the electrolyte phase forming a homogeneous mixture of electrolyte and catalyst (see Figure 3.1b). Both models were implemented and validated using the results of Bultel, Ozil, and Durand [8]. We begin with a discussion of the Thin Film Model.

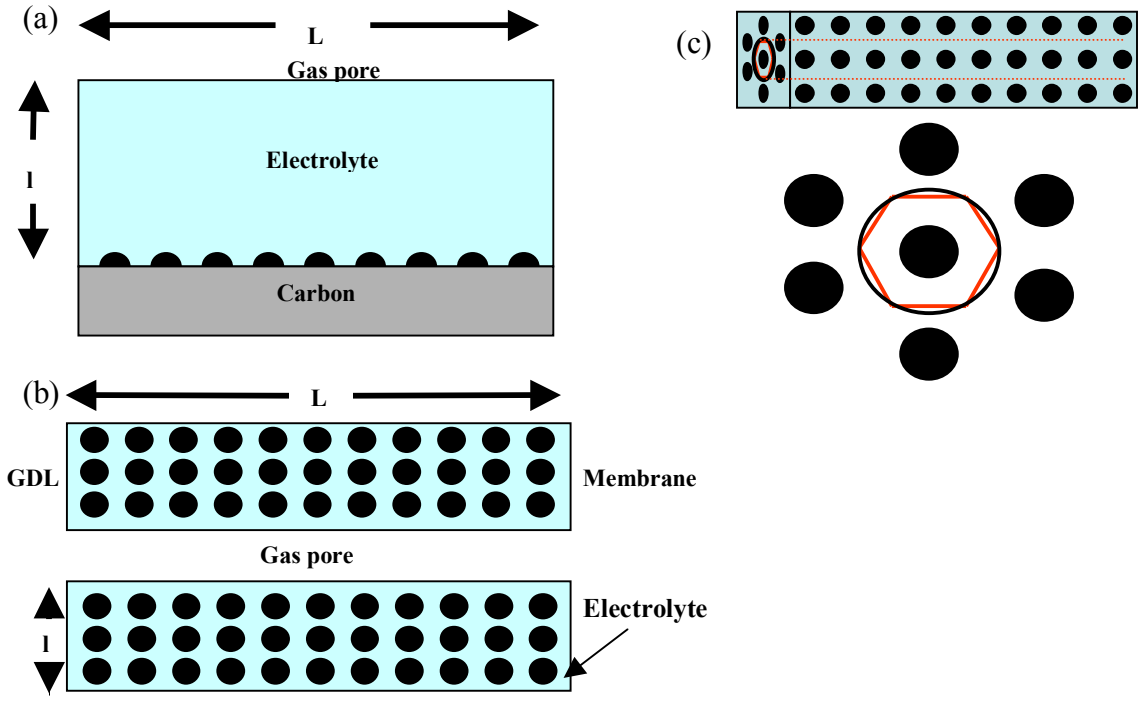

Figure 3.1: a) Hexagonal 2D network of hemispheric particles (Thin Film Model; upper figure); b)Hexagonal 3D network of particles (Agglomerate Model; lower figure); c) Hexagonal networks of symmetric platinum particles (applicable to both cases).

3.1 Thin Film Model From the Literature

The Thin Film Model (Bultel, Ozil, and Durand [12]) includes catalyst particles deposited on a carbon surface surrounded by electrolyte as shown in Figure 3.1a. The electrolyte is in contact with a gas pore providing species to the model. There is an axisymmetric symmetry evident in this geometry shown above even more clearly by the dotted-line rectangle in Figure 3.2. Utilizing this, one can use a set of axisymmetric equations to simulate a 3D geometry with a 2D model.

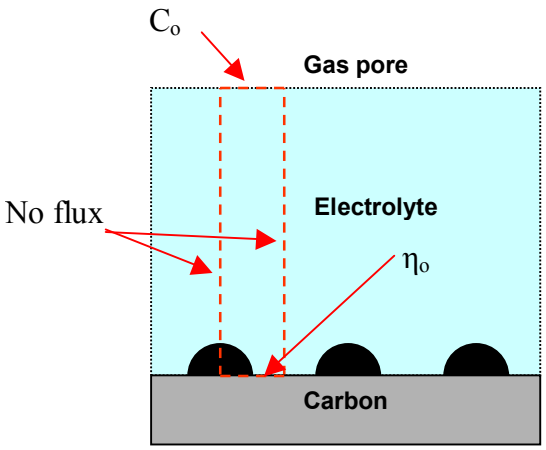

Figure 3.2: The Thin Film Model, with the axisymmetric symmetry displayed by the dotted line rectangle.

3.1.1 Model Assumptions

The assumptions for the Thin Film Model are as follow:

- The Nafion (electrolyte) thickness and interparticle distance are constant.
- There is no flux across all symmetry planes except the gas pore/electrolyte interface.
- Cylindrical symmetry is used to approximate the hexagonal symmetry.
- Pure oxygen is exposed to the gas diffusion layer/agglomerate interface at 1 atm.
- The porosity is zero, throughout the model.
- The process of diffusion is isothermal.
- The system is at steady state.

3.1.2 Model Equations

The Thin Film Model incorporates the following governing equation for the diffusive transport of oxygen, where D is the diffusion coefficient and C is the concentration for O_2 in Nafion:

$$\nabla \bullet (D_{O_2} \nabla (C_{O_2})) + S_{O_2} = 0 . \qquad (3.1)$$

In equation (3.1) the concentration of oxygen in Nafion is equal to the solubility at the gas pore/electrolyte interface. The rate of consumption at the surface of the catalyst is

$$\dot{n} = \frac{i}{4F}, \tag{3.2}$$

where $\dot{n}$ is the flux of O_2 consumed by the electrochemical reaction, i is the current density, and F is Faraday's constant. Thus, equation (3.1) controls species transfer within the model and equation (3.2) acts as a sink/source at the platinum surface. Equations (3.1) and (3.2) are solved simultaneously with the appropriate boundary conditions.

3.1.3 Boundary and Initial Conditions[4]

Boundary conditions are placed at the platinum surface and gas pore/agglomerate interface. A fixed concentration is used at the gas pore/agglomerate interface, while a null flux density is set at each line of symmetry as shown in Figure 3.2. A flux boundary condition dependent on species consumption, equation (3.2), is placed at the platinum particle surface. From this equation current density can be calculated, and concentration throughout the active layer can be evaluated.

Values utilized for the concentration, flux, and diffusion coefficient are shown in Table 3.1.

Table 3.1: Boundary conditions and diffusion coefficient values for The Thin Film Model.

Condition	Value	Location
C	2.82508e-18 mol/μm^3	Gas pore/agglomerate interface
D	79.433 μm^2/sec	Nafion
$\dot{n}$	-6e-17 molO_2/μm^2 sec	PT surface

The concentration boundary condition is derived from the solubility of O_2 in Nafion. The only initial condition in this model is that the concentration of O_2 throughout the Nafion is equal to its solubility in Nafion. Both diffusion and solubility data for O_2 were taken from Zhang, Ma, and Mukerjee [16].

[4] Note that even though the model is not transient, the CFD solver, CFDesign™, requires initial conditions in order to converge to a solution.

3.1.4 Geometric Configuration

The 2D axisymmetric geometry was constructed using FEMAP™, a finite element geometry modeling program. Table 3.2 displays the dimensions for the Thin Film Model.

Table 3.2: Thin Film Model geometry.

Platinum Radius	2.05 nm
Nafion Cylindrical Radius	10.25 nm
Nafion Cylindrical Length	1000 nm

These dimensions were derived from values listed in Bultel, Ozil, and Durand [8] such as the interparticle distance to mean particle diameter and active layer thickness to mean particle diameter ratios. From this data, the real geometry was constructed and implemented in the geometric modeling software.

Figure 3.3 displays the mesh for this geometry in FEMAP™. A platinum particle is shown in the lower right hand corner of the model. The mesh is refined near the Pt surface. Even though the model appears to be two-dimensional, it is actually programmed in three dimensions by incorporating axial symmetry about the Y-axis. When implementing axisymmetric symmetry, the Y-axis is fixed and the model is allowed to revolve around it, forming a cylinder. The Y-axis is as shown in Figure 3.3.

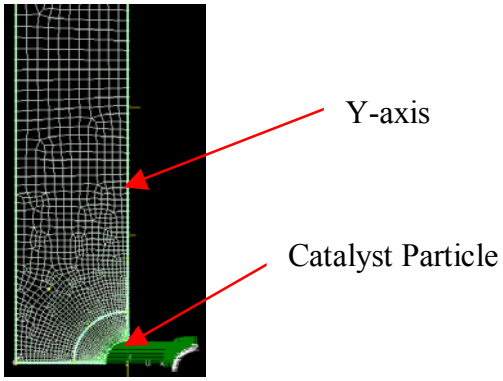

Figure 3.3: FEMAP Thin Film Model mesh.

The model is solved using CFDesign™, which is commercial finite element computational fluid dynamic software developed and marketed by Blue Ridge Numerics

Inc. (BRNI) and specifically modified by BRNI for Virginia Tech (VT) so that it could be used to solve the macroscopic and microscopic fuel cell continuum models developed at VT. Solution of the model results in the concentration distribution of oxygen throughout the electrode catalysts layer. These results are presented in Chapter 5.

3.1.5 Meshing Attributes

Using FEMAP™ a finite element generation pre- and post-processing software, the mesh for a fuel cell active layer can be developed. Such a mesh is then coupled with the finite element solver, CFDesign™ developed by Blue Ridge Numerics Inc. (BRNI) in order to resolve the electrochemical reaction and transport of ions and O_2 species across the active layer. Using FEMAP™, meshes can be generated manually or automatically. The automeshing utility is very useful when mapping large sections of geometry and works best when the number of nodes on a curve is specified. Figure 3.4 displays a

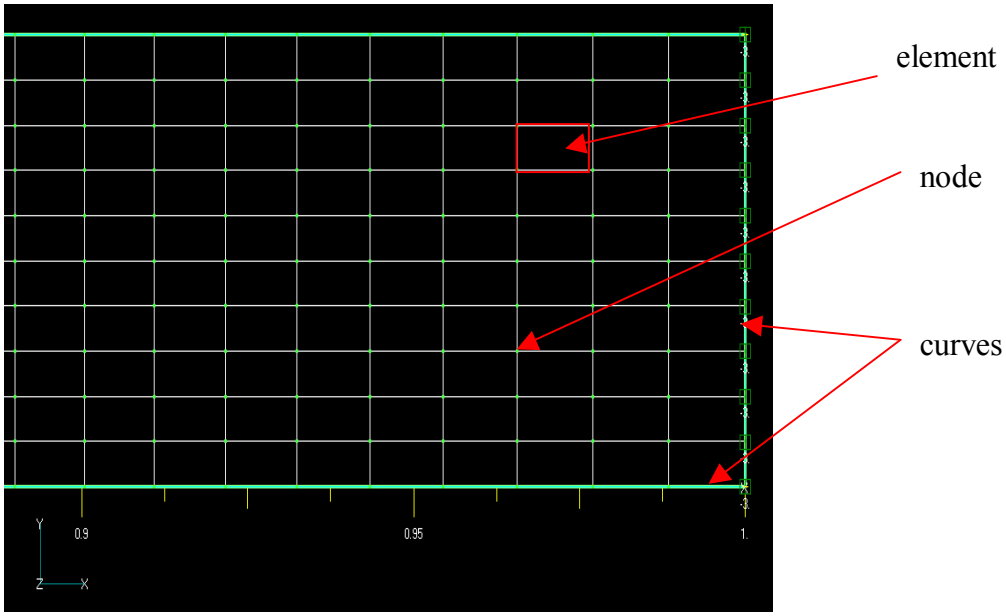

Figure 3.4: Finite element mesh on a geometry using the FEMAP™ automeshing utility.

section of a geometry that is automeshed using the FEMAP™ mesh generating software. Hexahedral elements are easily distinguished in Figure 3.4 as well as the corresponding nodes present at each corner. Since the numerical equations are solved at each node, care

has to be taken to create a consistent and sufficiently fine mesh for the particular conditions.

However, automeshing has uniformity issues when meshing complex geometries. This can be alleviated using a mapped mesh which creates a uniform mesh around a bend or on less than ideal surface, e.g., a platinum particle. To map mesh, one selects a particular three or four sided surface and indicates to FEMAP™ how many nodes to place on each curve (opposing curves must have the same number of nodes for uniformity). This tool has been used a great deal throughout this research and is capable of creating the mesh shown in Figure 3.5.

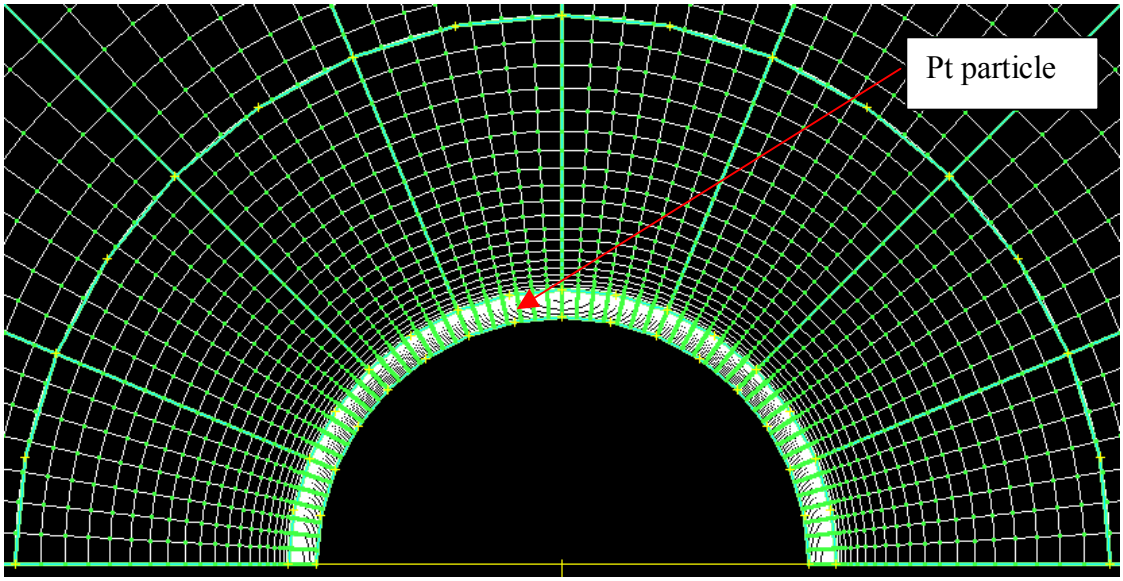

Figure 3.5: Finite element mesh around a Pt particle using the FEMAP™ mapped meshing utility.

With map meshing, one is able to form uniform elements around circular surfaces like the platinum particle's surface shown in Figure 3.5. Here, the O_2 species concentration and ion transport gradients are very high. Thus, finer elements are needed to produce valid results. Biasing enables a mesh to concentrate it's nodes towards a particular region and is first applied to the curves before meshing takes place. Biasing is also important to the runtime of a model. By forming a fine mesh where gradients are rapidly changing and a course mesh around areas of less variance, one is able to efficiently use processing power where it is needed.

One should also note that the geometry in Figure 3.5 is broken down into smaller surfaces. This sectioning promotes an even more uniform and efficient mesh. Mapped meshing is a great tool but it has faults when trying to mesh drastic change like the sphere shown in Figure 3.2. Thus, the platinum particle and surrounding areas are broken down into smaller surfaces and each is mapped meshed.

Hexahedral elements are recommended by FEMAP™ and are best for a uniform three to four sided structure like the ones previously shown in Figure 3.6. However, when dealing with an even more obtuse geometry like the six sided one shown in Figure 3.6, tetrahedral elements are better. Tetrahedral elements are beneficial due to their ability to mesh peculiar surfaces like the one shown in Figure 3.6.

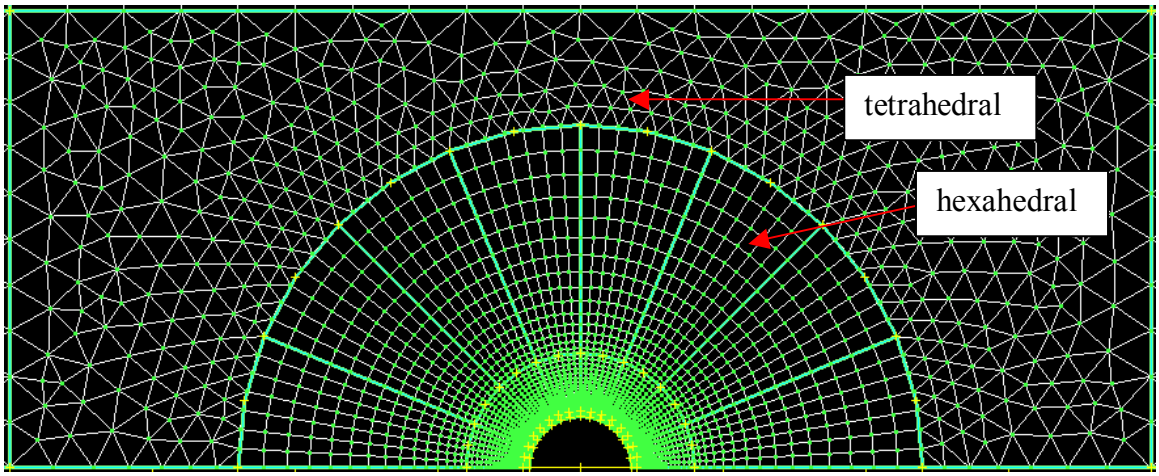

Figure 3.6: Finite element mesh around a Pt particle with hexahedral elements and tetrahedral elements using the FEMAP™ mapped meshing utility.

In this research, it was very important to reduce the runtime (time is takes for the model to converge). One of the easiest ways to do this is to reduce the number of nodes within a geometry, the tradeoff being a less accurate result. There is a mid-point for a particular geometry, where the mesh is fine enough to produce accurate results, yet coarse enough to alleviate unnecessarily long solution times. The art of finding this point is instrumental to this research. Notice above how all of the nodes surround the platinum particle. Thus, if one is to make a noticeable decrease in convergence time, one must focus on this region. By trial and error, the number of nodes where increased close to the platinum particle until consistent results where obtained. It was found that using node

spacing on the order of 1e-6 μm to 1e-7 μm produced valid results at acceptable runtimes. Thus, this kind of biasing was implemented into all of the model meshes. It was also found that node spacing as coarse as 1e-3 μm in regions where big variances in gradients do not appear were acceptable for accurate results.

Another important variable with respect to runtime is the dimensionality of the model. If a dimension in the x-direction is 100 times what it is in the y-direction, runtime time is negatively effected. For the porous agglomerate model with a length equal to 1μm, the x-direction to y-direction ratio is 20. Solution times for this model take approximately 7 minutes for a given point on a polarization curve with 45,000 nodes. However, for the 20μm length model with close to the same number of nodes, runtime increases to approximately 4 hours. Table 3.3 shows rough estimates of solution time for different geometries and different number of nodes on an AMD 2600+ Athlon processor with 1Gb of RAM.

Table 3.3: Approximate runtimes for various geometries and number of nodes (to fit one point on a polarization curve).

number of nodes	**L=1μm**	**L=10μm**	**L=20μm**
≈ 50,000	6.6 minutes	1.5 hours	4 hours
≈ 200,000	3 hours	12 hours	1 day
≈ 400,000	1 day	2 days	3 days

Although these runtimes seem very long they used to be much longer before proper meshing techniques were employed and the model was nondimensionalized[5], they were significantly longer. Another way to reduce runtimes was to increase the diffusion coefficient of O_2 in the platinum source/sink volume[6]. With this increase, the platinum particle saw less of a gradient across it; and much courser meshes on the platinum volume could be used as shown in Figure 3.7. Another way to aid convergence is to increase the number of internal iterations. CFDesign™ has both global and internal interactions in which the matrix solvers make educated numerical guesses until

[5] Non-dimensionalization was used to deal with the problems in run time arising from the orders of magnitude difference in dimensions between the x- and y-directions.

[6] A surface phenomenon is approximated by increasing the diffusion coefficient of O_2 within the platinum volume i.e. there should be no resistance to species transport in this region.

convergence is reached. When going into the solver source code of CFDesign™ one is able to change the number of internal iterations the solver is allowed to perform before making a global guess. A number of internal iterations around a thousand seemed to help reduce run time by aiding convergence.

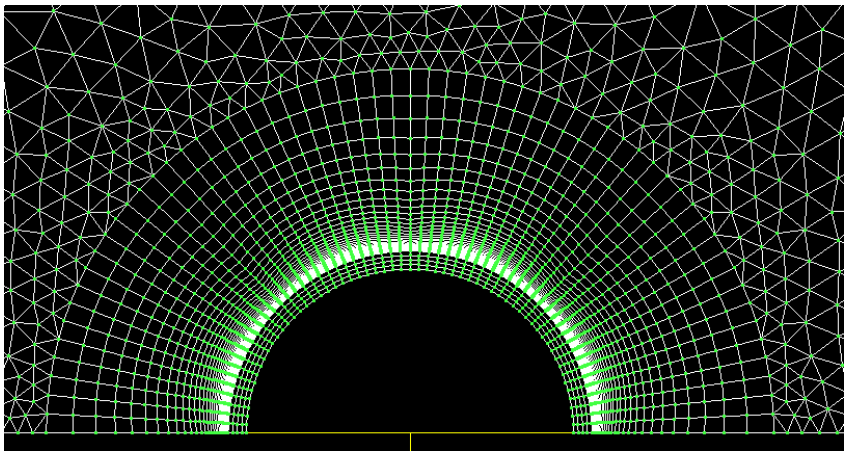

Figure 3.7: New course platinum volume meshing.

In conclusion, runtime is dependent upon many things among which is geometry. By reducing the number of nodes and having a model as close to square as possible, runtime can be greatly reduced. It was found that runtimes varied quite linearly with processor speed (a 2 Gigahertz processor is about twice as fast as a 1 Gigahertz one). The largest difference came in the type of processor used in solving the model. AMD processors are notorious for their sequential solving ability, but CFDesign™ uses a matrix based solver, which benefits greatly from the Intel architecture.

3.2 Agglomerate Model from the Literature and Current Research

The Agglomerate Model (Bultel, Ozil, and Durand [8]) is more complex than the Thin Film Model due to the consideration of multiple catalyst particles and, in some cases, a gas pore. In the Agglomerate Model, both species and charge transport are considered. The geometry of this model includes rows of platinum particles, each a set

distance apart, arranged in a hexagonal, three-dimensional network of spherical particles within the electrolyte as shown in Figure 3.1b.

3.2.1 Model Assumptions

The assumptions for the Agglomerate Model are as follow

- The Nafion (electrolyte) thickness and interparticle distance are constant.
- There is no flux across all symmetry boundaries except for the GDL/agglomerate, and agglomerate/membrane interface.
- Cylindrical symmetry is used to approximate the hexagonal symmetry.
- This process is isothermal.
- The system is at steady state.
- The electrochemical kinetic and mass transport properties are isotropic.

3.2.2 Model Equations

The equations for the Agglomerate Model consist of species and ion transport equations. In addition, the electrochemistry is modeled with a reduced form of Butler-Volmer equation, namely, the Tafel equation. This equation is active at the platinum/electrolyte interface.

3.2.2.1 Governing and Constitutive Equations

The following governing equation as utilized to model oxygen transport for the Agglomerate Model:

$$\nabla \bullet (D_{O_2} \nabla (C_{O_2})) + S_{O_2} = 0 \qquad \text{(Oxygen transport equation)} \tag{3.3}$$

Equation (3.1) tracks the diffusive transport of oxygen in the agglomerate, where D is the diffusion coefficient and C the concentration of O_2 in Nafion. This equation was also used in the Thin Film Model for species transport. The second governing equation used for charge transport is given by

$$\nabla \bullet (\kappa |\nabla \eta|) + S_{H^+} = 0 . \qquad \text{(Ohm's Law)} \tag{3.4}$$

Equation (3.3), determines the conductive transport of ions in the agglomerate, where κ is the conductance of ions in Nafion and η is the overpotential in volts. The relationship of the overpotential to the ion current density i and the oxygen concentration C is expressed by the constitutive equation.

$$i = i_o[\exp(\frac{2.3\eta}{b})]\frac{C}{C_o} \qquad \text{(Tafel Equation)} \qquad (3.5)$$

Where i_o is the exchange current density, b is the Tafel slope, and C_o the concentration of oxygen at the interface of the GDL with the agglomerate. Solutions of these three coupled equations results in current as a function of concentration with ionic resistance taken into account.

3.2.2.2 Discontinuity Condition

The model increases in complexity when pores are considered. The addition of a pore to the model means that there is a difference in concentration across the gas pore/electrolyte interface. Thus, two different boundary conditions at the GDL must be specified. One is located at the GDL/agglomerate interface and is the same as in the nonporous model. An additional boundary occurs at the GDL/pore interface and is a function of the discontinuity across the gas pore/agglomerate interface. This discontinuity is due to the fact that the oxygen solubility in Nafion is higher than the oxygen solubility in liquid water. Thus, Concentration 1 in Figure 3.8 is greater than Concentration 2 which in turn leads to the two separate boundary conditions at the GDL interface.

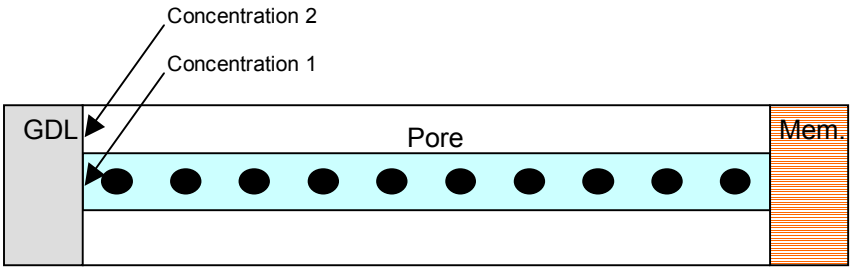

Figure 3.8: Porous Agglomerate Model geometry, displaying different boundary conditions at the GDL.

Now, in order to deal with the specific discontinuity in concentration itself across the gas pore/agglomerate interface special "effective concentration and diffusion coefficient are introduced since CFDesign™ is not able to directly handle such a jump[7] in concentration across an interface.

Both of these "effective" parameters are then introduced into the species transport equation (Equation (3.3)) which is then applied across the entire domain i.e. instead of two separate species transport equations, one for the gas pore and one for the agglomerate, a single equation is applied..

To derive this single equation, one first applies equation (3.3) to species movement in the flooded gas pore i.e.

$$\nabla D_{O_2}^{W} \nabla C_{O_2}^{W} = 0, \tag{3.6}$$

where $D_{O_2}^{W}$ is the diffusion coefficient of oxygen in liquid water and $C_{O_2}^{W}$ is the concentration of oxygen in liquid water. Next, equation (3.3) is applied to O_2 species movement in the electrolyte. The resulting species equation is

$$\nabla D_{O_2}^{P} \nabla C_{O_2}^{P} + S_{O_2} = 0. \tag{3.7}$$

The source term, S_{O_2}, is due to the platinum catalyst sites in the electrolyte. Equations (3.6) and (3.7) are the governing equations that control the transport of oxygen in both mediums.

Now, in order to take the discontinuity or jump into account, which occurs at the flooded gas pore/agglomerate interface, an effective Henry's constant is used such that

$$H^{W-P} = \frac{C_{O_2}^{W}}{C_{O_2}^{P}}. \tag{3.8}$$

Equation 3.8 is the Henry's Law at the flooded gas pore/agglomerate interface and describes the ratio of the concentration of oxygen in water to the concentration of oxygen in the polymer. The effective concentration is found by substituting the concentration of

[7] Note that such a "jump" can also be handled as described in Um, Wang, and Chen [17]

oxygen in the polymer for the concentration of oxygen in the water in equation 3.6. The result is

$$\nabla D_{eff} \nabla C_{O_2}^{P} = 0. \tag{3.9}$$

where

$$D_{eff} = D_{O_2}^{W} H^{W-P} \qquad \text{(flooded gas pore)} \tag{3.10}$$

and

$$D_{eff} = D_{O_2}^{P} \qquad \text{(polymer)} \tag{3.11}$$

This is an effective equation that can be used throughout the entire domain (i.e. polymer and flooded gas pore). Note that the new equation is a function of the concentration of oxygen in the polymer with a corrected diffusion term. Once equation (3.9) is solved for the entire domain, the concentration of O_2 in the flooded gas pore is found from the effective concentration by multiplying by Henry's constant. In this way, equiconcentration curves can be produced taking into account the discontinuity seen at the flooded gas pore/agglomerate interface.

Of course, when the gas pore is not flooded, equation (3.8) must be replaced with

$$H^{G-P} = \frac{C_{O_2}^{Air}}{C_{O_2}^{P}} \tag{3.12}$$

and equation (3.13) which is the governing equation for species transport in the gas pore i.e.

$$\nabla D_{O_2}^{Air} \nabla C_{O_2}^{Air} = 0 \tag{3.13}$$

is replaced with equation (3.9) but with

$$D_{eff} = D_{O_2}^{Air} H^{G-P} \qquad \text{(gas pore)} \tag{3.14}$$

and D_{eff} in the polymer the same as before, i.e. equation (3.11)

3.2.2.3 Non-dimensional Approach

Since convergence and time to converge of the models presented here for the geometries chosen depend very much on the scale of the parameters in play (e.g., concentration on the order of 10^{-17} mol/μm^3), steps were taken to non-dimensionalize the model by scaling each parameter by the greatest value it could possibility reach and by appropriately non-dimensionalizing each source term.

The results are

$$\nabla^* \bullet \left[D^* \left(\frac{\partial C^*}{\partial x^*} + \frac{\partial C^*}{\partial y^*} \right) \right] + \frac{S_{O_2} L^2}{D^{\max} C^{\max}} = 0 \tag{3.15}$$

$$\nabla^* \bullet \left[\kappa^* \left(\frac{\partial \eta^*}{\partial x^*} + \frac{\partial \eta^*}{\partial y^*} \right) \right] + \frac{S_{H^+} L^2}{\kappa^{\max} \eta^{\max}} = 0 . \tag{3.16}$$

where

$$D^* = \frac{D}{D^{\max}} \tag{3.17}$$

$$C^* = \frac{C}{C^{\max}} \tag{3.18}$$

$$\kappa^* = \frac{\kappa}{\kappa^{\max}} \tag{3.19}$$

$$\eta^* = \frac{\eta}{\eta^{\max}} \tag{3.20}$$

$$\nabla^* = \frac{\nabla}{L} \tag{3.21}$$

$$x^* = \frac{x}{L} \tag{3.22}$$

$$y^* = \frac{y}{L} \tag{3.23}$$

The "*" terms are effective terms ranging from 0 to 1 and "max" terms are maximum value terms. Table 3.4 gives all of the maximum value terms, some are fixed such as diffusion and conductivity, and others are allowed to vary aiding solution time. The

Table 3.4: The maximum value terms for the non-dimensionalization.

Coefficient	Maximum value
D^{max}	50000000.0 μm2/sec
C^{max}	(concentration at GDL/agglomerate interface)
κ^{max}	1.0e-4 S/μm
η^{max}	(overpotential at agglomerate/membrane interface)
L	(length of model 1μm, 10μm, or 20μm)

diffusion coefficient is set relatively high because it has to be applied to the platinum's volume discussed in Chapter 4. "L" is the maximum length for any X or Y direction in the model. The non-dimensionalization presented above results in a 30 fold increase in the speed of convergence.

3.3 Nonporous Agglomerate Model from the Literature

The Nonporous Agglomerate Model (Bultel, Ozil, and Durand [8]) is the base case for this research and assumes the electrolyte layer to be void of any pores. This layer therefore, simply contains an evenly distributed arrangement of discrete platinum particles as shown in Figure 3.9.

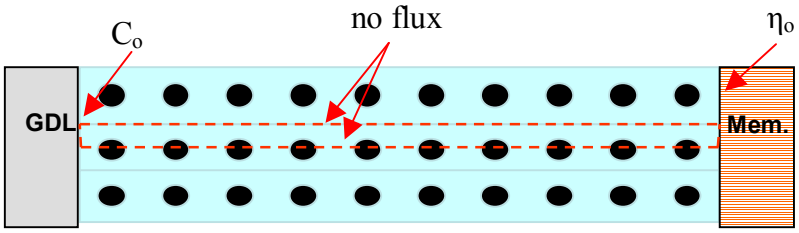

Figure 3.9: Nonporous Agglomerate Model geometry.

As with the Thin Film Model, this hexagonal symmetry is approximated with a cylindrical symmetry which allows axisymmetric equations to be applied. Thus, the geometry is simply a 2D rectangle rotated about the axis to form a 3 dimensional agglomerate.

3.3.1 Additional Assumptions

Assumptions for this model are as follows:

- There is no flux across all symmetry planes

3.3.2 Geometric Configuration

Some representative geometric parameter values for the model taken from Bultel, Ozil, and Durand [8] are given in Table 3.5. From these parameters a geometry was constructed in FeMap™ with proper dimensions. The geometry shown in Figure 3.10 is

Table 3.5: Agglomerate Model geometry.

Platinum Radius	5 nm
Nafion Cylindrical Radius	50 nm
Nafion Cylindrical Length	1000 nm
Number of Pt	10

the nonporous geometry meshed using the FeMap™ finite element meshing utility. The transition from a coarse mesh along the top wall to a fine mesh around the platinum particles can be seen by the difference in intensity.

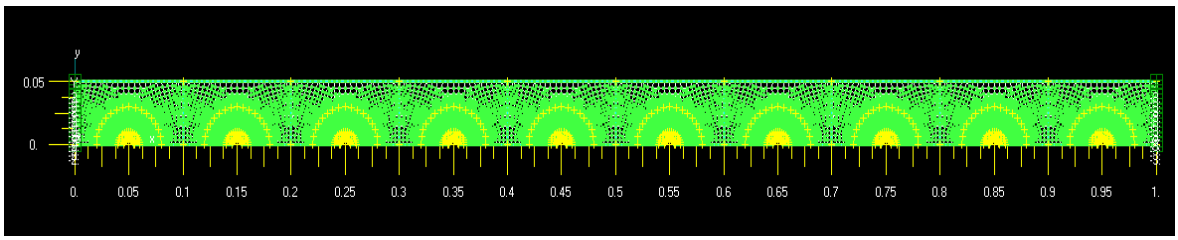

Figure 3.10: Nonporous Agglomerate Model meshed in FEMAP™.

This biased meshing is produced by refining the nodes per area when approaching the platinum particles. This procedure is used in order to acquire more detail around the platinum sites where the values of the oxygen concentration and ion current density quickly change with distance.

3.3.3 Boundary and Initial Conditions

For boundary conditions a fixed concentration is placed at the GDL/agglomerate interface. A null flux density is set at every symmetry plane. A source boundary condition (equation (3.4)) is placed at each platinum particle's surface. This source term is a reduction of the Butler-Volumer equation to the Tafel equation (equation (3.5)) and is based on concentration and overpotential. Values specified for the concentration, flux, diffusion coefficient and kinetic parameters are shown in Table 3.6.

Table 3.6: Parameters for the Nonporous Agglomerate Model.

Condition	Value	Location
$C^P_{O^2}$	2.34e-18 to 1.39e-17 mole/μm3	GDL/agglomerate interface
$D^P_{O^2}$	66.24 to 1405.05 μm2/sec	agglomerate
κ	1.42e-5 to 1.90e-5 S/μm	agglomerate
i_o	3.37e-15 to 7.19e-14 A/μm2	Pt surface
b	0.1134 to 0.1223 V/decade	Pt surface
η	0 to 1.2 V	Pt surface

The concentration boundary condition is derived from the solubility of O_2 in Nafion. The only initial condition[8] in this model is that the concentration of O_2 throughout the Nafion is equal to its solubility in Nafion. Both mass transport and kinetic data for O_2 in Nafion were taken from a paper by Zhang, Ma, and Mukerjee [16]. These parameters were found to vary with both pressure and temperature.

3.4 Porous Agglomerate Model from the Current Research

The Porous Agglomerate Model assumes the active layer to contain pores. Figure 3.11 shows an evenly distributed arrangement of discrete platinum particles surrounded by a gas pore. As with the Nonporous Agglomerate Model, the hexagonal symmetry for this model is approximated with a cylindrical symmetry which allows axisymmetric

[8] As noted earlier, initial conditions are required in order for CFDesign™ to converge to a solution.

equations to be applied.

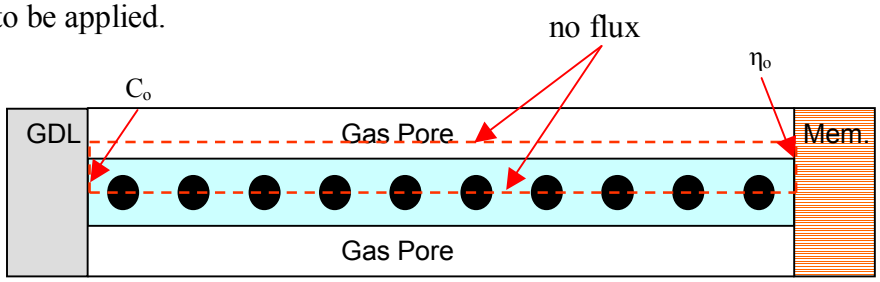

Figure 3.11: Porous Agglomerate Model geometry.

3.4.1 Additional Assumptions

Assumptions for this model are as follows:

- The pore thickness is uniform
- There is no flux across any of the symmetry planes

3.4.2 Geometric Configuration

For the base case the porosity is assumed to be 50% i.e. the pore volume is 50% of the volume of the agglomerate. This ratio is varied later on in the parametric study presented in Chapter 5. Representative geometric parameter values for the Porous Agglomerate Model are given in Table 3.7. These values are similar to those used in the Nonporous Agglomerate Model with, of course, the addition of a pore.

Table 3.7: Porous Agglomerate Model geometry.

Platinum Radius	5 nm
Nafion Cylindrical Radius	35.5 nm
Pore Cylindrical Radius	50.0 nm
Nafion Cylindrical Length	1000 nm

Using the dimensions given in Table 3.7, a mesh geometry can be created in FEMAP™ using the finite element meshing utility. The resulting mesh configuration is

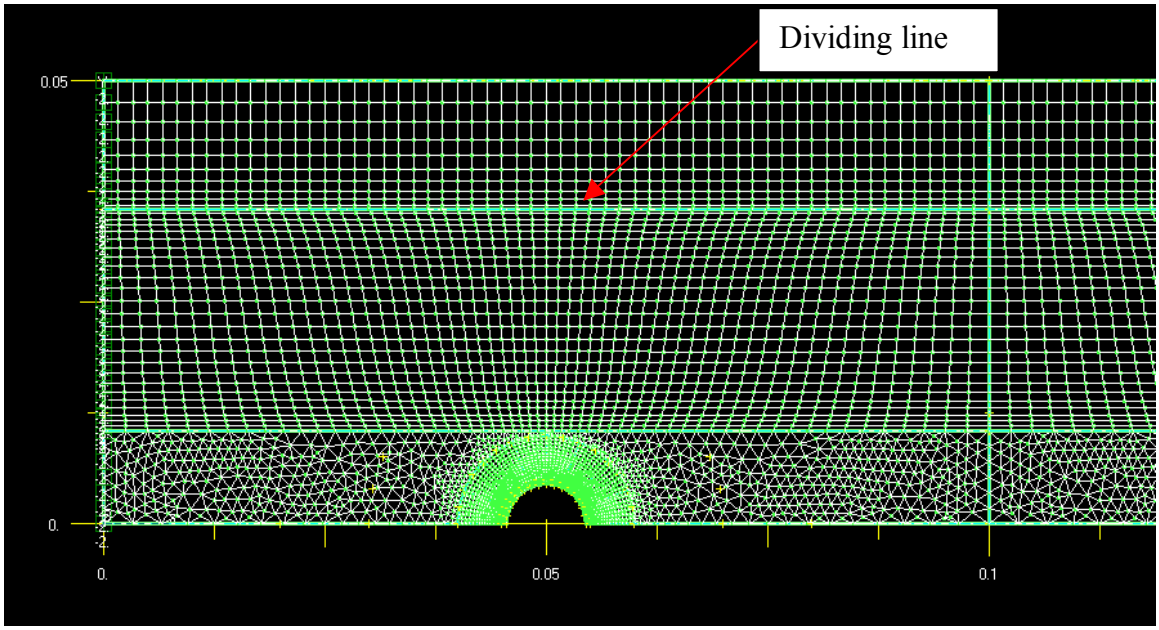

Figure 3.12: Porous Agglomerate Model geometry meshed in FEMAP™.

displayed in Figure 3.12. In this figure the dividing line that separates the gas pore from the Nafion (electrolyte) is clearly seen. The geometry is broken down into more separate pieces to enhance a uniform mesh throughout the model. The mesh varies from course in the gas pore region to more and more refined as the platinum particle site is approached.

3.4.3 Boundary and Initial Conditions

A boundary condition of fixed concentration is placed at the GDL/agglomerate interface. A null flux density is set at every symmetry plane. A source boundary condition (equation (3.5)) is placed at each platinum particle's surface. Values specified for the concentration, flux, diffusion coefficient and kinetic parameters are shown in Table 3.8

Table 3.8: Parameters for the Porous Agglomerate Model.

Condition	Value	Location
$C_{O^2}^{P}$	2.34e-18 to 1.39e-17 mole/μm^3	GDL/agglomerate interface
$D_{O^2}^{P}$	66.24 to 1405.05 μm^2/sec	agglomerate

$C_{O^2}^{Air}$	6.96e-18 to 3.87e-17 mole/μm^3	GDL/gas pore interface
$D_{O^2}^{Air}$	4.87e6 to 3.24e7 μm^2/sec	Gas pore
κ	1.42e-5 to 1.90e-5 S/μm	agglomerate
i_o	3.37e-15 to 7.19e-14 A/μm^2	Pt surface
b	0.1134 to 0.1223 V/decade	Pt surface
η	0 to 1.2 V	Pt surface

The concentration boundary conditions are derived from the solubility of O_2 in Nafion and air or just pure O_2. The initial condition[9] for this model is that the concentration of O_2 throughout the electrolyte is equal to its solubility in Nafion and the concentration of O_2 in the pore is based on the solubility of O_2 in either air or of just pure O_2. Both mass transport and kinetic data for O_2 in Nafion were taken from the paper by Zhang, Ma, and Mukerjee [16]. These parameters were found to vary with both pressure and temperature. The mass transport parameters for O_2 in air or for just pure O_2 were taken from [14] and [18].

3.4.4 Special Case

When using pure oxygen in the Porous Agglomerate Model, the model can be treated some what differently then portrayed above. This special condition assumes that there is a negligible pressure drop across the pore. If this assumption is made, the concentration is fixed down the length of the pore. Therefore, a boundary condition can be applied to the gas pore/agglomerate interface directly as shown in Figure 3.13.

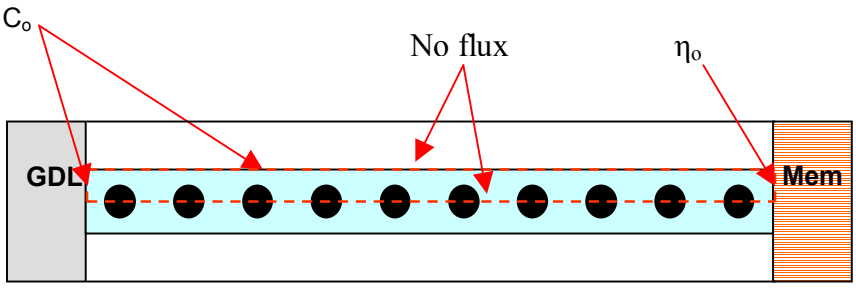

Figure 3.13: Porous Agglomerate Model geometry.

[9] As noted before, needed for converging the solution in CFDesign™.

3.5 Flooded Porous Agglomerate Model from the Current Research

The Flooded Agglomerate Model assumes the active layer to have pores which are flooded with water. Therefore, in the model there is an evenly distributed arrangement of discrete platinum particles surrounded by a flooded gas pore as shown in Figure 3.14.

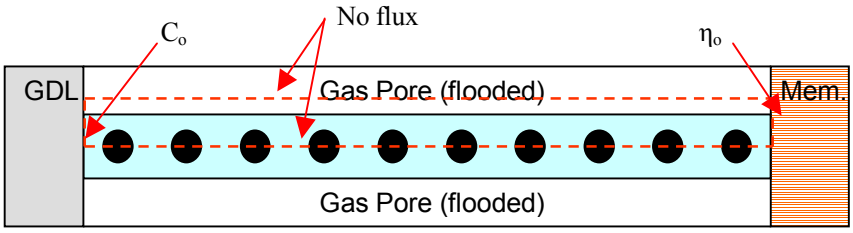

Figure 3.14: Flooded Porous Agglomerate Model geometry.

The water in the pore hinders the oxygen's ability to diffuse through the gas pore and into the agglomerate. The amount of resistance actually produced by the water can be explored in this model. Because the oxygen concentration is different in the pore then in the agglomerate, a new set of boundary conditions is required. One condition located at the GDL/agglomerate interface as before and a new one at the GDL/liquid water interface.

3.5.1 Additional Assumptions

Assumptions for this model are as follows:

- The pore thickness is uniform.
- The pore is completely flooded with liquid water.
- The liquid water is assumed fixed in place.

3.5.2 Geometric Configuration

The two dimensional geometry is constructed in FEMAP™ using the parameters in Table 3.4. From these parameters, a meshed geometry can be constructed in

FEMAP™ as shown in Figure 3.15 using the FEMAP™ finite element meshing utility. This Figure shows a clear distinction between the gas pore and the agglomerate. As in the previous models, the mesh becomes coarser as the platinum particles are approached.

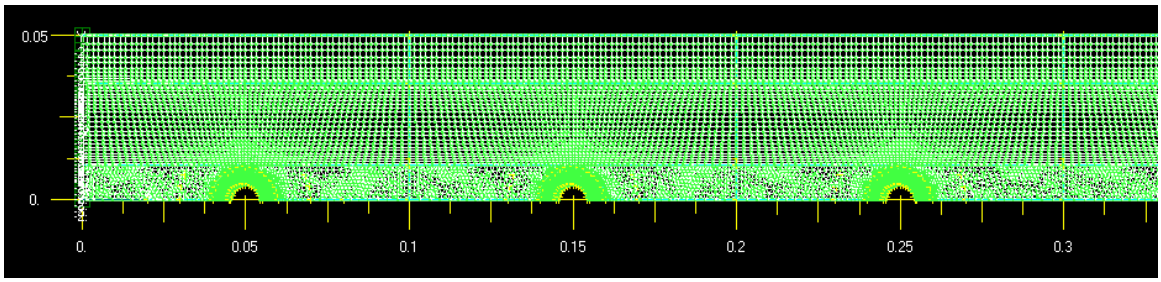

Figure 3.15: Flooded Porous Agglomerate Model geometry meshed in FEMAP™.

3.5.3 Boundary and Initial Conditions

There are three boundary conditions imposed upon the flooded model. A fixed concentration is placed at the GDL/agglomerate interface. A null flux density is set at every symmetry plane. A source boundary condition (equation (3.5)) is placed at each platinum particle's surface. Values specified for the concentration, flux, diffusion coefficient and kinetic parameters are shown in Table 3.9.

Table 3.9: Parameters for Flooded Porous Agglomerate Model.

Condition	Value	Location
$C^{P}_{O^2}$	2.34e-18 to 1.39e-17 mole/μm^3	GDL/agglomerate interface
$D^{P}_{O^2}$	66.24 to 1405.05 μm^2/sec	agglomerate
$C^{W}_{O^2}$	9.22e-20 to 4.60e-18 mole/μm^3	GDL/gas pore interface
$D^{W}_{O^2}$	3802 to 6990 μm^2/sec	gas pore
κ	1.42e-5 to 1.90e-5 S/μm	agglomerate
i_o	3.37e-15 to 7.19e-14 A/μm^2	Pt surface
b	0.1134 to 0.1223 V/decade	Pt surface
η	0 to 1.2 V	Pt surface

The concentration boundary conditions are derived from the solubility of O_2 in

Nafion and air or for just pure O_2. The initial condition[10] imposed on the model equates the concentration of O_2 throughout the Nafion to the solubility in Nafion and the concentration of O_2 in the pore to the solubility of O_2 in either air or of just pure O_2. The mass transport and kinetic parameters were gleaned from the study by Zhang, Ma, and Mukerjee [16]. All of these parameters varied with temperature and pressure.

3.6 Continuous Model from the Literature

Continuous Models are commonly seen in the literature and such a model was considered for each of the agglomerate models considered here i.e. the nonporous, porous, and flooded porous. The continuous model is presented in Figure 3.16, assumes the active layer catalyst activity to be continuous throughout the layer. This is an important model with which to compare the discrete models. By comparing a non-discrete (continuous) case to a discrete case, the validity of the common continuous assumption can be decided.

Figure 3.16: Continuous Nonporous Model geometry.

3.6.1 Geometric Configuration

The geometry for the continuous case is identical to each of the previous agglomerate models, only now there are no discrete platinum particles. Thus, the catalyst is present throughout, and the source term is applied throughout the whole active layer

[10] As noted before, needed for converging the solution in CFDesign™

except the pore. The meshed geometry for this non-discrete case is shown in Figure 3.17. This particular figure represents the nonporous case. The meshes for the porous and flooded porous cases are very similar. Due to the concentration of oxygen and ions not changing much over a particular distance, a course mesh is used to aid solution time.

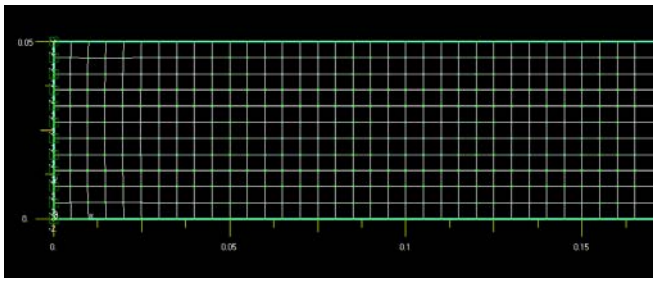

Figure 3.17: Continuous Agglomerate Model geometry meshed in FEMAP™.

3.6.2 Boundary and Initial Conditions

The boundary and initial conditions for the continuous case are exactly the same as for each of the particular discrete cases (nonporous, porous, or flooded porous). However, the source term is now applied across the entire electrolyte.

3.7 Methodology of Study

After validating the Thin Film and Nonporous Agglomerate Models produced by Bultel, Ozil, and Durand [8], the porous models developed in the present research can be evaluated at varying temperatures and pressures. The results of the validation and parametric study appear in Chapter 5.

Chapter 4: Physical Properties and Geometric Configuration

The various physical properties used in the models will be further investigated in this chapter. In addition, the agglomerate/axisymmetric assumption is presented in the geometric configuration sub-section. Finally, the volumetric source approximation for a surface flux will be explored, which becomes important due to CFDesign™'s inability to consider a concentration based surface flux.

4.1 Physical Properties

One of the major tasks of this research was to obtain the physical property values required by all the models. Two of the major parameter values needed for the model were those for the concentration and binary diffusion coefficients of oxygen in Nafion, water, and air. Experimental values for all of these exist in the literature for various conditions.

The models by Bultel, Ozil, and Durand [8] used values from Parthsarathy, Srinivasan, and Appleby [14]. However, there are large discrepancies in the values of these parameters and those found in Beattie, Basura, and Holdcroft [15] and Zang, Ma, and Mukerjee [16] as identified earlier in Chapter 2. Not only did values of the same parameters vary greatly by author, but similar studies conducted by the same author also varied.

In order to make sense of the large discrepancies, I spoke directly with for example, Dr. Mukerjee concerning his studies. He stated that the contact resistance between the active layer and the equipment used to measure the parameters was a major problem. Elaborating, he indicated that various trials on the same parameter produced different results, especially in the case of ion transport kinetics. This proved to be a major dilemma for my research, since a consistent set of parameter values as a function of temperature and pressure were required by all of the models.

Since the data obtained by Zang, Ma, and Mukerjee [16] was the most recent and complete and no other more objective criteria was available for choosing between the sources of data in the literature, it was decided to use the source for the model. Regression analyses were then used to fit the experimental data as function of both temperature and pressure. Figure 4.1 displays the binary diffusion coefficient of oxygen in Nafion as a function of temperature. A regression analysis provides the following correlation:

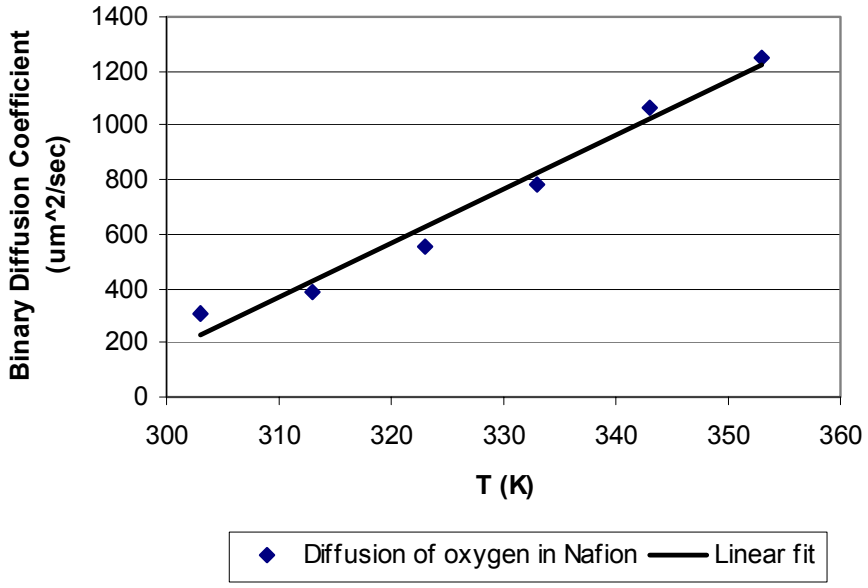

Figure 4.1: Diffusion of oxygen in Nafion 117 as a function of temperature. (Zang, Ma, and Mukerjee [16]).

The Diffusion of oxygen in Nafion 177 with varying temperature using pure oxygen at 3 atm total pressure is

$$D_{O_2}^{P}(T) = 1.99771428\ \ 57E+01 * T - 5.82850285\ \ 71E+03 \qquad (4.1)$$

Figure 4.2 shows the variance of concentration of oxygen in Nafion as a function of temperature using pure oxygen at 3 atm total pressure. This can be fit with a linear correlation given by

$$C_{O_2}^{P}(T) = -8.8057142\ 857E-20 * T + 3.79227428\ 57E-17 \qquad (4.2)$$

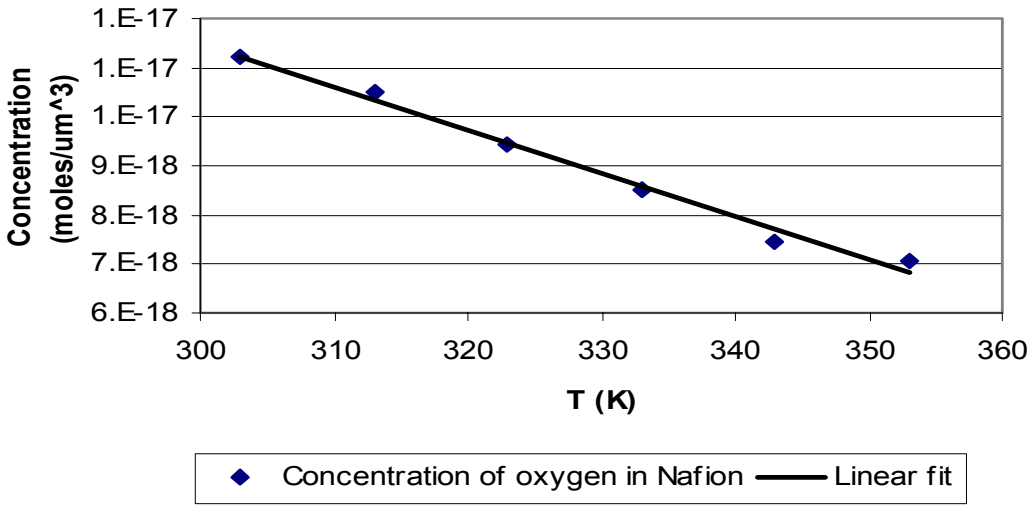

Figure 4.2: Concentration of oxygen in Nafion 117 as a function of temperature using pure oxygen at 3 atm total pressure. (Zang, Ma, and Mukerjee [16]).

Unlike the temperature effect on the diffusion and concentration of oxygen in Nafion, the effect of pressure is nonlinear. Consequently, polynomial fits are used to

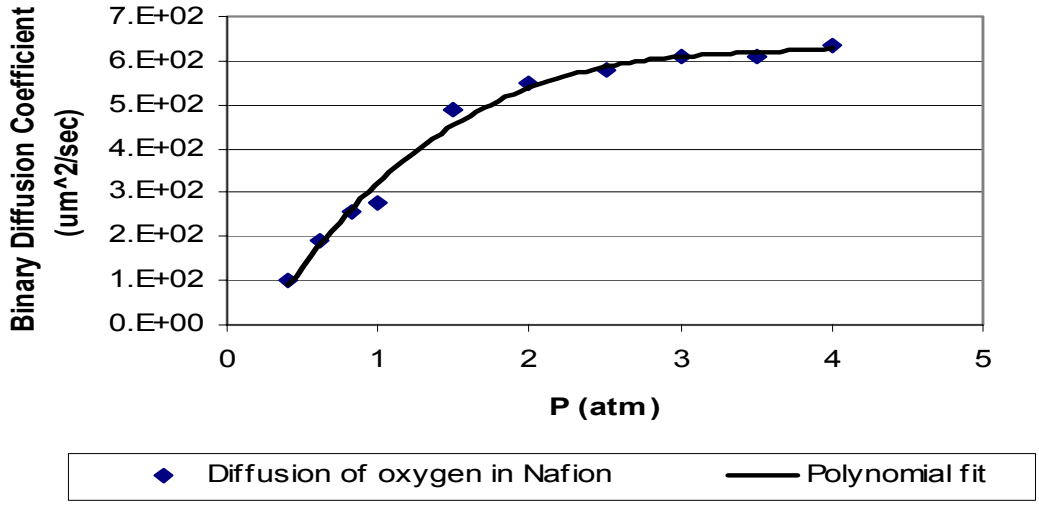

Figure 4.3: Diffusion of oxygen in Nafion as a function of pressure using pure oxygen at 323 K. (Zang, Ma, and Mukerjee [16]).

predict behavior for pressure variations. To begin with, Figure 4.3 displays experimental data for the diffusion of oxygen in Nafion as a function of pressure and a third order

polynomial fit of the experimental data provides the following correlation:

$$D_{O_2}^{P}(P) = 1.54\text{E}+01 * \text{P}^3 - 1.65\text{E}+02 * \text{P}^2 + 6.02\text{E}+02 * \text{P} - 1.31\text{E}+02 \qquad (4.3)$$

The concentration of oxygen as a function of total pressure at 323K is

$$\text{C}_{\text{O}_2}^{\text{P}} = 2.10682101990015\text{E}-18 * \text{P} + 2.70119450547330\text{E}-18 \qquad (4.4)$$

Zang, Ma, and Mukerjee [16] present parameter values at a specified pressure for multiple temperatures and vice versa, i.e. for varying pressures at a fixed temperature. Linear interpolation is used to complete the parameter tables that are needed in the model. A complete listing of the various mass transfer and electrochemical kinetic parameters are presented in Tables 4.1 to 4.6.

The initial experimental data determined by Zang, Ma, and Mukerjee [16] is presented in Table 4.1 and is consistent with equations (4.1) to (4.3). This data is used as the starting point for determining the parameter values affecting fuel cell performance that are presented in the subsequent five tables (Tables 4.2 to 4.6). The ionic conductivi-

Table 4.1: Mass transfer and electrochemical kinetic parameters for O_2 at 3 atm Zang, Ma, and Mukerjee [16].

Temp (K)	Diffusion of O_2 in Nafion (µm^2/sec)	Concentration of O_2 in Nafion (mol/µm^3)	Diffusion of O_2 in H_2O (µm^2/sec)	Concentration of O_2 in H_2O (mol/µm^3)	Tafel slope (hcd) (mV/dec)	Exchange Current Density (hcd) (A/µm^2)	Ionic Conductance (electrolyte) (S/µm)
323	624.11	9.48E-18	3869.64	2.71E-18	0.1134	1.15E-14	1.42E-05
333	823.89	8.60E-18	4714.15	2.47E-18	0.1163	1.96E-14	1.58E-05
343	1023.66	7.72E-18	5645.62	2.28E-18	0.1193	3.17E-14	1.74E-05
353	1223.43	6.84E-18	6660.98	2.10E-18	0.1223	4.78E-14	1.90E-05

*hcd – high current density

Table 4.2: Mass transfer and electrochemical kinetic parameters for pure O_2 at 1 atm.

Temp (K)	Diffusion of O_2 in Nafion (µm^2/sec)	Concentration of O_2 in Nafion (mol/µm^3)	Diffusion of O_2 in H_2O (µm^2/sec)	Concentration of O_2 in H_2O (mol/µm^3)	Tafel slope (hcd) (mV/dec)	Exchange Current Density (hcd) (A/µm^2)	Ionic Conductance (electrolyte) (S/µm)
323	324.11	5.05E-18	4018	8.28E-19	0.1134	5.74E-15	1.42E-05
333	427.85	4.58E-18	4905	7.08E-19	0.1163	9.75E-15	1.58E-05

343	531.59	4.11E-18	5894	5.85E-19	0.1193	1.58E-14	1.74E-05
353	635.34	3.64E-18	6990	4.41E-19	0.1223	2.38E-14	1.90E-05

*hcd – high current density

Table 4.3: Mass transfer and electrochemical kinetic parameters for O_2 at 5 atm.

Temp (K)	Diffusion of O_2 in Nafion (µm^2/sec)	Concentration of O_2 in Nafion (mol/µm^3)	Diffusion of O_2 in H_2O (µm^2/sec)	Concentration of O_2 in H_2O (mol/µm^3)	Tafel slope (hcd) (mV/dec)	Exchange Current Density (hcd) (A/µm^2)	Ionic Conductance (electrolyte) (S/µm)
323	716.76	1.39E-17	3802	4.60E-18	0.1134	1.73E-14	1.42E-05
333	946.19	1.26E-17	4634	4.23E-18	0.1163	2.95E-14	1.58E-05
343	1175.62	1.13E-17	5552	3.97E-18	0.1193	4.77E-14	1.74E-05
353	1405.05	1.00E-17	6553	3.76E-18	0.1223	7.19E-14	1.90E-05

*hcd – high current density

ty, which is dependent upon temperature, is gathered from a previous paper by (Ma et al [19]). The diffusion and concentration of oxygen in water as it changes with temperature and pressure is taken from [20] and [21] respectively. Dry air is assumed to have a composition of 79% N_2 and 21% O_2. These proportions change when the air is humidified.

The data presented in Tables 4.2 to 4.6 was obtained by comparing the partial pressure of oxygen in each of the above cases with the pressure data given in Zang, Ma, and Mukerjee [16]. The parameter values for the diffusion and concentration of oxygen were then evaluated using solubility data to account for the variance of the partial pressure of oxygen with the amount of water vapor present in the air or in humidified O_2 gas. This data was obtained from the previous fuel cell work by Siegel et al. [7].

In Tables 4.1 to 4.3 the partial pressure of O_2 in humidified O_2 gas changes along with the water vapor partial pressure. As the temperature of oxygen increases, so does the amount of water it can hold. Thus, as temperature increases the partial pressure of water vapor increases and the partial pressure of oxygen decreases. Table 4.7 displays the effect that water vapor has on the partial pressure of oxygen in humidified oxygen gas. At high temperatures and low pressure, the partial pressure of water can approach that of oxygen.

Table 4.4: Mass transfer and electrochemical kinetic parameters for air at 1 atm.

Temp (K)	Diffusion of O_2 in Nafion (µm^2/sec)	Concentration of O_2 in Nafion (mol/µm^3)	Diffusion of O_2 in H_2O (µm^2/sec)	Concentration of O_2 in H_2O (mol/µm^3)	Diffusion of O_2 in air (µm^2/sec)	Concentration of O_2 in air (mol/µm^3)	Tafel slope (hcd) (mV/dec)	Exchange Current Density (hcd) (A/µm^2)	Ionic Conductance (electrolyte) (S/µm)
323	66.24	3.25E-18	4144.73	1.73E-19	24927366	6.96E-18	0.1134	3.37E-15	1.42E-05
333	87.44	2.94E-18	5050.41	1.48E-19	26914304	6.17E-18	0.1163	5.73E-15	1.58E-05
343	108.64	2.64E-18	6050.11	1.22E-19	29342288	5.17E-18	0.1193	9.26E-15	1.74E-05
353	129.84	2.34E-18	7140.48	9.22E-20	32439350	3.86E-18	0.1223	1.40E-14	1.90E-05

*hcd – high current density

Table 4.5: Mass Mass transfer and electrochemical kinetic parameters for air at 3 atm.

Temp (K)	Diffusion of O_2 in Nafion (µm^2/sec)	Concentration of O_2 in Nafion (mol/µm^3)	Diffusion of O_2 in H_2O (µm^2/sec)	Concentration of O_2 in H_2O (mol/µm^3)	Diffusion of O_2 in air (µm^2/sec)	Concentration of O_2 in air (mol/µm^3)	Tafel slope (hcd) (mV/dec)	Exchange Current Density (hcd) (A/µm^2)	Ionic Conductance (electrolyte) (S/µm)
323	174.60	4.17E-18	4061.42	5.67E-19	8144811	2.28E-17	0.1134	4.58E-15	1.42E-05
333	230.49	3.78E-18	4947.91	5.16E-19	8672663	2.15E-17	0.1163	7.79E-15	1.58E-05
343	286.38	3.40E-18	5925.54	4.75E-19	9256449	2.01E-17	0.1193	1.26E-14	1.74E-05
353	342.27	3.01E-18	6990.41	4.39E-19	9919615	1.84E-17	0.1223	1.90E-14	1.90E-05

*hcd – high current density

Table 4.6: Mass transfer and electrochemical kinetic parameters for air at 5 atm.

Temp (K)	Diffusion of O_2 in Nafion (µm^2/sec)	Concentration of O_2 in Nafion (mol/µm^3)	Diffusion of O_2 in H_2O (µm^2/sec)	Concentration of O_2 in H_2O (mol/µm^3)	Diffusion of O_2 in air (µm^2/sec)	Concentration of O_2 in air (mol/µm^3)	Tafel slope (hcd) (mV/dec)	Exchange Current Density (hcd) (A/µm^2)	Ionic Conductance (electrolyte) (S/µm)
323	331.53	5.10E-18	3998.85	9.61E-19	4867144	3.87E-17	0.1134	5.80E-15	1.42E-05
333	437.65	4.62E-18	4870.90	8.85E-19	5167761	3.69E-17	0.1163	9.85E-15	1.58E-05
343	543.77	4.15E-18	5831.91	8.29E-19	5491227	3.50E-17	0.1193	1.59E-14	1.74E-05
353	649.89	3.68E-18	6877.52	7.85E-19	5845838	3.29E-17	0.1223	2.40E-14	1.90E-05

*hcd – high current density

Table 4.7: Oxygen partial pressure in humidified O_2 gas as a function of temperature and pressure at 100%RH.

Temp (K)	P_{H_2O} (kPa)	P_{O_2} (kPa) 1atm	P_{O_2} (kPa) 3atm	P_{O_2} (kPa) 5atm
303	4.25	97.08	299.73	502.38
313	7.38	93.94	296.59	499.24
323	12.35	88.98	291.63	494.28
333	19.94	81.39	284.04	486.69
343	31.19	70.14	272.79	475.44
353	47.39	53.94	256.59	459.24

For O_2 in air, nitrogen is also present, and Tables 4.8 to 4.10 show how the partial pressure of oxygen varies with temperature and pressure at a relative humidity (RH) of 100%.

Table 4.8: Oxygen partial pressure in humidified air as a function of temperature at 100% RH and 1atm.

Temp (K)	P_{H_2O} (kPa)	P_{O_2} (kPa)	P_{N_2} (kPa)
303	4.25	20.29	76.79
313	7.38	19.63	74.31
323	12.35	18.60	70.38
333	19.94	17.01	64.38
343	31.19	14.66	55.48
353	47.39	11.27	42.66

Table 4.9: Oxygen partial pressure in humidified air as a function of temperature at 100% RH and 3atm.

Temp (K)	P_{H_2O} (kPa)	P_{O_2} (kPa)	P_{N_2} (kPa)
303	4.25	62.64	237.09
313	7.38	61.99	234.60
323	12.35	60.95	230.68
333	19.94	59.36	224.67
343	31.19	57.01	215.77
353	47.39	53.63	202.96

Table 4.10: Oxygen partial pressure in humidified air as a function of temperature at 100% RH and 5atm.

Temp (K)	P_{H_2O} (kPa)	P_{O_2} (kPa)	P_{N_2} (kPa)
303	4.25	105.00	397.38
313	7.38	104.34	394.90
323	12.35	103.30	390.97
333	19.94	101.72	384.97
343	31.19	99.37	376.07
353	47.39	95.98	363.25

It is evident from Tables 4.8 to 4.10 that nitrogen has a limiting effect on the partial pressure of oxygen in air. This is due to air being 79% nitrogen, and with the addition of water vapor, the partial pressure of oxygen can be very low. Because fuel cells require oxygen as a reactant, it would seem from this data that it would be very beneficial to use humidified oxygen at a low temperature. However, this may prove to be not true when one considers the increased kinetics the fuel cell experiences at a higher temperature.

The concentration of oxygen in liquid water is displayed in Table 4.11. This data comes from a temperature and partial pressure relation given in [21]. The partial

Table 4.11: Concentration of pure oxygen in liquid water.

Temp (K)	Concentration of O_2 in H_2O (mol/µm^3)
303	1.18E-18
313	1.04E-18
323	9.43E-19
333	8.81E-19
343	8.45E-19
353	8.29E-19

pressure of oxygen in water takes into account total pressure and whether or not the O_2 diffuses into the liquid water from humidified air or O_2.

In order to calculate the binary diffusion coefficient for oxygen in liquid water, a binary diffusion equation is used. The diffusion coefficient, D_{AB}, for species A in liquid

solvent B comes from [20] is based on temperature, and given by the following relation

$$D_{AB} = \frac{7.4\times10^{-8}(\Phi_B M_B)^{1/2} T}{\mu_B V_b^{0.6}} \tag{4.5}$$

where Φ_B is the "association" parameter for solvent B, M_B the molecular weight of solvent B, T the absolute temperature of the mixture, μ_B the viscosity of the solution, and V_B the molar volume of solute at the normal boiling point.

4.2 Geometric Configuration

4.2.1 Agglomerate and Axisymmetric Assumption

The agglomerate geometry used in this model is based on the research conducted by Bultel, Ozil, and Durand [8]. It is assumed that the agglomerate is composed of electrolyte material and platinum particles which are distributed in a homogeneous fashion throughout the agglomerate. In this arrangement, once the mean particle diameters and interparticle distances are fixed as shown in Figure 4.4, the active layer geometry is fixed.

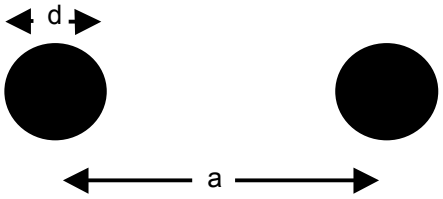

Figure 4.4: Mean particle diameter (d) and interparticle distance (a).

In this active layer the carbon which supports the Pt catalyst, is assumed simply as a source or sink for the electron present at the reaction site (the Pt surface)[11]. Furthermore,

[11] Electron conduction within the agglomerate also needs to be considered. The models developed in this research assume that a continuous conduction pathway leading from the carbon supported catalyst to the GDL exist. This assumption needs to eventually be replaced by some type of geometric modeling of this pathway since pure water which has a conductivity four orders of magnitude lower than that of carbon is not a sufficient pathway. Carbon's electrical conductivity is 1e-3 S/cm [26] and pure water is 5e-8 S/cm [27].

the distribution of particles forms a hexagonal three-dimensional network of symmetric platinum particles as shown in Figure 4.5.

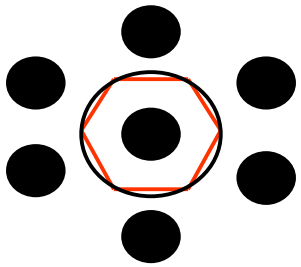

Figure 4.5: Hexagonal three-dimensional network of symmetric platinum particles.

The hexagonal symmetry surrounding each platinum particle is shown in red in Figure 4.5. If this hexagonal symmetry is approximated with cylindrical symmetry, as shown by the black circle, cylindrical agglomerates are formed. Figure 4.6 displays this cylindrical agglomerate symmetry (shown by the red lines) within an active layer. In 3D this agglomerate becomes a cylinder connecting the GDL to the membrane electrolyte as seen in Figure 4.7.

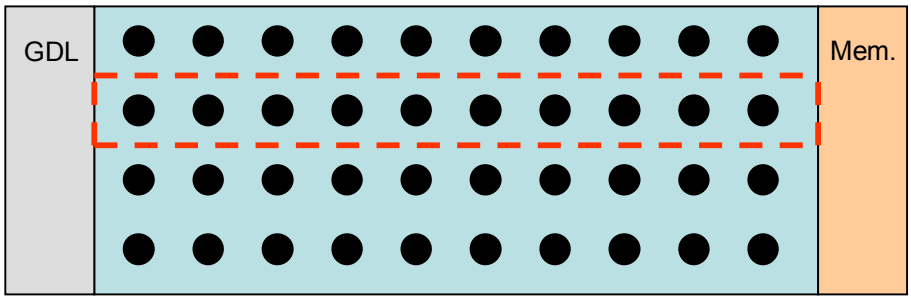

Figure 4.6: Active layer with cylindrical agglomerates.

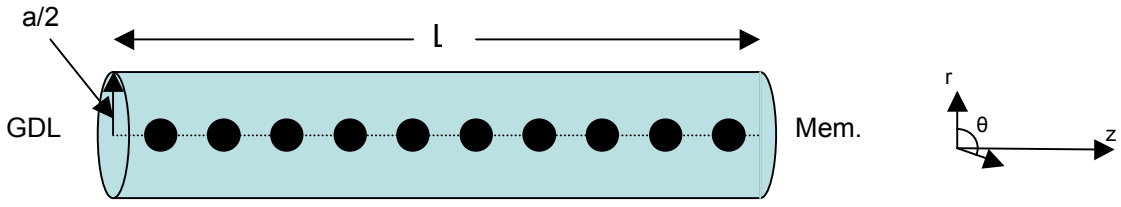

Figure 4.7: Cylindrical agglomerate geometry.

The cylinder in Figure 4.7 has a radius equal to half the interparticle spacing (a) and a length (L) equal to the thickness of the active layer. Such symmetry allows one to assume that concentration and overpotential do not change in the θ direction. Figure 4.8 shows how this assumption of cylindrical symmetry permits the 3D agglomerate to be simulated by a 2D plane. This 2D axisymmetric geometry considerably reduces the number of mesh nodes required[12] and significantly reduces model run-time in CFDesign™.

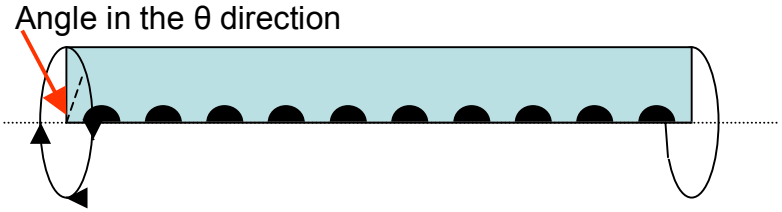

Figure 4.8: Reduction of the 3D agglomerate to a 2D plane due to the assumption of cylindrical symmetry.

4.3 Volumetric Source Approximation

A drawback to using CFDesign™ as the finite element solver is that it is unable to apply a concentration based source term as given by equation (3.5). This sink accounts for the oxygen reduction reaction taking place at the platinum surface. In order to circumvent this dilemma, the surface flux was changed to a volumetric flux condition by imposing it upon a volume and using an area per unit volume correction. This new volumetric source (i.e. current density per unit volume) is given by

$$i = r_{A/V} \cdot i_{\circ}[\exp(\frac{2.3\eta}{b})]\frac{C}{C_{\circ}} \qquad \text{(modified Tafel equation)} \qquad (4.6)$$

where

[12] Even with the axisymmetric assumption, as many as 500,000 nodes may be required to accurately solve the agglomerate models.

$$r_{A/V} = \frac{A_{Pt}}{V_{Pt}} = \frac{4\pi r_o^2}{\frac{4}{3}\pi(r_o^3 - r_i^3)} \tag{4.7}$$

is the area per unit volume correction factor and r_o is the outside radius of the particle and r_i the inside radius resulting from conversion of the surface flux into a volumetric flux. The A_{Pt} is the outer surface area of the platinum particle and V_{Pt} is the volume difference between the outer and inner hemispheres formed by the actual and adjusted Pt particle. Figure 4.9 illustrates the new geometry created.

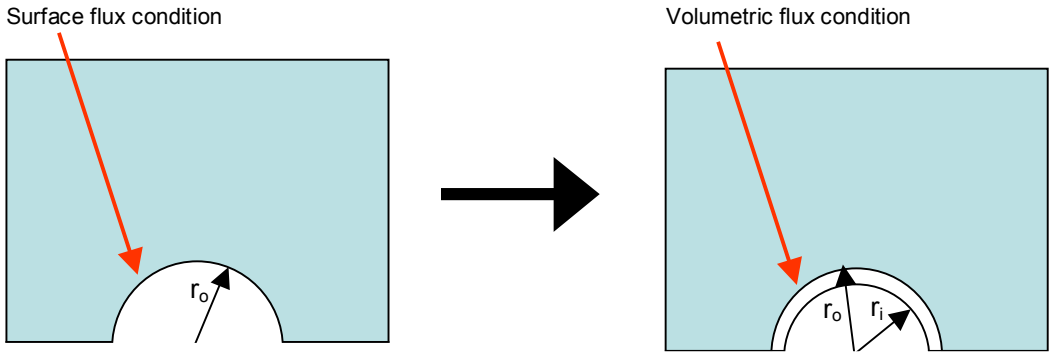

Figure 4.9: Geometry associated with the volumetric flux assumption.

Of course, r_i is a degree of freedom which must be chosen consistent with the idea that this volume difference be small enough to approximate the platinum particle's surface. However, if this volume is made too small, problems with meshing are encountered. This arises from the rapid change in concentration in the radial direction. Thus, a surface is created that satisfies both conditions and is similar to the one shown in Figure 4.9.

Chapter 5: Results and Discussion

The succeeding sections present the results for the various models described in Chapter 3 and discuss the effect on performance for a proton exchange membrane fuel cell. First, the Thin Film and Agglomerate Models are validated using published models in the literature. Next, a parametric study is presented. In this study, results for similar geometries and thermodynamic conditions were varied to find ideal platinum particle placements and geometries for the active layer. The finial section of this chapter highlights specific active layer arrangements found to be beneficial to fuel cell performance. This section also concludes with a best case scenario for the cathode active layer.

5.1 Model Validation

In order to validate the proposed models, results from the Butel, Ozil, and Durand [8] were compared to the results produced by the models formulated here. Once validated, confidence in the model was sufficiently high to perform the parametric study.

5.1.1 Thin Film Model Validation

The geometry for the validation was constructed using FEMAP™, in order to mimic the study conducted by Butel, Ozil, and Durand [8]. This was done using the interparticle distance to mean particle diameter and active layer thickness to mean particle diameter ratios described in the paper (see Table 3.2).

The model incorporates the governing equations for species transfer and rate of consumption at the surface of the catalyst as given by equations (3.1) and (3.2) in Chapter 3. Using the finite element modeling software CFDesign™, concentration and flux boundary conditions were applied to the model consistent with those listed by Butel,

Ozil, and Durand [8] and given in Table 3.1.

The concentration distribution of oxygen throughout the active layer for this model is shown in Figures 5.1 and 5.2. The non-dimensional concentration is 1 at the GDL/active layer interface and decreases to 0.853 (an actual concentration of 2.4098e-18 mol/μm^3) at the platinum particle surface. The non-dimensional concentration is given by equation (3.18) and relates the concentration at a point in the model to the concentration imposed at the GDL/active layer interface. Using equation (3.18) equiconcentration curves are calculated and evaluated as shown in Figure 5.1.

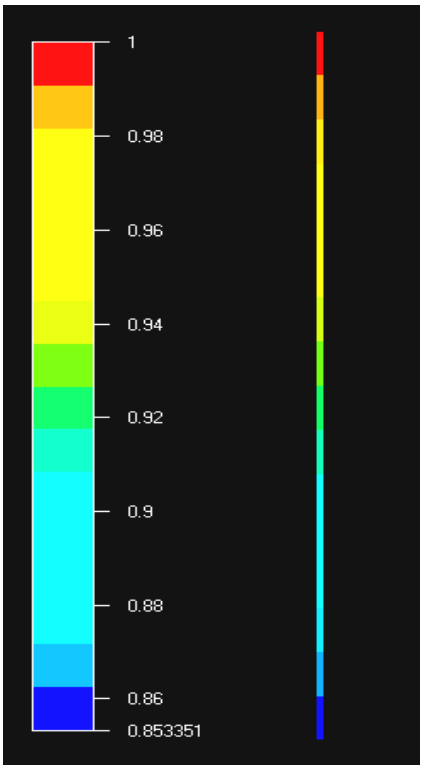

Figure 5.1: CFD equiconcentration curves for the Thin Film Model.

It is evident from the figure that the platinum particle does not influence the concentration noticeably in the active layer except in the vicinity of the particle where a local effect is seen i.e. a local drop in concentration. This local drop influences the current density of the fuel cell and, thus overall fuel cell performance.

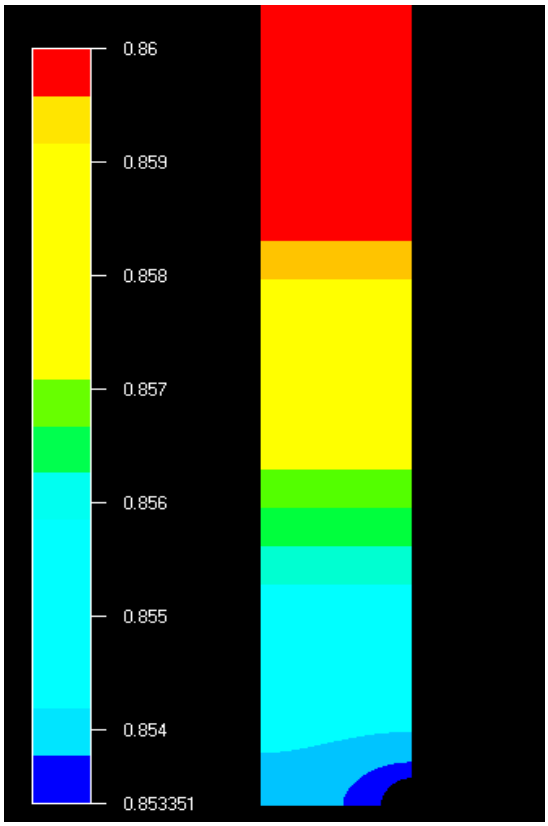

(a) Current Thin Film Model

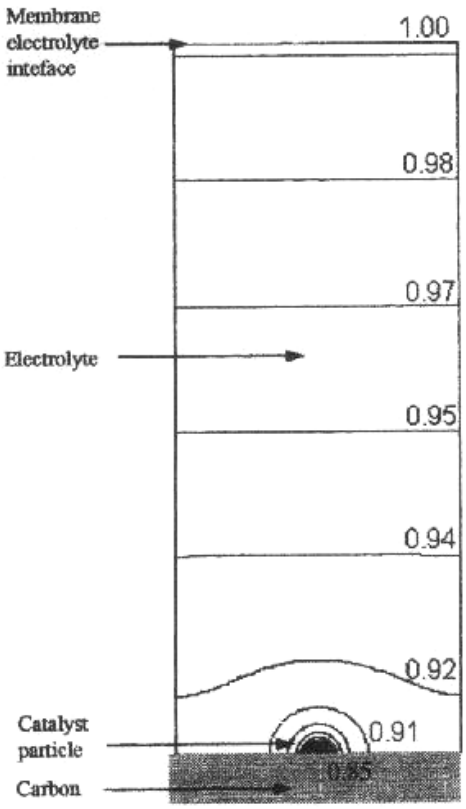

(B) Butel, Ozil, and Durand [12] Thin Film Model

Figure 5.2: CFD equiconcentration curves for the Thin Film Model.

Figure 5.2 shows that the current model reaches the same final concentration as that of Butel, Ozil, and Durand [12]. Comparison with the curves presented by Butel, Ozil, and Durand [12] shows that the model follows similar trends and is, thus, deemed validated. Note that in the Butel, Ozil, and Durand [12] model the local concentration effects are far more pronounced then in the current model. This can be attributed to that lack of knowledge of the exact conditions at which Butel, Ozil, and Durand [12] ran their studies. Furthermore, even though they reported using an active layer thickness of 1μm for their model, which is what the current model uses, the lack of a larger concentration drop through the bulk of the layer (see Figure 5.2b) seems to suggest that the thickness used by those authors was much thinner then 1 μm reported.

5.1.2 Agglomerate Model Validation

The Agglomerate Model which is more complex than the Thin Film Model, was also validated using Butel, Ozil, and Durand [12]. It represents a more realistic geometry and permits ohmic loses to be calculated due to ion transport through the electrolyte of the active layer.

For the Agglomerate Model validation, both diffusion and ohmic drop due to ion flow within the electrolyte are taken into account by coupling the governing and constitutive equations (equations (3.1), (3.2), and (3.4)). This new coupled system of equations allows one to calculate current as a function of concentration, while simultaneously account for ohmic drop through the model. Results for the concentration of oxygen distribution in the electrode/catalyst layer (active layer) appear in Figure 5.3. Concentration varies from 100% at the gas diffusion layer-electrode/catalyst interface and decreases to about 54.5% at the membrane-electrode/catalyst interface. Note that at the latter interface, a no flux condition is assumed. The bending or distortion in the equiconcentration lines in the vicinity of each platinum particle is also evident in this figure.

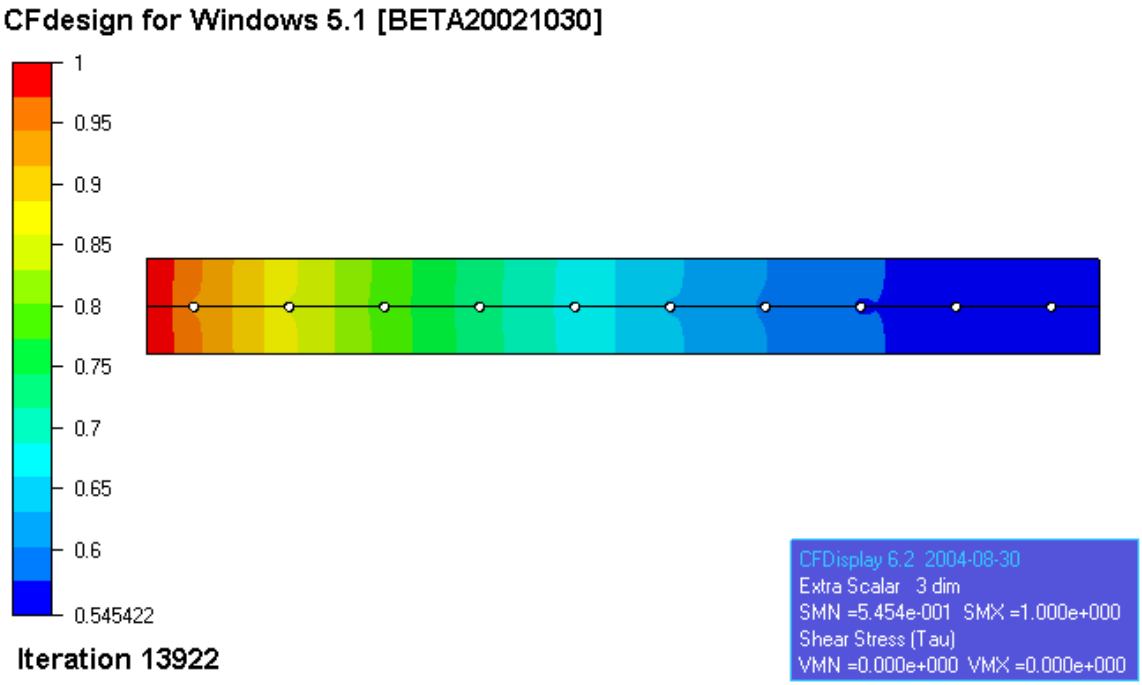

Figure 5.3: Equiconcentration curves for the Agglomerate Model.

Figure 5.4 shows the corresponding potential profile. The initial overpotential is specified at the right side of the model (the electrode/catalyst-membrane interface) and the ohmic loss due to ion flow is taken into account through the agglomerate in order to account for potential drop. Note that the left hand boundary (the GDL-electrode/catalysts interface) has a no flux condition imposed. With, the potential profile (Figure 5.4), a

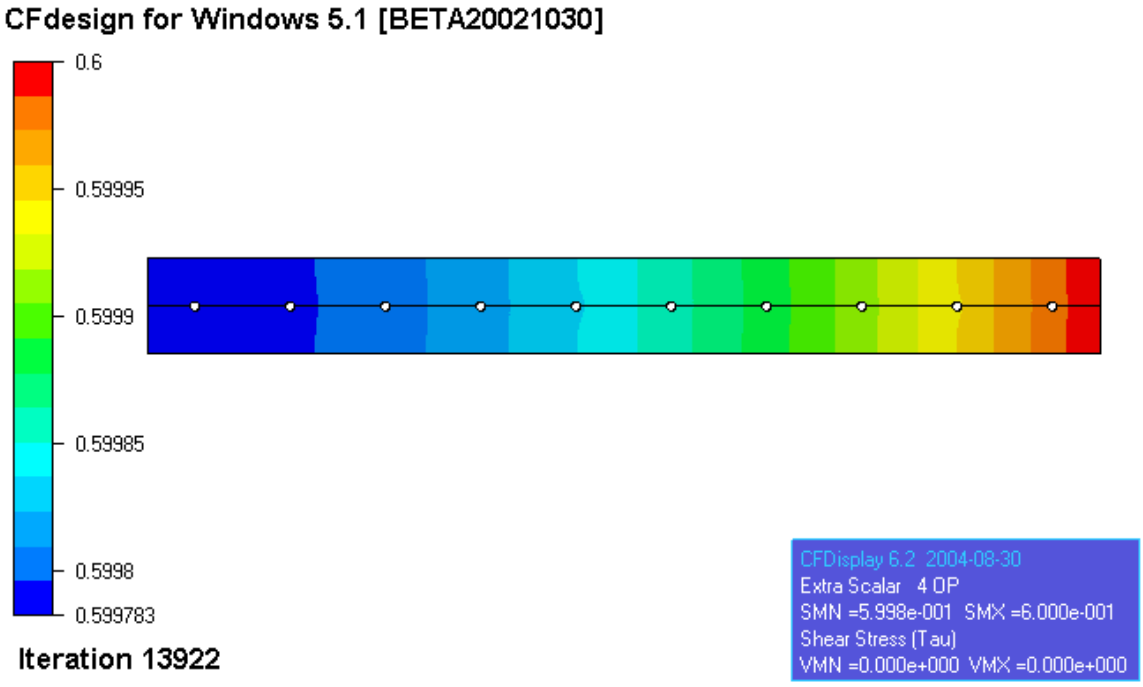

Figure 5.4: Potential profile for the Agglomerate Model.

potential drop of 2.17e-4 V is calculated. This .0362% drop across the agglomerate demonstrates the potential equation's (equation 3.4) relatively low impact under the given conditions.

In order to validate the model, a comparison was made with the concentration and potential curves found in Butel, Ozil, and Durand [8] for their Agglomerate Model. As seen in Figure 5.5 and Table 5.1, very similar results were obtained for the concentration profile. This was not the case for the potential profile. The difference in potential profile is partially attributable to not knowing the exact conditions at which the published model

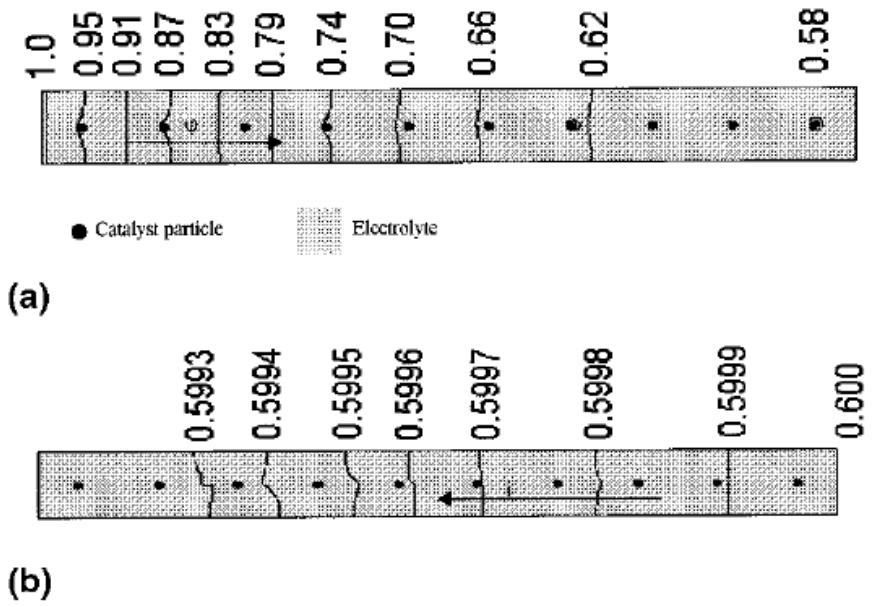

Figure 5.5: Contour plots for concentration (a) and potential (b) from Butel, Ozil, and Durand [8].

was run. Furthermore, the distortion seen in the contour lines in Figure 5.5b put into doubt the validity of the published results for potential, i.e. since the model is axisymmetric, the potential contour lines should be mirrored with respect to the platinum particles. They are not. This distortion in contour lines could be due to the very small variance in potential but is more likely due to an insufficient mesh by the authors. However, not knowing the details of their meshing, there is still a question as to whose

Table 5.1: Concentration and potential drops predicted by the current Agglomerate Model and Bultel, Ozil, and Durand [8].

	Current Model	**Bultel, Ozil, and Durand Model**
Concentration drop	45.5%	42%
Potential drop	2.17e-4 V	8e-4 V

results are correct. To check which potential profile prediction is the more realistic, an estimated potential drop was calculated using

$$D_{O_2}\left(\frac{\Delta C}{\Delta x}\right) = \frac{I_{average}}{4F} \tag{5.2}$$

and

$$\Delta V = \frac{I_{average}}{\kappa}\Delta x \tag{5.3}$$

Substituting equation (5.3) into (5.2) results in

$$\Delta V = 4D_{O_2}F(\frac{\Delta C}{\kappa}) \tag{5.4}$$

where F is Faraday's constant and κ is the ion conductivity in Nafion. This potential drop turns out to be 1.722e-4 V, which is much closer to the 2.17e-4 V drop predicted by the current model. Thus, based on this last calculation and observations made earlier, one can reasonably conclude that the current model is the correct one.

To further validate the current model's results with that of Bultel, Ozil, and Durand [8] a comparison was made using polarization curves. Using the geometric parameters found in Table 3.4 for the Nonporous Agglomerate Model and the parameters given in Table 5.2 which are taken from Parthasarathy, Srinivasan, and Appleby [14], the polarization curve (solid line) seen in Figure 5.6 was generated. After constructing the geometry the following parameters were applied to the model.

Table 5.2: Parameters for the Agglomerate Model [14].

Condition	Value
T	343 K
C_o	4.74e-18 mol/μm^3
D	394 μm^2/sec
κ	1e-7 S/m
b	.12 V
η	.6 V

Note that the parameter values taken from Parthasarathy, Srinivasan, and Appleby [14] are the ones used by Bultel, Ozil, and Durand [8] to generate the polarization curve given in Figures 5.6 by the dashed line. This slight difference in these two curves may at least partially be attributed to the fact that Bultel, Ozil, and Durand [8] never specifically state all the parameter values used to generate their curve. Instead, they give range of values from 1e-9 to 4e-9 mole/ms for the product of D and C_o.

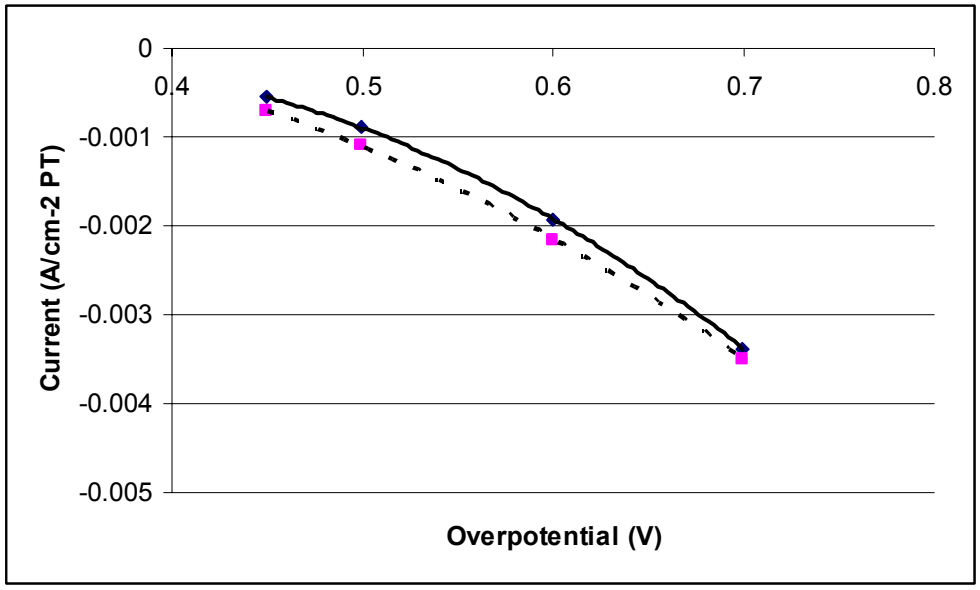

Figure 5.6: Polarization curves for cathodic oxygen reduction as predicted by the current Nonporous Agglomerate Model (solid line) and by Bultel, Ozil, and Durand (dashed line).

5.1.3 Discrete versus Nondiscrete Case

One of the biggest assumptions commonly made in the literature is that the active layer is a homogeneous mixture of carbon, catalyst, and polymer. This assumption is made due to the simplicity of not having to model the catalyst particles individually. One of the goals of my research is to find out how good an assumption this really is. Butel, Ozil, and Durand [8] concluded that the anode active layer must be modeled discretely (as opposed to nondiscretely as is done under the homogeneous assumption) in order to produce valid results. They also concluded that the cathode layer need not be modeled discretely due to their results showing that particle placement has a relatively low impact on fuel cell performance.

To validate or invalidate this last conclusion, the current Nonporous Agglomerate Model was used to see how accurately the homogeneous assumption predicts performance as compared with that for the discrete case. Two active layers were used, one with discrete active catalyst sites and one with reactions occurring throughout the volume of the layer. Thus, in the discrete case, the source terms in equation (3.3) and (3.4) are applied at the catalyst surface and in the nondiscrete case, throughout the

volume of the layer. For the nondiscrete case, a correction is applied to the agglomerate volume taking the effective catalyst area into account. The results of the comparison

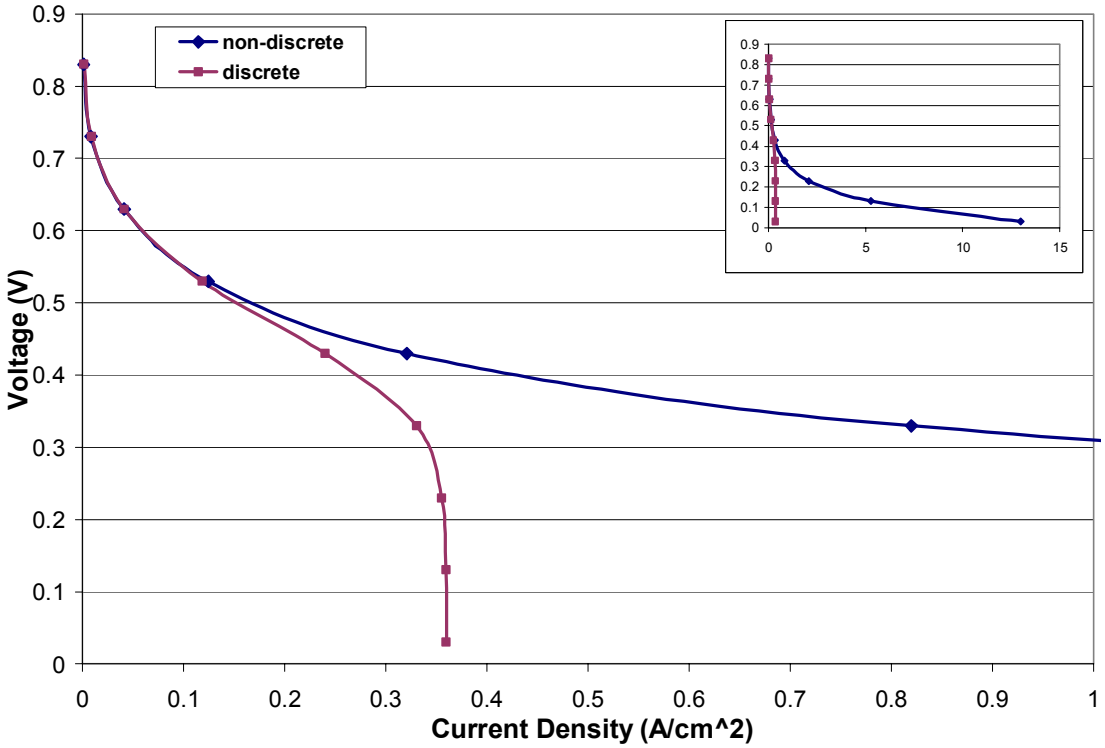

Figure 5.7: Polarization curves for the nondiscrete and discrete Nonporous Agglomerate Models at 353°K, 3atm, 10 Pt particles at a loading of 5.23e-06 μm^3/agglomerate, particle radius of 5 nm, and agglomerate length of 1 μm and radius of .05 μm.

are shown in Figure 5.7. At low current densities, the models behave identically. However, at current densities greater than about 0.13 A/cm^2, the polarization curves begin to diverge so that the nondiscrete case eventually dwarfs the discrete case. Figure 5.7 not only invalidates the conclusion of Butel, Ozil, and Durand [8] but in fact shows that discrete catalyst modeling at the cathode may be quite important, particularly at high current densities.

5.1.4 Platinum Particle Placement

Another assumption generally accepted in the literature is that current density is

simply a function of catalyst effective area for the slow oxygen reduction reaction at the cathode. This conclusion may also be premature and was, thus, tested as well. The results are given in this section.

In order to validate or invalidate this last assumption, four different porous agglomerate geometries were meshed. A geometry having 25 platinum particles is compared to a geometry having 50 smaller platinum particles. The total catalyst surface area is constant for the two cases. Next, the radius of each particle for the 50 platinum particle case is increased and compared to a 100 platinum particle case.

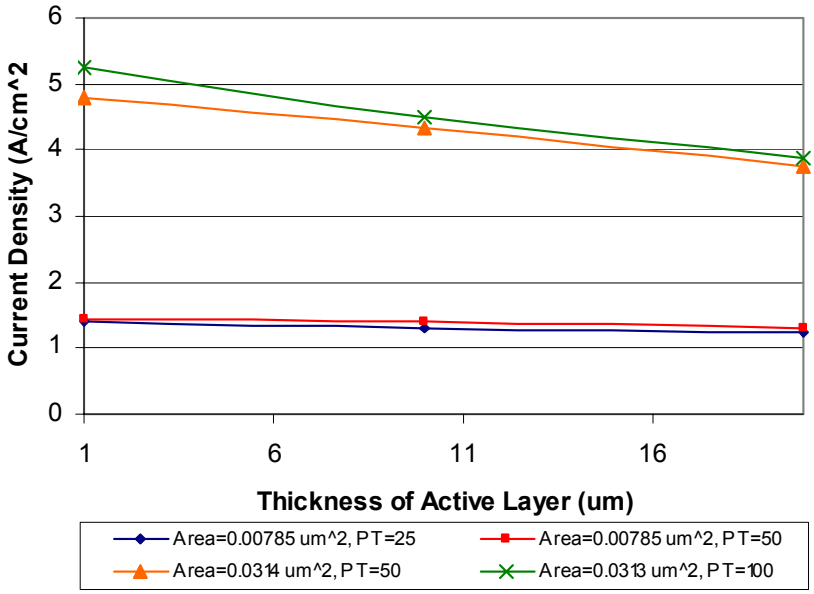

Figure 5.8: Current density versus active layer thickness for various catalyst surface areas and number of platinum particles (T=353 K, P=3atm, air, agglomerate length of 1 μm and pore outer radius of .05 μm, porosity of 50%) based on Porous Agglomerate Model.

One can see from Figure 5.8 that the agglomerate configuration with more platinum particles performs somewhat better then the one with bigger platinum particles for a fixed catalyst surface area. Conversely, the agglomerate with smaller radius platinum particles performs better then the model with less platinum particles. The result of this study proves that current density is not simply a function of catalyst area but placement and number of particles. The more particles added to a geometry, the more uniform the agglomerate is able to behave with a subsequent increase in performance.

The next thing which was looked at was whether or not the placement of a single platinum particle in an agglomerate can influence fuel cell performance. A trial was set up in order to investigate this effect for a porous and nonporous case. The geometry for each case is depicted in Figure 5.9.

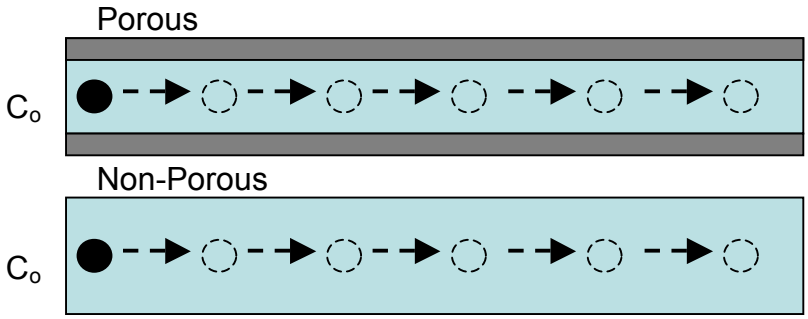

Figure 5.9: Various platinum placements down the length of a porous and nonporous agglomerate geometry (1 Pt particles at a loading of 5.23E-07 μm^3/agglomerate, particle radius of 5 nm, and agglomerate length of 1 μm and outer pore or agglomerate radius of .05 μm).

The platinum particle is initially close to the GDL/agglomerate interface and then placed progressively further away in the direction of the agglomerate/membrane interface. As can be seen in Figure 5.10 the porous agglomerate behaves completely different then the non-porous one regardless of particle placement. In the porous agglomerate species diffusion is primarily in the radial direction so that platinum placement has little effect on current density. However, the non-porous agglomerate is highly dependent on axial (x-direction) diffusion. Therefore, a change in placement of the platinum particle has a huge impact on current density. A platinum particle close to the GDL creates a higher concentration gradient over a given distance. This concentration gradient is the driving force responsible for driving more species into the model from the GDL.

Figure 5.10 also demonstrates that a platinum particle far from the GDL in a nonporous configuration will grossly under perform that of the porous case. However closer to the GDL, the effect of the pore is lessened and eventually the performance of the two agglomerates converges. This data also shows that even the porous model can benefit from moving the particle close to the GDL/agglomerate interface. In fact, the

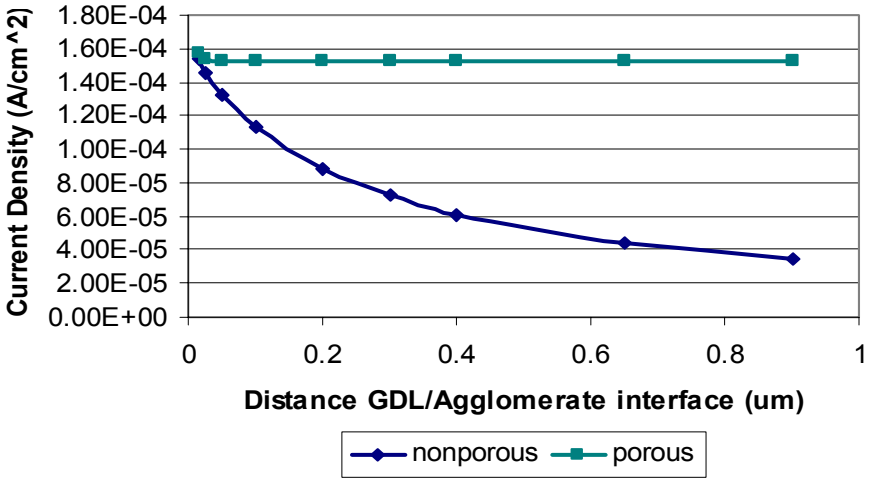

Figure 5.10: Current density as a function of platinum placement for the porous and nonporous agglomerate shown in Figure 5.9. (T=353K, P=3atm, η=0.8, 1 Pt particles at a loading of 5.23e-07 μm^3/agglomerate, particle radius of 5 nm, and agglomerate length of 1 μm and outer pore or agglomerate radius of .05 μm).

porous model would perform even better if the platinum particles were allowed to approach the gas pore.

5.2 Parametric Study

A parametric study was conducted next in order to analyze under which conditions the cathode active layer performs best. Conditions considered included variations in temperature, pressure, and geometric configuration. These variations were then used to characterize the best configuration for the cathode active layer. The main tool used in evaluating active layers were polarization curves (with losses in other fuel cell components such as the membrane neglected). Thus, the current density reported at a given overpotential is only that for the cathode active layer and is, thus, overestimated. Nonetheless, the cathode active layer curves generated are of importance for gauging overall fuel cell performance since this layer is so crucial to fuel cell operation.

5.2.1 Comparison of Different Models (porous, flooded porous, and nonporous)

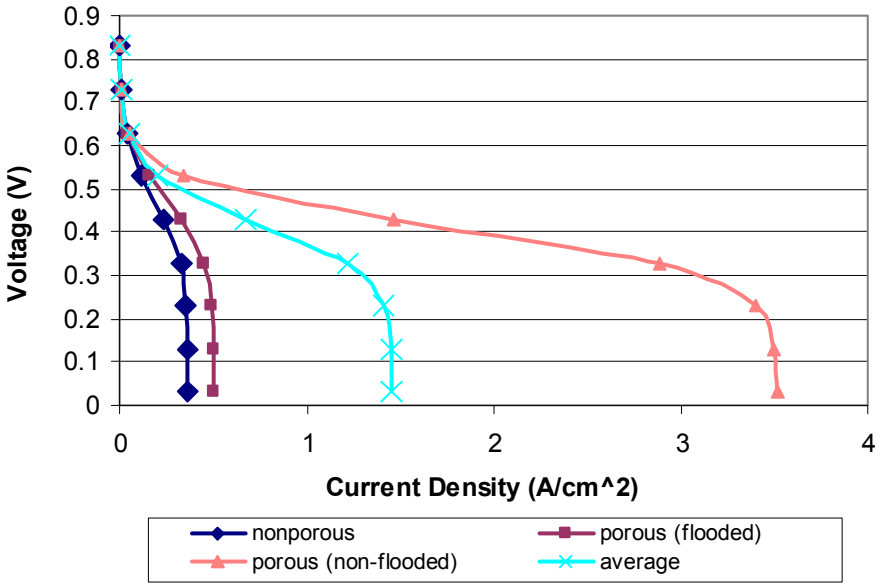

Figure 5.11: Polarization curves for a number of different agglomerate geometries (non-porous, porous, and flooded porous); T=353 K, P=3 atm, air, agglomerate length of 1 μm and pore outer radius of .05 μm, porosity of 50%, loading of 5.23e-06 μm^3/agglomerate, particle radius of 5 nm.

Figure 5.11 depicts a number of polarization cures for a catalyst loading of 5.23E-06 μm^3/agglomerate. The porous case produces substantially better results then the non-porous and flooded porous cases. This is due to the fact that the concentration of oxygen in air does not decrease down the length of the pore so that the agglomerate is supplied with significantly more species. In the non-porous agglomerate the oxygen has to diffuse through the length of the agglomerate which prohibits some platinum from receiving a high concentration of oxygen. Since current density is based on concentration this creates a diffusive bottleneck. Because the permeability of oxygen in water is only slightly better then oxygen in Nafion, the flooded porous agglomerate performs similarly to the nonporous one. This figure shows that the geometry for the agglomerate needs to be changed significantly in order to produce high current densities when considering a nonporous or flooded porous geometry. Also, in this figure is an average of the porous, flooded porous, and nonporous agglomerates since all three agglomerate types would commonly be found in a given active layer.

Figure 5.12 displays the oxygen concentration down the length of a nonporous agglomerate of length 1μm. The concentration ranges from 1 at the GDL/agglomerate interface to roughly zero at the agglomerate/membrane interface. Note that the first

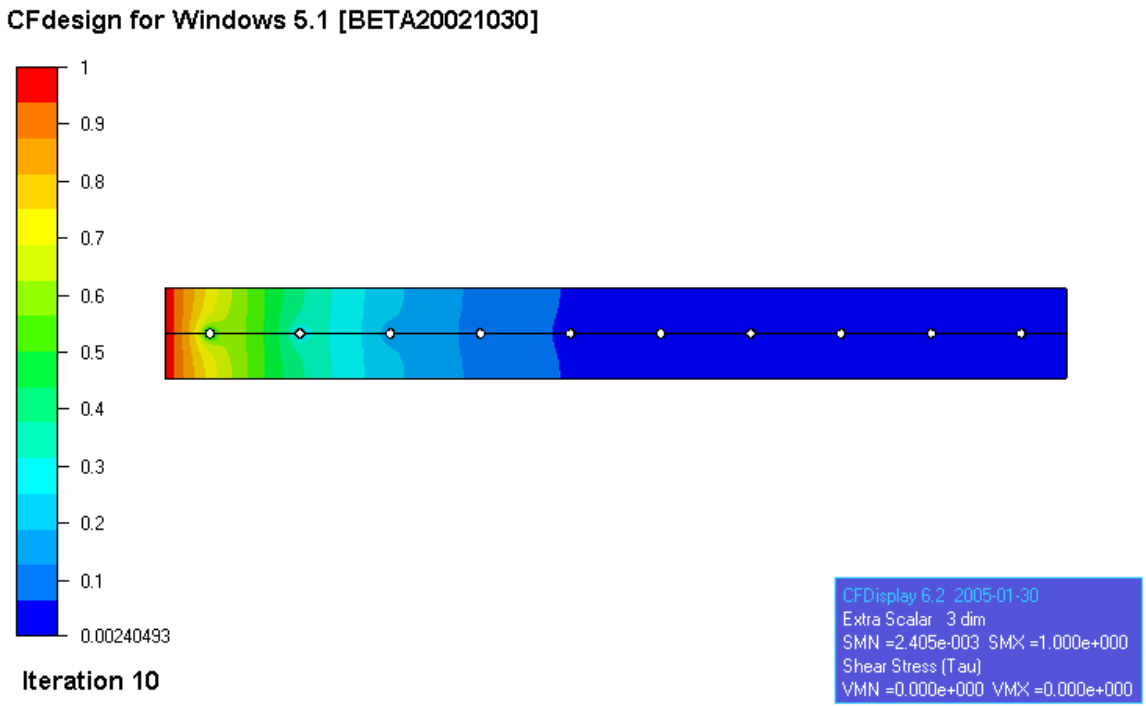

Figure 5.12: Equiconcentration curves shown for a nonporous agglomerate at T=353 K, P=3 atm, η=0.8 V, 10Pt, air, agglomerate length of 1 μm and agglomerate outer radius of .05 μm, loading of 5.23e-06 μm^3/agglomerate, particle radius of 5 nm.

platinum particle receives around 60% of the initial concentration; and results in a relatively high ion production. The last six platinum particles receive little oxygen and are thus, essentially useless at this overpotential (i.e. η=0.8 V).

The porous agglomerate is able to produce far more current then the nonporous one. This is due to the way species is delivered to the agglomerate. Notice the pores at the top and bottom in Figure 5.13. The lack of an O_2 concentration drop through these pores allows a greater amount of O_2 to be delivered to each platinum particle. In the nonporous agglomerate, the diffusion of oxygen is primarily in the x or axial direction, while in the porous agglomerate diffusion is mostly in the radial direction and, thus, the O_2 encounters less resistance since it has a shorter distance to travel through the

agglomerate. These short distances create a high concentration gradient in the radial direction which further promotes diffusion. Note that if O_2 instead of air is used as the inlet gas, the gas pore with O_2 diffusing through the air in the pore into the agglomerate reduces to a boundary condition for O_2 at the gas pore/agglomerate interface which is equal to the boundary condition of the O_2 at the inlet to the active layer.

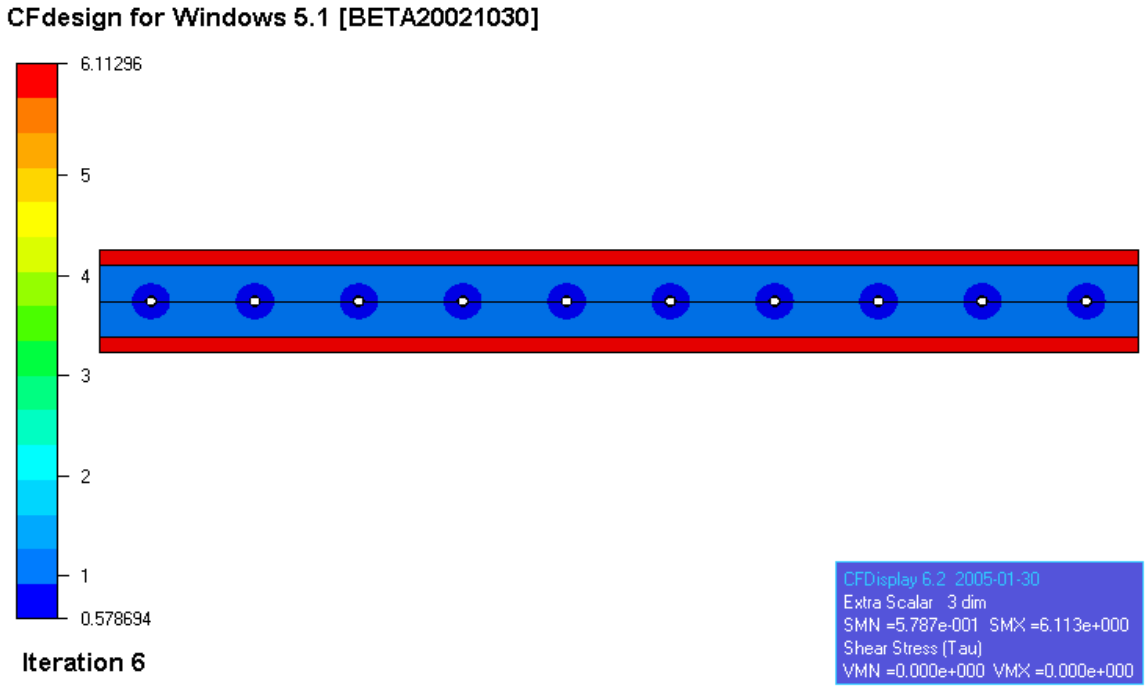

Figure 5.13: Equiconcentration curves shown for the porous agglomerate at T=353 K, P=3 atm, η=0.8 V, 10Pt, air, agglomerate length of 1 μm and pore outer radius of .05 μm, porosity = 50%, loading of 5.23e-06 μm^3/agglomerate, particle radius of 5 nm.

The Flooded Porous Model considers the gas pore to be flooded with liquid water. This has already been shown to reduce the performance of the porous active layer. This reduced effectiveness is due to oxygen's relatively low solubility and diffusivity in water. The permeability of water to O_2 is only slightly higher then for the electrolyte. Thus, a flooded porous active layer's performance mimics that of a non-porous active layer. Figure 5.14 depicts the concentration of oxygen in the agglomerate and within the gas pore. This model considers the diffusion of oxygen in liquid water and a boundary condition cannot be assumed at the gas pore/agglomerate interface due to the change in

concentration down the channel. Note that the last 3 or 4 platinum particles are relatively ineffective. Nonetheless, the flooded porous agglomerate performance is slightly better than that of the nonporous agglomerate whose last six Pt particles are relatively ineffective.

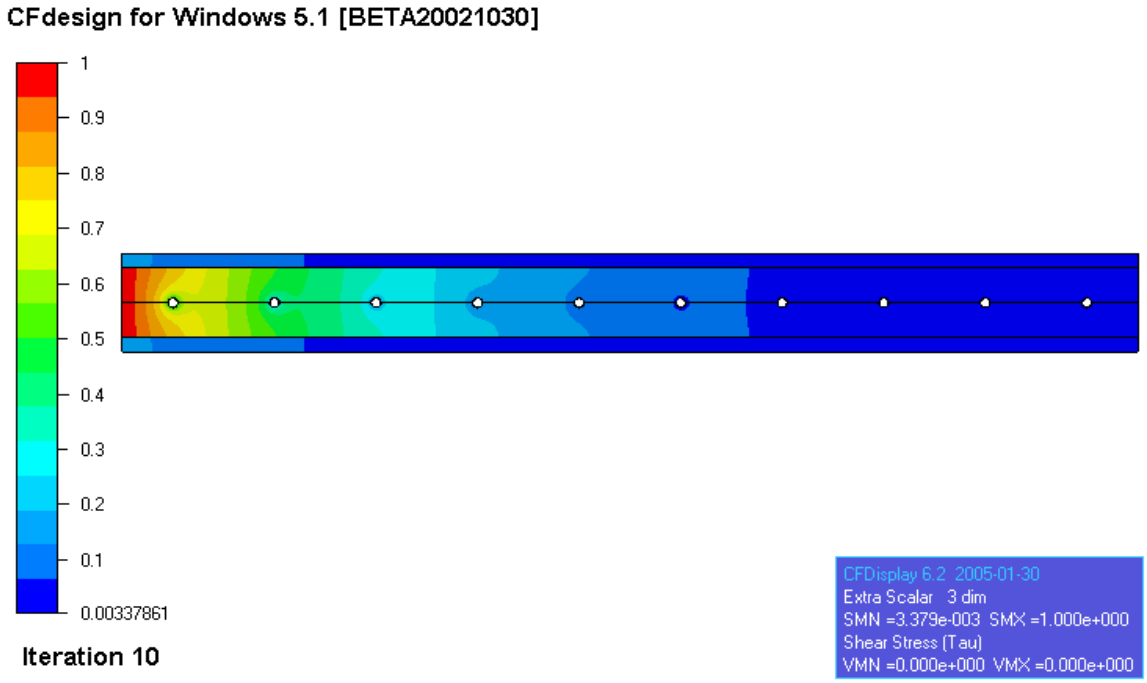

Figure 5.14: Equiconcentration curves shown for the flooded porous model at T=353 K, P=3 atm, η=0.8 V, 10Pt, air, agglomerate length of 1 μm and pore outer radius of .05 μm, porosity = 50%, loading of 5.23e-06 μm^3/agglomerate, particle radius of 5 nm.

Figure 5.14 also shows how the flooded pore starts out with an oxygen concentration well below that of oxygen in Nafion. The diffusion coefficient of oxygen in water makes up for the low concentration, producing a similar polarization curve to that for the nonporous agglomerate.

Figure 5.15, which is similar to Figure 5.11, compares the performance of all three types of agglomerates when O_2 or air are the inlet gas. The current density produced by the flooded porous and nonporous models when air is used is very low. This is due to the species not being able to get into and through the electrolyte very well. It is

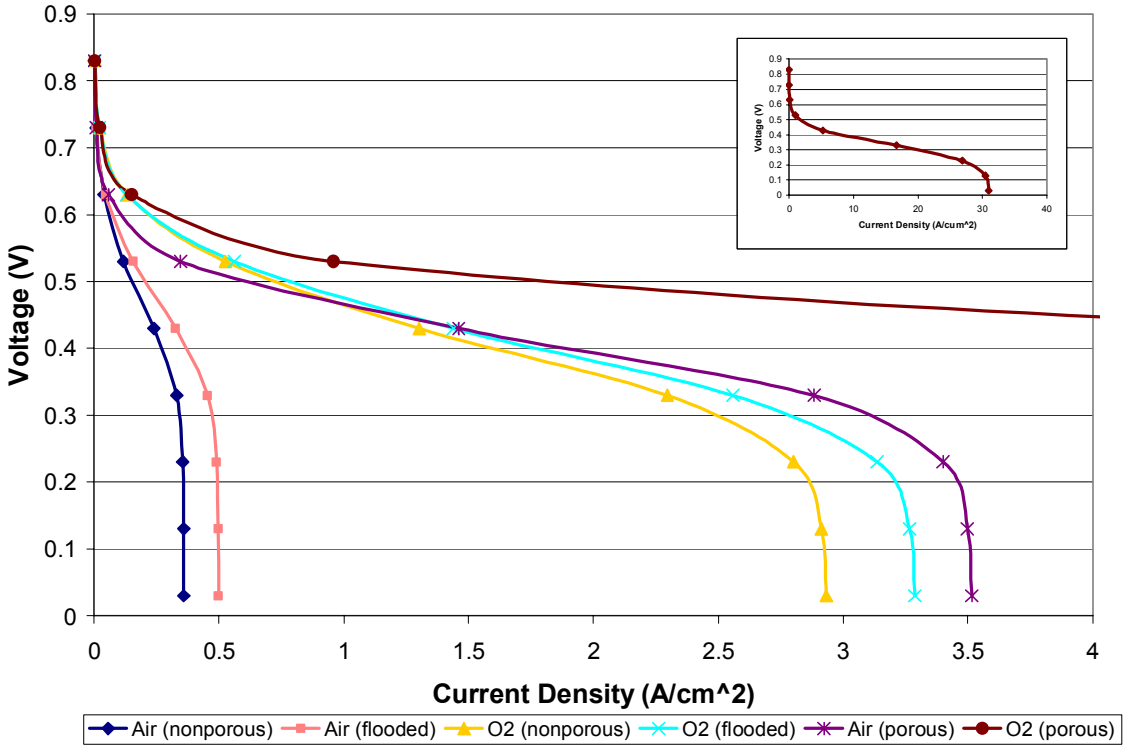

Figure 5.15: Polarization curves for the different active layer types (nonporous, porous, and flooded porous) at T=353 K, P=3 atm, η=0.73 V, 10Pt, agglomerate length of 1 μm and pore or agglomerate outer radius of .05 μm, porosity = 50% (porous and flooded) and 0% (nonporous), loading of 5.23e-06 μm^3/agglomerate, particle radius of 5 nm.

important to note that the current density for the porous agglomerate when air is used is more than that for the nonporous and flooded porous using pure oxygen. Thus, one can obtain high current densities without resorting to the use of pure oxygen. However, if the agglomerate becomes flooded the current density will reduce tremendously.

5.2.2 Thermodynamic Conditions

Varying thermodynamic conditions were evaluated next in order to find the best operating conditions for the cathode active layer. Since the temperature of a fuel cell is not typically higher then 80°C the temperature was varied from 50 °C to 80°C in 10° increments.

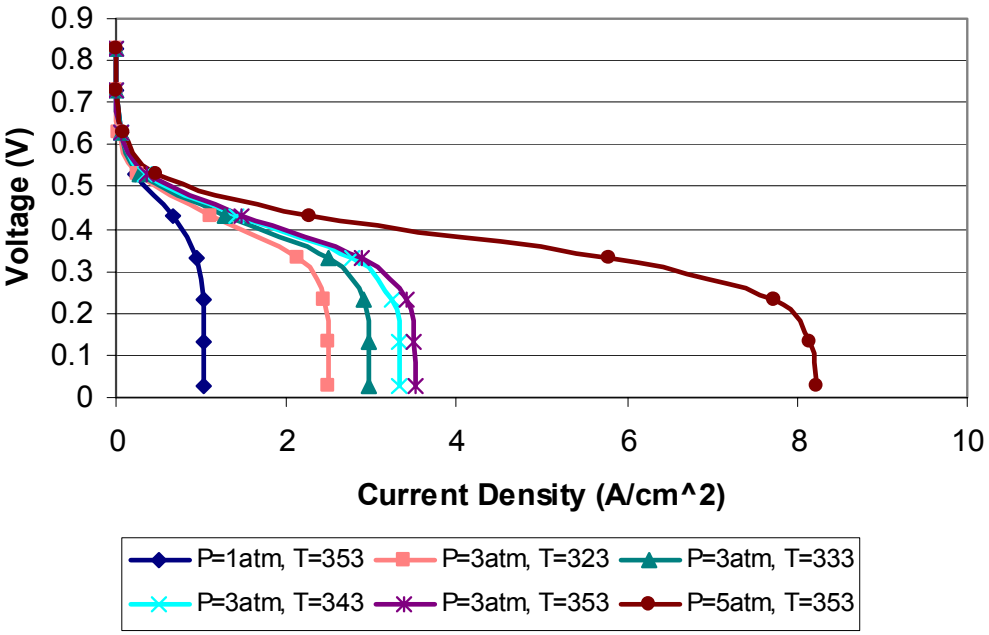

Figure 5.16: Polarization curves displaying the effects of temperature and pressure on a porous cathode active layer at η=0.73 V, 10Pt, air, agglomerate length of 1 μm and pore outer radius of .05 μm, porosity = 50%, loading of 5.23e-06 μm^3/agglomerate, particle radius of 5 nm.

As shown in Figure 5.16, a higher temperature has a positive effect on cathode active layer performance. This is due to the higher kinetics of increased ionic conductivity and improved reaction rates. This same trend is evident in each of the cases when using air or pure oxygen. A 41% increase in maximum current density is noticed when going from 323°K to 353°K.

Pressure was then varied to capture its effect on cathode active layer performance. This given pressure ignores the pressure drop seen across the gas diffusion layer. Thus, this pressure is the pressure applied to the cathode active layer directly. Figure 5.16 also displays the impact that varying pressure has on fuel cell performance.

Pressure has a tremendous impact on current density. This is due to high pressures providing higher species concentrations to the agglomerate. Figure 5.17 shows a 697% increase in maximum current density for the flooded porous case when increasing the pressure from 1 atm to 5 atm at the cathode active layer.

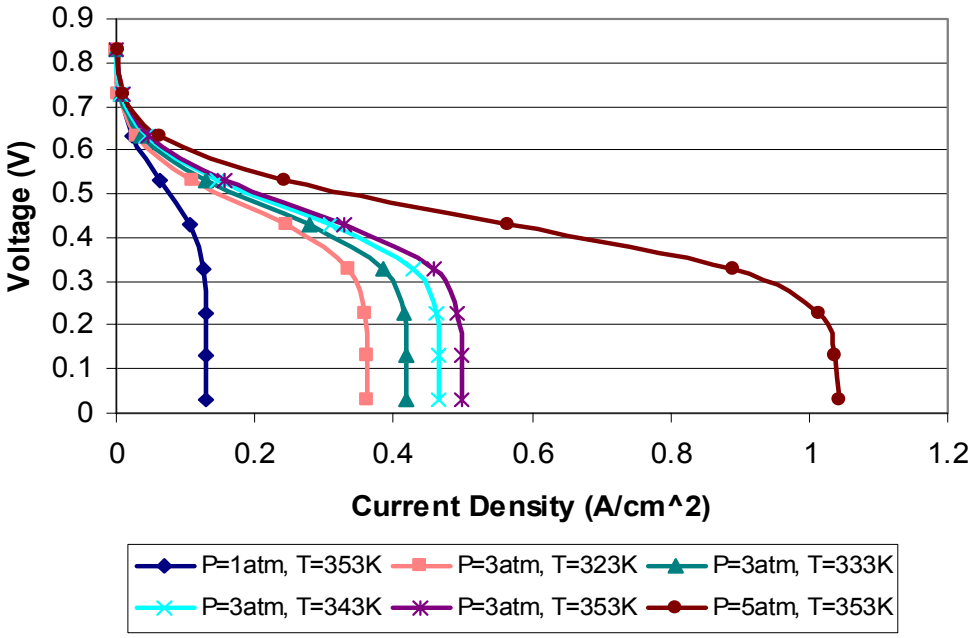

Figure 5.17: Polarization curves displaying the effects of temperature and pressure on a flooded porous cathode active layer at η=0.73 V, 10Pt, air, agglomerate length of 1 μm and pore outer radius of .05 μm, porosity = 50%, loading of 5.23e-06 μm^3/agglomerate, particle radius of 5 nm.

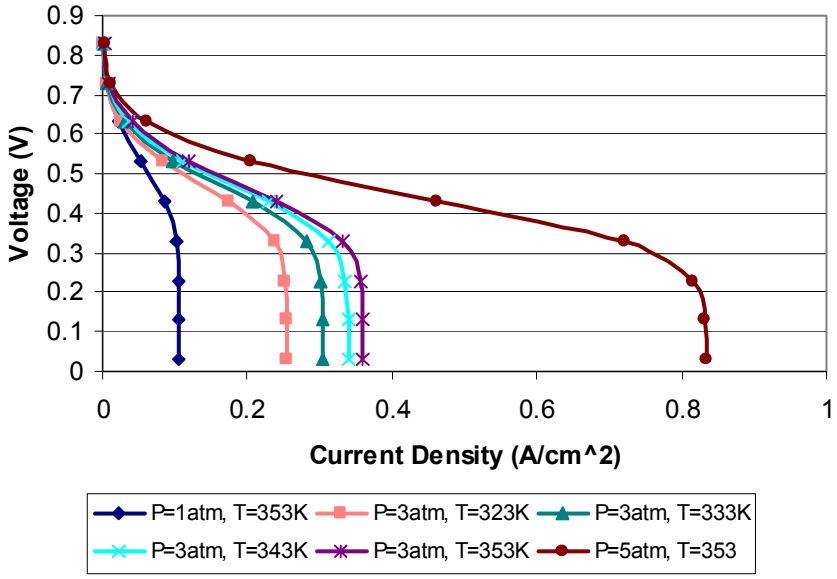

Figure 5.18: Polarization curves displaying the effects of temperature and pressure on a nonporous cathode active layer at η=0.73 V, 10Pt, air, agglomerate length of 1 μm and outer radius of .05 μm, loading of 5.23e-06 μm^3/agglomerate, particle radius of 5 nm.

The flooded porous case of Figure 5.17 shows a small performance advantage over that for the non-porous case presented in Figure 5.18. Figures 5.17 to 5.19 all follow the same trend, with high temperature and pressure very beneficial to fuel cell performance.

A comparison of Figures 5.16 and 5.18 show a difference in performance of a factor of ten. Thus, one realizes a 10-fold decrease in performance when the active layer is non-porous or porous and completely flooded.

5.2.3 Loading

A study was conducted next to find out what impact catalyst loading has on fuel cell performance. In this study, the agglomerate's length was increased from 1 µm to 10 µm to 20 µm. Figure 5.19 shows the effect this geometric parameter has on current

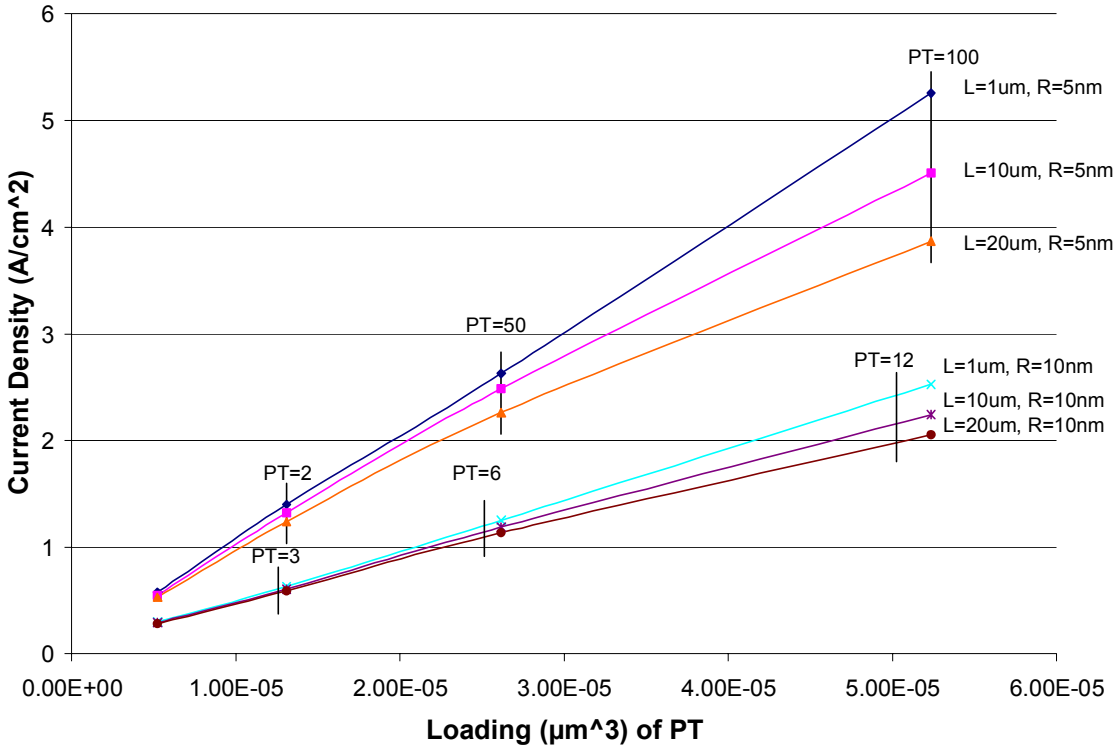

Figure 5.19: Current density as a function of loading and agglomerate length for a porous cathode active layer at η=0.73 V, air, agglomerate pore outer radius of .05 µm, porosity = 50%.

density at various loadings. Overpotential is fixed at 0.73 volts, pressure at 3 atm, and temperature at 353 K. The porous air case is used for this study. Note the major improvement when moving from 20 nm diameter particles to 10 nm ones. This is due to a smaller particle having an increase in surface area per unit volume.

Figure 5.19 also shows the effect that changes in the number and size of the platinum particles have on current density for different active layer thicknesses. The performance of the cathode is increased when using a thin active layer. This thin layer aids in diffusion of species and ions throughout the active layer, thus, producing higher current densities.

5.2.4 Porosity

Another important geometric parameter to consider is porosity. Porosity is defined as the ratio of pore volume to total volume. Thus 25% porosity means that 25% of the active layer is gas pore and 75% is agglomerate. As porosity increases, oxygen species within the gas pores is allowed to get closer to the platinum reaction sites. This

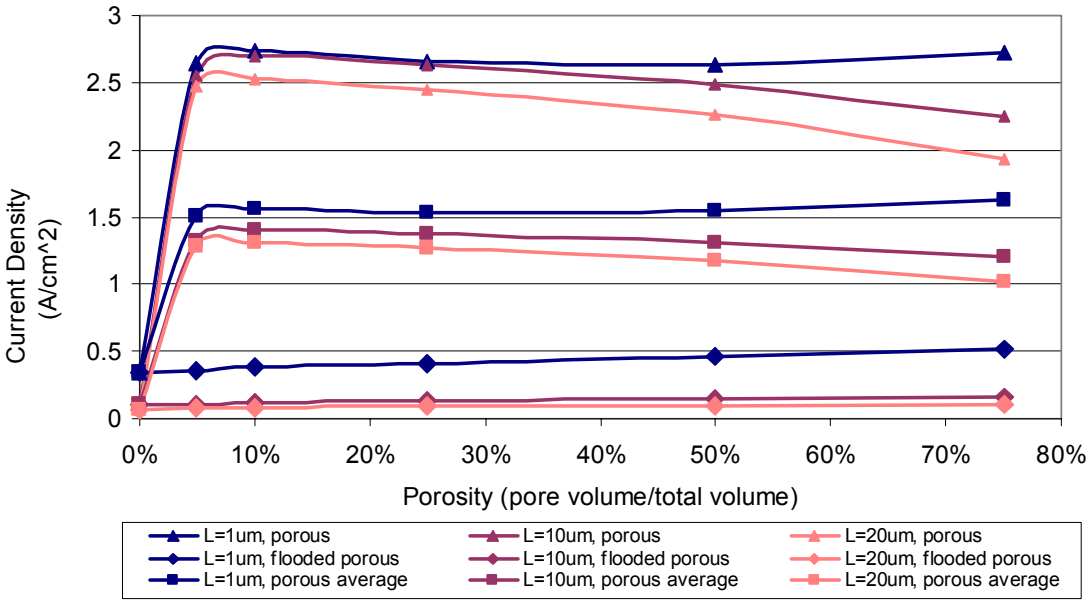

Figure 5.20: Current density as a function of porosity and agglomerate length for porous, flooded porous, and average cases at η=0.73 V, 50Pt, air, pore outer radius of .05 μm, loading of 2.62e-05 μm^3/agglomerate, particle radius of 5 nm.

aids the reaction by providing a larger concentration of oxygen at the catalyst surface. The downside is that the electrolyte is reduced as porosity increases. This causes ohmic loses to increase and is important in thick active layers.

Another thing to consider is the possibility of flooding. This being a known problem for fuel cells, another set of curves is displayed in Figure 5.20 in order to determine flooding overall effect. For this study both the porous and flooded porous cases are shown. An average of the two simulates an active layer in which half the pores are flooded and half are filled with air and is shown by the three "average curves".

For the active layer having a thickness of 1μm, there seems to be a porosity at which the trade off between resistance to ion flow versus resistance to O_2 flow reverses for the average and porous cases, i.e. below this porosity resistance to ion flow decreases while that for O_2 flow increases with a net increase in performance while above this porosity resistance to ion flow increases while that for O_2 flow decreases again with a net increase in performance. Thus, at a low porosity, the ohmic losses within the electrolyte are almost negated. In contrast, as the porosity increases more O_2 species can reach the catalyst surface, thus promoting current. The pivotal porosity for the 1μm active layer is at about 50% where any lower (down to a minimum of 5%) and there is a greater performance due to low ohmic losses and any higher and there is a greater performance due to increased concentration at the platinum surface. Below 5%, performance drops off rapidly for all the active layers lengths as pore height thickness reduces to zero. Furthermore, the longer active layer lengths do not see the same trade-off porosity point that is seen with the 1μm case. In general it would appear that for these longer lengths a porosity of between 5% and 10% leads to the best performance.

Finally, note in Figure 5.20 that for the average porous case performance is shifted down significantly. This is due to the reduced current density when half of the pores are flooded. Another notable characteristic is that the curves have changed slope slightly. This is due to thick active layers performing very poorly in the flooded porous case. Where a high porosity hinders the porous case, it aids the flooded porous case due to oxygen having a higher diffusion coefficient in water then in Nafion. Because the current density is so small in the flooded porous case, ohmic losses are never really a problem. This data reinforces how important a thin active layer is to overall fuel cell

performance. Furthermore, flooding should be reduced and eliminated as much as possible.

5.2.5 Ohmic Losses

The overpotential is explored through the agglomerate of the porous case in the following section. Figure 5.21 demonstrates the relatively small impact that ion transport has on the over all model. The overpotential only drops slightly due to the short distance the ions have to diffuse. In this case, the ion transport equation could simply be ignored.

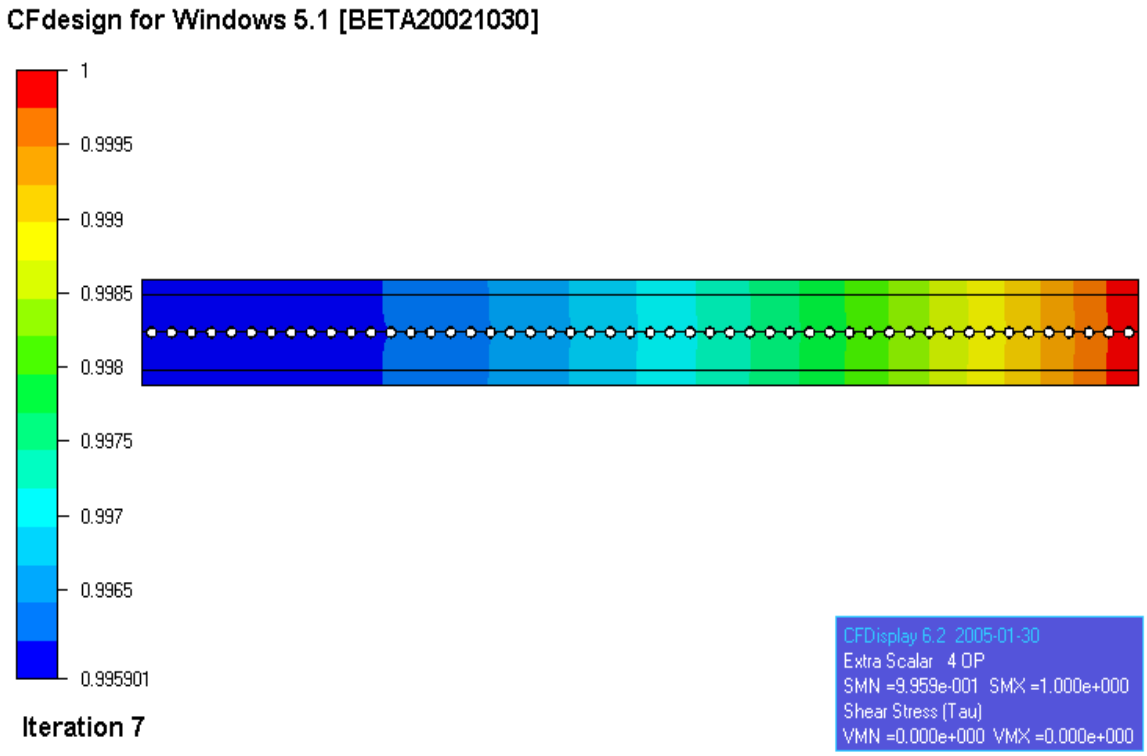

Figure 5.21: Overpotential distribution across a porous active layer at T=353 K, P=3 atm, η=0.8 V at the membrane boundary, 50Pt, air, agglomerate length of 1 μm and pore outer radius of .05 μm, porosity = 50%, loading of 2.62e-05 μm^3/agglomerate, particle radius of 5 nm.

In contrast, with the thicker active layers shown in Figure 5.22 and 5.23, the overpotential equation must be considered due to its notable effect on fuel cell performance. When the active layer is greater then 1 μm and current density is high, the

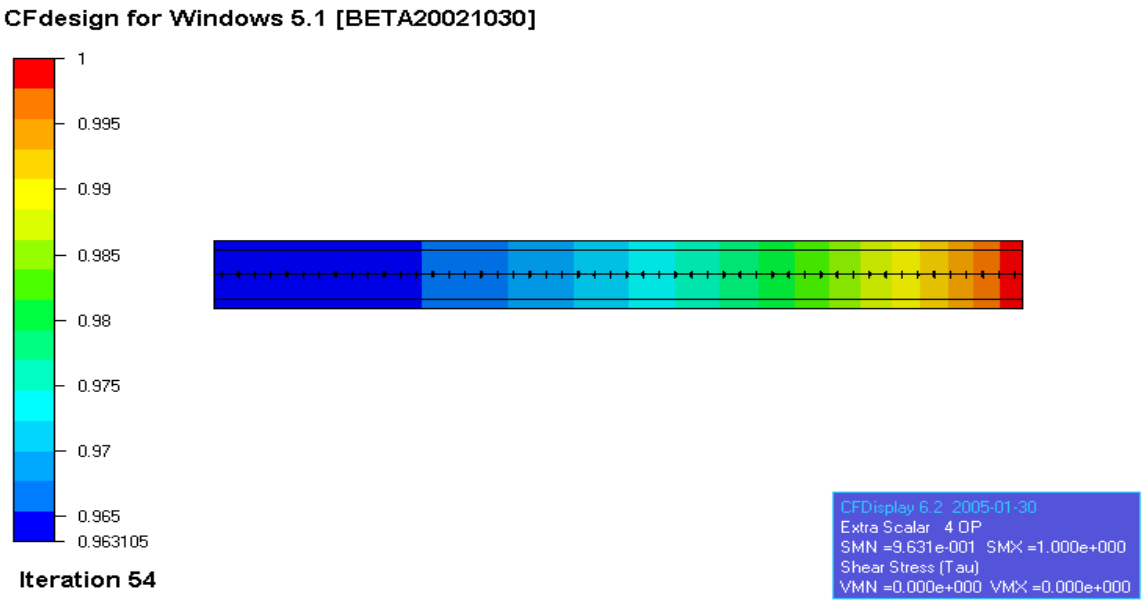

Figure 5.22: Overpotential distribution across a porous active layer at T=353 K, P=3 atm, η=0.8 V at the membrane boundary, 50Pt, air, agglomerate length of 10 µm and pore outer radius of .05 µm, porosity = 50%, loading of 2.62e-05 μm^3/agglomerate, particle radius of 5 nm (image is not to scale in the x-direction for display purposes).

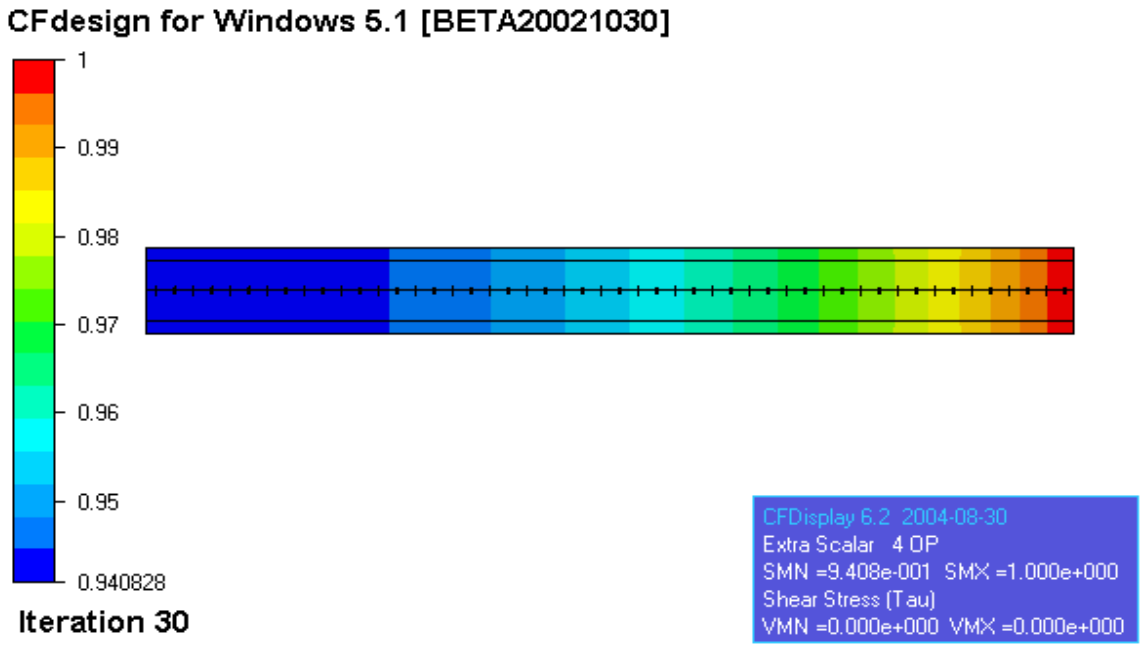

Figure 5.23: Overpotential distribution across a porous active layer at T=353 K, P=3 atm, η=0.8 V at the membrane boundary, 50Pt, air, agglomerate length of 20 µm and pore outer radius of .05 µm, porosity = 50%, loading of 2.62e-05 μm^3/agglomerate, particle radius of 5 nm (image is not to scale in the x-direction for display purposes).

effect of ion transport on fuel cell performance is no longer negligible. Figure 5.23 displays an active layer that is 20 μm in thickness. This thickness is common place in fuel cells today. Although smaller thicknesses are beneficial, technology has limited how thin the layers can be constructed.

Shown in Figure 5.23 and Table 5.3 is a 5.92% drop in overpotential across the 20 μm active layer. This is very important to consider when accurately modeling a fuel cell. Table 5.4 furthermore shows how ion transfer ohmic losses are a factor of active layer thickness. It is evident that for a thinner active layer these losses can be ignored since they are an order of magnitude smaller then for the longer active layers.

Table 5.3: Overpotential drop across active layer for various thicknesses.

Model Length	Overpotential Drop	Percentage Drop
1 μm	0.003279 V	0.4099 %
10 μm	0.029516 V	3.6895 %
20 μm	0.047338 V	5.9172 %

5.2.6 Biasing

With results (see Figure Figure 5.10 in section 5.1.4) showing improvements when the platinum particles approach the active layer/GDL interface, a final study, was made that looked at biasing the platinum particles towards this interface. Figure 5.24 displays this biasing and its effect on the O_2 concentration profile in an active layer of length 1μm for the nonporous case.

Note how the concentration profiles surround each agglomerate particle. The first four particles have a concentration profile distribution around their entire group. The O_2 concentrations become very small as the active layer/membrane interface is approached.

Results form this new biased model are compared to previous results obtained from the uniformly loaded active layer, namely, Figure 5.12. Note how in this last figure it is the last six particles (instead of the last four as in Figure 5.24) which are not supplied

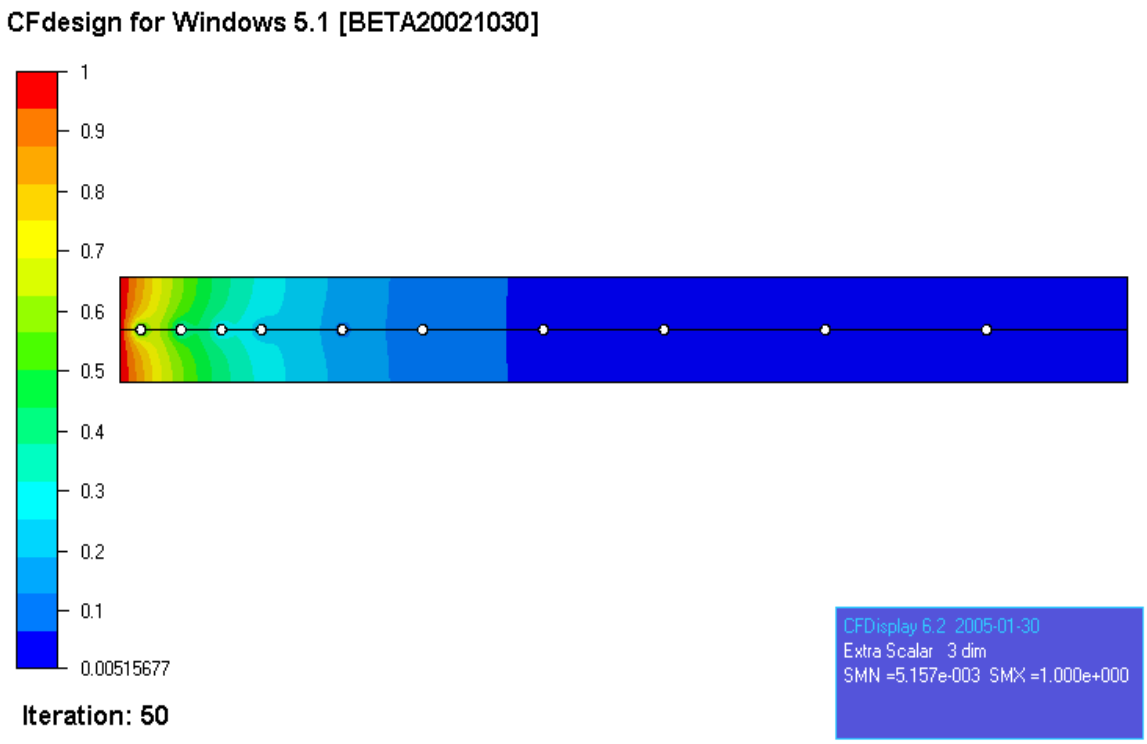

Figure 5.24: Equiconcentration curves shown for the nonporous case at T=353 K, P=3 atm, η=0.8 V at the membrane boundary, 10Pt, air, agglomerate length of 1 μm and agglomerate outer radius of .05, loading of 5.23e-06 μm^3/agglomerate, particle radius of 5 nm.

with a sufficiently high concentration of O_2. Thus, from a concentration standpoint it would seem that the biasing loading of Figure 5.24 is superior to the uniform loading of Figure 5.12.

Now, Figure 5.25 shows that when moving from uniform to biased loading, there is an increase in performance for the porous case. However, for this case, the biasing does not overall have a very big effect on current density since species diffusion primarily in the radial direction and the loading is biased in the axial direction. The effect of biasing is further explored in Figures 5.26 and 5.27.

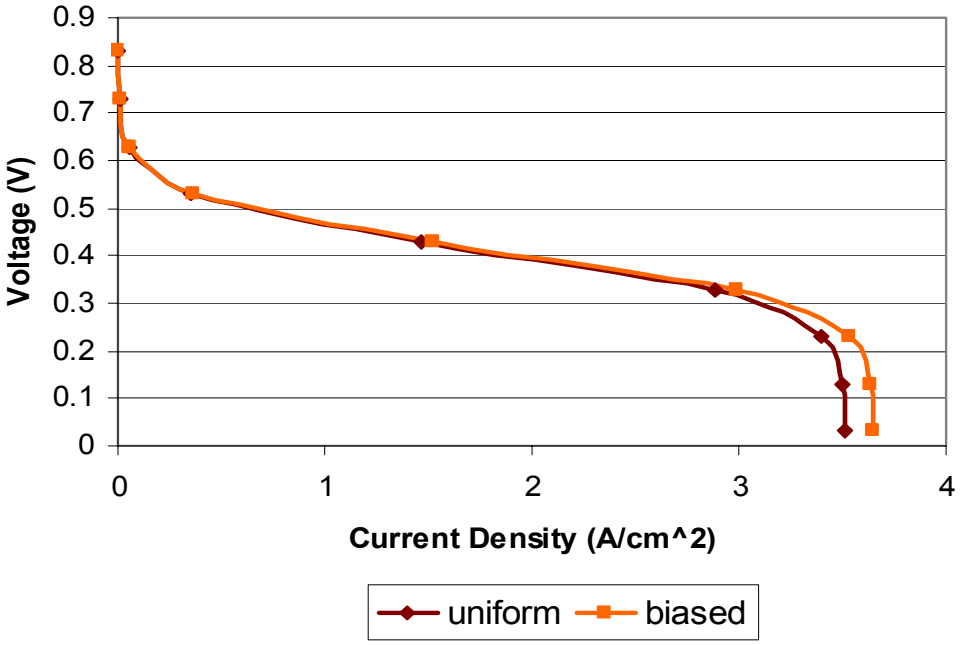

Figure 5.25: Biased porous case versus the porous case at T=353 K, P=3 atm, η=0.8 V, 10Pt, air, agglomerate length of 1 μm and pore outer radius of .05, porosity=50%, loading of 5.23e-06 μm^3/agglomerate, particle radius of 5 nm.

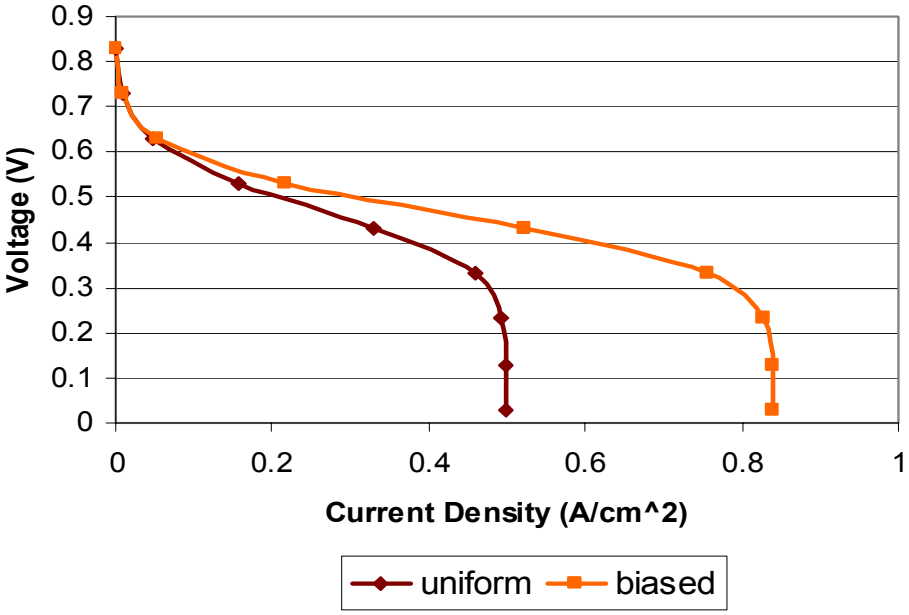

Figure 5.26: Biased flooded porous case versus the flooded porous case at T=353 K, P=3 atm, η=0.8 V, 10Pt, air, agglomerate length of 1 μm and pore outer radius of 0.05, porosity=50%, loading of 5.23e-06 μm^3/agglomerate, particle radius of 5 nm.

Unlike Figure 5.25, Figures 5.26 and 5.27 show a significant effect of biasing for the flooded porous and nonporous cases. This great improvement is not evident in the porous case due to the concentration not changing much down the length of the pore of the active layer. This is not the case for the flooded porous and nonporous cases. Thus, the greater particle loading towards the GDL creates a higher species flux into the agglomerate from the GDL and a higher current density.

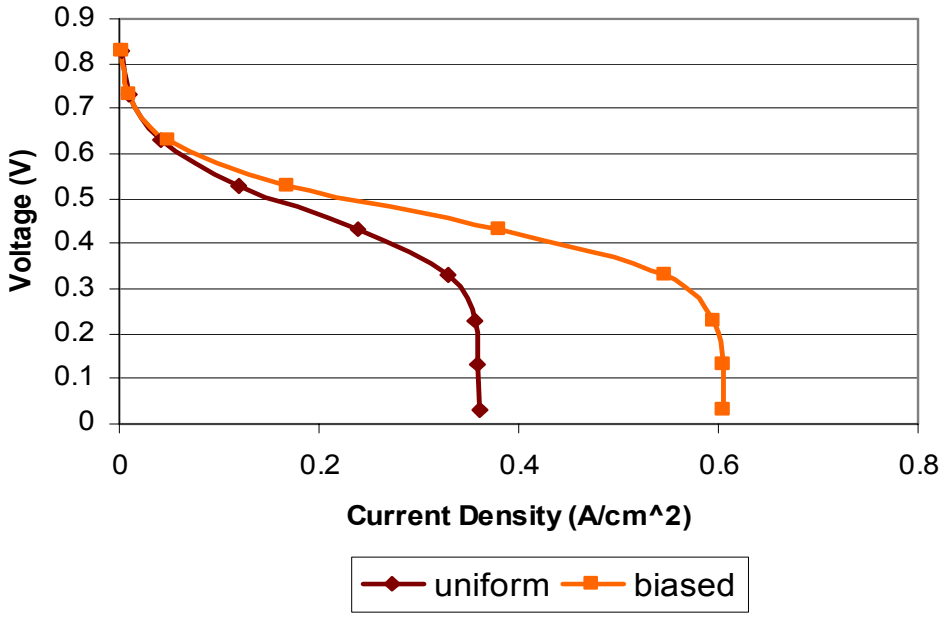

Figure 5.27: Biased nonporous case versus the nonporous case at T=353 K, P=3 atm, η=0.8 V, 10Pt, air, agglomerate length of 1 μm, loading of 5.23e-06 μm^3/agglomerate, particle radius of 5 nm.

Since the biasing does not seem to have any negative effects for any of the cases, the increase in performance which results suggest that it may be worth while investigating experimentally. This could be done by using two different catalyst loadings or more and applying the lighter loading to the membrane and the heavier loading to the GDL side of the active layer. This should help improve fuel cell performance.

Chapter 6: Conclusions and Recommendations

The research presented in this thesis includes the development of steady state microscopic continuum models capable of discretely modeling the electrode active layers of PEMFCs. These models involve a set of differential equations describing the transport of O_2 and ions and the electrochemical kinetics of the oxygen reduction reaction taking place at, for example, the cathode of a PEMFC. By first validating and then further developing the Agglomerate Model used in the research by Bultel, Ozil, and Durand [8], my modified models are able to account for pores, flooding, and various thermodynamic and geometric conditions within the fuel cell. Results from this work include suggested optimal cathode active layer configurations to enhance overall fuel cell performance.

6.1 Conclusions from the Models

Based on the literature, a Thin Film and an Agglomerate Model are developed and geometry implemented with the use of FEMAP™, a finite element meshing program. Using FEMAP™, a uniform geometry and mesh can be constructed, and boundary conditions input. The geometry is then used in CFDesign™, a fluid dynamic finite element solver capable of computing the solution across a particular domain. The result of the solution process is a set of polarization curves which through an extensive parametric study allow conclusions to be drawn from both the modeling and construction of an electrode.

Three agglomerate models are introduced in this research (porous, flooded porous, and nonporous) in order to accurately model the varying geometric conditions present within a fuel cell active layer. A case can be made that an actual fuel cell active layer does not mimic one of these cases in particular but instead an average of the three.

6.1.1 Discrete Computational Model

As far as this research could ascertain, there has been little work in the literature regarding the discrete modeling of platinum catalyst particles. The work of Bultel, Ozil, and Durand [8] and related works by the same authors offer the only real insight into such modeling. The authors concluded that the discrete modeling of platinum particles at the cathode active layer is not needed, implying that the layer can be considered homogeneous (non-discrete), as is commonly done in the CFD modeling of fuel cells. The work done in this thesis found that at low current densities (<0.13 A/cm^2) the homogenous approximation is valid. However, at current densities greater than 0.13 A/cm^2, the nondiscrete case eventually dwarfs the discrete case, suggesting that discrete catalyst modeling at the cathode may be quite important. At the anode active layer, the discrete modeling is important at most current densities

Another assumption generally accepted in the literature is that current density is simply a function of catalyst effective area for the slow oxygen reduction reaction at the cathode. This assumption is valid at low current densities for thin active layers. However, this conclusion seems to be premature at higher current densities. The particular placement of a single platinum particle is shown to have a significant effect on fuel cell performance. A particle close to either a gas pore or the GDL/active layer interface increases the gradient and, thus, the flux of O_2 species into the active layer. This platinum placement aids the limiting current density seen at the cathode and should increase overall fuel cell performance.

6.1.2 Conclusions about Overall Cathode Active Layer Makeup

Results from the parametric study provide recommendations for thermodynamic conditions and calls for experimental research into the geometric configuration of a proton exchange membrane cathode active layer. The following list consists of notable results obtained from the current research:

- High pressures and temperatures are recommended for cathode active layer performance due to increased concentrations seen at the GDL/active layer interface with increased pressure and improved kinetics noticed with increased temperature.
- The more particles added to an active layer, the more uniform the layer behaves. Thus, a subsequent increase in performance is noticed. This suggests there should be many smaller platinum particles rather then fewer larger particles for a fixed catalyst surface area
- A porous active layer is shown to outperform a flooded or nonporous active layer by a factor of approximately 6. Flooding must be avoided as much as possible since when flooding occurs, a porous active layer's performance approaches that of a nonporous active layer.
- The degree to which pure O_2 outperforms air for a given geometric configuration is quantified. However, current density for the porous agglomerate when air is used outperforms the flooded porous and nonporous agglomerate configurations using pure O_2. This result proves that high current densities can be obtained without the use of pure O_2.
- Loading is shown to have a linear effect on current densities using thin porous active layers and low to medium current densities. Above these densities, the effects begins to become somewhat nonlinear. Furthermore, loading is shown to have a relatively small effect on the limiting current densities for the flooded porous and nonporous cases due to problems associated with species transfer.
- Porosity does not have to be high to promote fuel cell performance. The current density within the cathode active layer of a fuel cell benefits from a uniform distribution of pores and agglomerates. This uniformity enables lower porosity to flourish due to the increased ion conducting characteristics for all thicknesses of active layer (1μm, 10μm, and 20μm). However, thin active layers (1μm) also perform well using high porosities due to their increased O_2 transport capabilities. With a thin active layer, ion conduction is not a problem.

- A biased catalyst active layer geometry is recommended due to its positive effect on current density for all active layer cases (porous, flooded porous, and nonporous)

These conclusions answer the chief objectives (1 to 4) mentioned in Chapter 1.

6.2 Future Recommendations

The work done in this study can be extended to include several factors. First, further validation of a set of physical properties characterizing fuel cell kinetics is necessary to be sure that the models accurately reflect fuel cell operation. Although there is fairly consistent species transport data available in the literature, when it comes to the electrochemical kinetics the data is inconsistent between the authors and even between separate experiments by the same authors. Resolving this issue is critical to future modeling of these active layers.

Electron conduction within the agglomerate also needs to be considered. The models developed in this research assume that a continuous conduction pathway leading from the carbon supported catalyst to the GDL exist. This assumption needs to eventually be replaced by some type of geometric modeling of this pathway since pure water which has a conductivity four orders of magnitude lower than that of carbon is not a sufficient pathway. Thus, more research is needed into how a discrete carbon network would be incorporated into the active layer.

To further develop the models presented in this research, other layers of the proton exchange membrane should be considered. The addition of a discrete anode active layer and membrane would result in a more representative fuel cell model. Such a model would account for various other phenomena such as water transport, momentum, and energy present in the fuel cell.

As to the current research, it would appear that with the computer hardware available to us currently, computations have hit a computing limit. For example, the most complex geometry considered has a length of 20μm and 100 platinum particles,

requiring half a million nodes in order to produce consistent results. These results however, require three days of computation. Thus, more complicated models will, perhaps, require a cluster system. Though processing power increases every year, nothing could compare to a cluster working in parallel. Also, the computing architecture from both AMD and Intel are starting to implement 64-bit capabilities. One of the computers used to run CFDesign™ is 64-bit capable, but CFDesign™ is not. Thus, hopefully a 64-bit computational fluid dynamics code is somewhere in the near future.

References:

1 Schatz Energy Research Center, http://www.humboldt.edu/~serc/animation.html.

2 Automotive Technology. http://www.automotive, technology.com/projects/p2000/p20006.html, 2004.

3 Rocky Mountain Institute, http://www.rmi.org/sitepages/pid556.php, 2004.

4 Fuel Cell Test and Evaluation Center, http://www.fctec.com/fctec_types_pem.asp, 2003.

5 Genevey D.B., von Spakovsky M.R., Ellis M.W., Nelson, D.J., Olsommer B., Topin F., and Siegel N., *Transient Model of Heat, Mass, and Charge Transfer as well as Electrochemistry in the Cathode Catalyst Layer of a PEMFC*, International Mechanical Engineering Congress and Exposition – IMECE'2002, ASME IMECE Paper No. 33322, November 2002.

6 Siegel N.P., Ellis M.W., Nelson D.J., and von Spakovsky M.R., *Single Domain PEMFC Model Based on Agglomerate Catalyst Geometry,* Journal of Power Sources, Vol. 115, pp. 81-89, 2002.

7 Siegel N.P., Ellis M.W., Nelson D.J., and von Spakovsky M.R., *A Two-Dimensional Computational Model of a PEMFC with Liquid Water Transport,* Journal of Power Sources, 2003.

8 Butel Y., Ozil P., and Durand R., *Concentration and Potential Distributions in the Active Layer of Proton Exchange Membrane Fuel Cell Electrodes,* Journal of Applied Electrochemistry, Vol. 30, pp. 1369-1376, 2000.

9 Butel Y., Ozil P., Durand R., and Simonsson D., *Study of Mass Transfer within the Active Layer of P.E.M.F.C. Electrodes at the Particle Level,* Electrochemical Society Proceedings, Vol. 95, pp. 34-47, 1995.

10 Butel Y., Ozil P., and Durand R., *Modeling the mode of operation of PEMFC Electrodes at the particle Level: Influence of Ohmic Drop within the Active Layer on Electrode Performance,* Journal of Applied Electrochemistry, Vol. 28, pp. 269-276, 1998.

11 Antoine O., Bultel Y., Durand R., and Ozil P., *Electrocatalysis, Diffusion, and Ohmic Drop in PEMFC: Particle Size and Spatial Discrete Distribution Effects,* Electrochemica Acta, Vol. 43, No. 24, pp. 3681-3691, 1998.

12 Bultel Y., Ozil P., and Durand R., *Modeling of Mass Transfer within the PEM Fuel Cell Active Layer: Limitations at the Particle Level,* Journal of Applied Electrochemistry, Vol. 29, pp. 1025-1033, 1999.

13 Gloaguen F., Convert P., Gamburzev O., Velev O.A., and Srinivasan S., *An Evaluation of the Macro-homogenous and Agglomerate Model for Oxygen Reduction in PEMFCs,* Electrochemica Acta, Vol. 43, No. 24, pp. 3767-3772, 1998.

14 Parthasarathy A., Srinivasan S., and Appleby A., *Temperature Dependence of the Electrode Kinetics of Oxygen Reduction at the Platinum/Nafion Interface – A Microelectrode Investigation,* Journal of Electrochemical Society, Vol. 139, No. 9, pp. 2530-2537, 1992.

15 Beattie P., Basura V., and Holdcroft S., *Temperature and Pressure Dependence of O_2 Reduction at Pt/Nafion® 117 and Pt/BAM® 407 Interfaces,* Journal of Electroanalytical Chemistry, Vol. 468, pp. 180-192, 1999.

16 Zang L., Ma C., and Mukerjee S., *Oxygen Reduction and Transport Characteristics at a Platinum and Alternative Proton Conducting Membrane Interface,* Journal of Electroanalytical Chemistry, Vol. 568, pp. 273-291, 2004.

17 Um S., Wang C., and Chen K., *Computational Fluid Dynamics Modeling of Proton Exchange Membrane Fuel Cells,* Journal of Electrochemical Society, Vol. 147, No. 12, pp. 4485-4493, 2000.

18 Bird R., Stewart W., and Lightfoot E., *Transport Phenomena,* U.S.A., 1960.

19 Ma C., Mukerjee S., Ofer D., and Nair B., *An Investigation of Proton Conduction in Select PEM's and Reaction Layer Interfaces-Designed for Elevated Temperature Operation,* Journal of Membrane Science, Vol. 219, pp. 123-136, 2003.

20 Welty, Wicks, and Wilson, *Fundamentals of Momentum, Heat and Mass Transfer,* New York, 1976.

21 International Union of Pure and Applied Chemistry, *Solubility Data Series,* Great Britain, 1981.

22 CFDesign® V5.1, Blue Ridge Numerics, 2003.

23 FEMAP® V8.0, EDS, 2002.

24 Larminie, and Dicks, *Fuel Cell Systems Explained,* England, 2000.

25 Patankar, S., *Numerical Heat Transfer and Fluid Flow,* Hemisphere, Washington D.C., 1980.

26 Carbon, http://www.scescape.net/~woods/elements/carbon.html

27 Application Bulletin, http://www.myronl.com/PDF/application_bulletins/DI_AB.pdf